Measurements of Friction and Wear in Chemical Mechanical Polishing Using Single Particle Analog Probes

A Dissertation Presented

by

Joo Hoon Choi

to

The Graduate School

in Partial Fulfillment of the

Requirements

for the Degree of

Doctor of Philosophy

in

Mechanical Engineering

Stony Brook University

May 2009

Stony Brook University

The Graduate School

Joo Hoon Choi

We, the dissertation committee for the above candidate for the
Doctor of Philosophy degree, hereby recommend
acceptance of this dissertation.

Dr. Chad S. Korach – Dissertation Advisor,
Assistant Professor, Mechanical Engineering

Dr. Robert V. Kukta – Chairperson of Defense
Associate Professor, Mechanical Engineering

Dr. Imin Kao – Member
Professor, Mechanical Engineering

Dr. Joseph Levert – Outside Member
Associate Professor at SUNY Maritime College, Mechanical Engineering

This dissertation is accepted by the Graduate School

Lawrence Martin
Dean of the Graduate School

Abstract of the Dissertation

Measurements of Friction and Wear in Chemical Mechanical Polishing Using Single Particle Analog Probes

by

Joo Hoon Choi

Doctor of Philosophy

in

Mechanical Engineering

Stony Brook University

2009

In this work, lateral force microscopy (LFM) was performed with analogs (silica-coated AFM probe and diamond-coated AFM probe) of a nanoscale individual CMP abrasive particle to mimic a chemical mechanical polishing (CMP) process. The silica-coated AFM probes were used to investigate the 2-body friction contribution of an individual silica CMP polishing particle in contact with the polishing pad (JK111) and silica substrates (bulk silica and thermal grown oxide wafer) for load and pH ranging from 10 nN to 50 nN and 7 to 11, respectively. Actual surface deformations of the three samples were obtained to determine the predominant friction involved during LFM. It was shown that the predominant friction mode for the pad surface was plowing friction while the friction of the silica substrates was governed by adhesive friction. This lead to the understanding why the friction results for the pad was higher than other samples. A proper friction model for the bulk silica was determined by fitting the friction results with Carpick's generalized transition equation. It was shown that the friction results at pH 7 and 9 were determined to follow the JKR model while the friction responses at pH 10 and 11 should not be analyzed with adhesive-based friction models because no adhesion force was observed. The diamond-coated AFM probes were used to simulate the surface damage occurring during a CMP process. AFM force lithography was performed on structures composed of various copper-dielectric pattern densities and two dielectric materials under a

KOH environment. The damaged surfaces due to lateral force were analyzed to obtain the scratch depth of copper interconnects and line bending of patterned structures. It was observed that the structure with higher pattern densities were susceptible to deformation because they were composed more copper interconnect than the dielectric film. The critical load to initiate the plastic deformation of copper interconnects for the surface deformation was measured. In addition, the structure composed a weaker dielectric film was more susceptible to plastic deformation. For bending of pattern structures, the structure with a similar pattern density but larger dielectric film width or with stiffer dielectric material showed more resistance to bending.

Table of Contents

List of Tables

List of Figures

Chapter One
Introduction

1.1 Chemical Mechanical Polishing (CMP)

1.1.1 Overview of CMP

Since the revolutionary invention of a transistor by Bell Labs in 1947 and an Integrated Circuit (IC) in 1958, electronic devices have developed extensively. As technology advanced, there has been a need in the semiconductor industry to increase the device density while improving its performance. The goal was achieved by producing multi-level structures through metallization process, which reduces lateral circuit dimensions to minimize RC interconnect delay [1.1]. As each level is constructed with vertically-connected metal interconnects and silica dielectric insulator, formation of nonplanarized surface topography of each level during fabrication process is inevitable [1.2]. Conventional planarization techniques removed the excessive surface material by indentation and abrasion leaving defects such as scratch marks, fine cracks and pits on the surface [1.3].

An improved planarization technology was in demand to achieve global and local planarization with minimized defects and high removal rate [1.1, 1.4 – 1.6]. The technique was also needed during fabrication of Micro-Electro-Mechanical-Systems (MEMS) and Nano-Electro-Mechanical-Systems (NEMS).

A polishing technique known as Chemical Mechanic Polishing (CMP) was first invented by IBM in 1984 and it has been developed intensively since. It has shown a dynamic growth playing a key role in the semiconductor industry due to the planarization ability and effectiveness in removing defects on a wafer surface [1.1]. It can produce a smooth and planarized surface with minimal surface or sub-surface damage by combining synergetic effects of chemical and mechanical actions to polish the surface of a substrate [1.7 – 1.8]. After the chemical interaction among polishing abrasives, a substrate material and a chemical environment weakens the substrate surface, then the mechanical abrasion removes the weakened surface [1.3]. CMP polishes a substrate material such as a wafer composed of silicon, oxide or metal (W, Cu or Al) by rubbing the surface of the substrate with nanometer-scale polishing particles suspended in the form of an aqueous slurry between the surfaces of the substrate and a polishing pad. The schematic of CMP is presented in Figure 1.1. There are three main components: a substrate to be polished, slurry composed of corrosive chemicals and abrasive particles, and a porous polyurethane polishing pad to keep the particles in place and remove polish materials. A substrate is mounted on the head and pressed against a polishing pad which is mounted on a platen. While the head and platen spin in the same direction, but about different axes, CMP slurry is fed onto the surface of the pad. The porous pad is typically made of polyurethane with modulus of 500 MPa and the pore size is approximately 50 um in diameter. A slurry is composed of a chemical solution and polishing particles. The chemical solution is generally an acidic slurry (nitric or citric acid) or alkaline slurry such as ammonium hydroxide (NH_4OH) or potassium hydroxide (KOH) with pH 10 or greater. The slurry chemicals soften the substrate to improve the material removal rate and prevent particles from agglomerating. The most commonly used abrasive particle in CMP is silica or alumina with size ranges from 50 to 200 nm in diameter. The interaction among these three main components polishes the wafer involving friction.

1.2 Issues in CMP

1.2.1 Optimization efforts in CMP

Researchers have tried to optimize the CMP process 1) through development of diverse material removal rate (MRR) models, which can fit experimental results, 2) through controlled polishing, which involves investigations of operational parameters effects on polishing performance and 3) through the fundamental study of polishing mechanisms.

1.2.1.1 MRR Modeling

First, prediction of material removal rate of the wafer is possible by investigating process parameters (down force and rotational velocity) and input parameters (hardness and elastic modulus of the wafer and the pad, roughness of pad and size and geometry of polishing abrasives). Many researchers have strived to develop MRR models which are based on FEM, contact mechanics, mathematics, plasticity and abrasion mechanism [1.3, 1.9 – 1.12]. For example, Fu et al. developed a plasticity-based MRR model assuming that the pad-particle-wafer interface possessed perfectly plastic behavior and considering the deformation of the soft pad as bending of a thin elastic beam. Their model predicted the material removal rate as a function of process parameters such as down force and relative velocity during polishing and design parameters such as pad and slurry properties [1.3].

1.2.1.2 Process parameters effects

Instead of investigating all CMP parameters that affect MMR at the same time, many researchers focused on an individual polishing parameter and investigated their effects on polishing [1.13 – 1.21]. CMP performance on silica dielectric depends on the material properties of pad, particle and wafer at the surface and near-surface regions and the interactions among them. In addition, processing parameters affect the results as well. Choi et al. [1.22] investigated effects of pH and down forces on polishing rates, friction forces and surface topography during polishing of silicon dioxide dielectric considering solubility of silica and interaction forces between the silica abrasives and silica wafer for various pH environments.

1.2.1.3 Fundamental study of CMP with AFM

Lastly, there have been efforts to investigate the fundamental responses such as friction, adhesion or surface force during polishing process by utilizing an atomic force microscope (AFM) to have a better understating of CMP process. Ducker et al. [1.23] measured surface forces between a colloidal particle and oxidized flat silicon wafer by attaching a colloidal sphere at the end of a blank AFM cantilever. Lin et al. [1.24] utilized AFM to measure surface forces between a silicon nitride (Si_3N_4) AFM tip and an oxidized silicon wafer in KNO_3 electrolyte under various pH environments ranging of pH from 3 to 11. Sokolov et al. [1.25] investigated the surface interaction forces between silica or silicon nitride AFM probes and surfaces of polyurethane CMP polishing pads in KNO_3 solution with pH values ranging from 4 to 10 to measure surfaces potentials of silica, silicon nitride and polyurethane pad, which were derived by applying DLVO theory to the measured force-distance results. Taran et al. [1.26] employed lateral force microscopy of AFM to simulate friction during CMP polishing. A silica particle was attached to a blank AFM cantilever as an analog of the CMP polishing particle. The friction between the silica particle and a silica wafer were measured for pH values between 3.6 and 10.6 and different normal loads. The friction responses were examined to observe dependence of friction on pH environment and load conditions during CMP.

1.3 Outline of this work

One way to achieve increased MRR with reduced damages/defects during CMP is to control the polishing process by varying CMP parameters. As shown in the work by Choi [1.22], the overall effect of process parameters on the material removal rate can be found by varying the parameters. However, that does not lead to a fundamental understanding of interaction occurring during CMP. Investigation of the interaction between a single abrasive particle and a substrate wafer or a polishing pad can assess the effects of CMP parameters at the interface and can correlate a single abrasive particle response with overall process measurements. This will also help to minimize a number of controllable CMP parameters because it can describe how any variation of a single CMP parameter affects interactions near the interface and how one interaction can be affected by various CMP parameters.

In this work, an analog of the single abrasive particle, which is similar in size or same in material, is created to study its interaction with CMP process materials utilizing AFM to examine effects of slurry chemistry, particle size and correlate a single abrasive particle friction with process friction measurements. There are two parts in this work. The first part is to assess the frictional response of an individual particle analog on CMP process materials to obtain fundamental relationships of the frictional contributions, which will lead to an improved understanding of the effects of particle properties and CMP process parameters on polishing. The second part is to investigate surface feature damage due to friction and provide insight that can be used for optimizing the oxide polishing process.

1.3.1 Part 1 – Application of Abrasive Particle Analogs to Oxide CMP

CMP removes the surface of a wafer by the synergetic interactions of chemical and mechanical contributions to polish the surface. Researchers have studied the contribution of each aspect. The chemical contribution in CMP is the chemical reaction at the pad-particle-wafer interface, which alters the physical and mechanical properties of the interface [1.27 – 1.29]. The mechanical contribution of material removal is due to mechanical abrasion, which removes material and planarizes the surface through the direct contact of between the wafer surface and abrasive particles embedded in the pad [1.30 – 1.31]. The abrasion mechanism develops due to friction from different contact modes, which contribute to overall or global friction in CMP. When the polishing pad is pressed against the wafer, friction between the asperities of the pad and the wafer is introduced because the pad is in direct contact with the wafer surface. This contribution is not significant because the polishing pad is made of polyurethane, which has a lower elastic modulus than CMP polishing particles and wafers being polished. Alternatively, there can be 2-body or 3-body contact at the pad-particle-wafer interface depending on conditions. Since the pad is porous and rough in nature, some parts of the particles will be trapped between the asperities of the pad and wafer during polishing. The contact among the pad, particle and wafer is a 3-body contact. When the load at the interface is low, the 3-body contact induces rolling of the abrasive particles during polishing. When there exists a slight load, the particle trapped between the pad and wafer can damage the pad surface. This is a 2-body contact between the pad and the particle. In some cases, the load applied at the interface is large enough for the pad to deform into the surface of the pad and end up being embedded in the pad. This direct contact between the particle and wafer is a 2-body contact for the silica particle and the substrate. The contributions from the pad-substrate and 3-body contacts are minor while those from the 2-body contacts (particle-pad and particle-silica contacts) play an important role in removing the substrate material. Investigation of the friction contribution from a single polishing particle can be used for material removal models for CMP and lead to fundamental understanding of the contribution of the 2-body contact to global friction such as relationship between chemistry and contract area, types of friction and particle size optimization.

In this work, AFM is used to study frictional response during CMP polishing. Lateral force microscopy (LFM) is performed with SiO_2 coated AFM probes to investigate the 2-body friction contribution of an individual silica CMP polishing particle in contact with a compliant non-porous polyurethane polishing pad (JK111), a stiff bulk silica substrate and a thermally grown oxide wafer under various applied normal loads and diverse pH environmental factors. Based on the friction responses by the particle analog, a friction model is developed to integrate the effect of pH into existing nano-scale friction models. Additionally, surface and adhesion forces were determined with the environments to observe their contributions to the friction results. The work is presented in Chapter 3.

1.3.2 Part II – CMP Generated Defects in Cu/low-k Patterned Wafers

Another issue in CMP is to avoid damage of a substrate surface during polishing. Undesired surface damages can be caused by excessive pressure and friction forces applied by polishing particles on a substrate. For example, agglomeration of polishing particles causes gouging of the surface or deformation of patterns on the surface. Investigation of such pressure and lateral force can set a limit for polishing pressure and can be used as reference values for polishing optimization. One of the efforts to minimize the interconnection delay was achieved by the integration from aluminum to copper for metal interconnect and from SiO_2 to low-k (LK) or ultra low-k (ULK) dielectric materials for insulators. However, the adoption of porous low-k materials brought a problem such as delamination of dielectric material during CMP due to poor adhesion between layers, high stress in low-k dielectric layer and poor mechanical strength of porous low-k interlayer dielectrics [1.32]. Even though an extensive amount of work was devoted to develop efficient low-k dielectric materials, problems such as relatively poor mechanical strength, low thermal conductivity and incompatibility problems with existing IC manufacturing processes have not been resolved [1.33].

Many researchers have tried to investigate the delamination of low-k dielectric materials [1.34 – 41]. Busch and etc. [1.42] observed structural and chemical modifications of low-k material by exposing sets of low-*k* blanket wafers to pre- and post-polishing CMP slurry chemistry and performing CMP on another set to see effects of each CMP step and they observed structural and chemical variations were significantly affected only by the polishing case. Balakumar and colleagues [1.43] performed CMP on Cu/SiLK^{TM} single- and dual-stack non-patterned wafers to study fundamentals of delamination during CMP. Leduc and colleagues [1.44] studied the dependence of CMP-induced delamination on number of low-k dielectric films stacked and established the relationship between delamination and the number of ULK dielectric layers during CMP.

The insight into the surface damage can be obtained by investigating the 2-body contacts between the particle-pad and particle-wafer. The contributions of pad-substrate contact and particle-substrate 3-body contact on the damage of a substrate surface during polishing is insignificant but the damage is mainly created from the friction generated by 2-body contact between the substrate and polishing particles where the particles are embedded in the substrate. The amount of embedment depends on the locations of the particle on the surface of the pad whose surface is rough in nature. A shallow embedment will lead to rolling of the particles during polishing while a deep embedment will result in scribing of the substrate surface. When the normal load applied during CMP is high, plowing can occur and can damage the substrate surface by scratch defect damage and surface cracking which lead to reliability and performance degradation of the IC. An understanding of the contribution from a single particle on the damage of the substrate surface can lead to optimization of CMP for advanced materials. The effects of a single CMP particle on a patterned wafer with a low-k dielectric and copper interconnects presents a formidable challenge.

In this work, the concept of a CMP particle analog was adopted by selecting a triangular AFM cantilever with diamond-coated probe. Force lithography of AFM was utilized under high KOH environment to damage the surface of a patterned wafer and the deformation of the surface is investigated to determine the relationship between variations in pattern densities with the loads necessary to initiate deformation, which can be used as a reference for designing specific structures or determining preferred structures. This work is presented in Chapter 4.

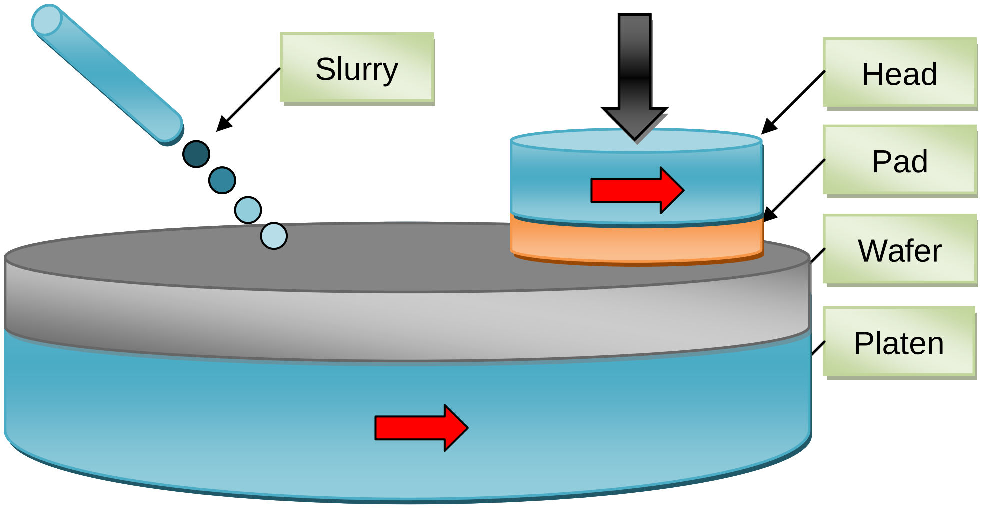

Figure 1.1: Schematic of CMP with main components: wafer, pad and slurry.

1.4 References

1.1 Perry, Chemical Mechanical Polishing: The Impact of New Technology on an Industry, 1998 Symposium on VLSI Technology Digest of Technical Papers

1.2 http://www.sia-online.org/pre_resources_FAQ.cfm

1.3 Guanghui Fu, Abhijit Chandra, Sumit Guha, and Ghatu SubhashF, IEEE TRANSACTIONS ON SEMICONDUCTOR MANUFACTURING, A Plasticity-Based Model of Material Removal in Chemical–Mechanical Polishing (CMP) 14 (2001) 406 – 417

1.4 J. M. Steigerwald, S. P. Murarka, and R. J. Gutmann, *Chemical Mechanical planarization of Microelectronic Materials*, John Wiley & Sons, New York (1997)

1.5 R. K. Singh, S.-M. Lee, K.-S. Choi, G. B. Basim, W. Choi, Z. Chen, and B. M. Moudgil, *MRS Bull.,* **27**, 752 (2002)

1.6 J. M. Steigerwald, S. P. Murarka, and R. J. Gutmann, *Chemical Mechanical Planarization of Microelectronic Materials*. New York: Wiley, 1997

1.7 R. K. Singh and R. Bajaj, in *Advances in Chemical-Mechanical-Planarization 2002*, R. K. Singh and R. Bajaj, Editors; PV 27-10, p. 743, Materials Research Society Bulletin, Warrendale, PA (2002)

1.8 S. M. Lee, W. Choi, V. Craciun, S. H. Jung, and R. K. Singh, Paper I4.11, presented at Materials Research Society Meeting, San Francisco, April 2002

1.9 Yuan, C A, Driel, W D van, Silfhout, R B R van, Sluis, O van der, Engelen, R A B, Ernst, L J, Keulen, F van, & Zhang, G Q, Delamination Analysis of Cu/low-k Technology Subjected to Chemical-Mechanical Polishing Process Conditions, Microelectronics Reliability 46 (2006) 1679-1684

1.10 Vlassak, *A model for chemical–mechanical polishing of a material surface based on contact mechanics*, Journal of the Mechanics and Physics of Solids 52 (2004) 847 – 873

1.11 J. Bai, Y.W. Zhao, Y.G. Wang, *A mathematical model for material removal and chemical–mechanical synergy in chemical–mechanical polishing at molecular scale*, Applied Surface Science 253 (2007) 8489–8494

1.12 Luo and Dornfeld, *Material Removal Mechanism in Chemical Mechanical Polishing: Theory and Modeling*, IEEE TRANSACTIONS ON SEMICONDUCTOR MANUFACTURING, VOL. 14, NO. 2, (MAY 2001) 112-133

1.13 Q. Luo, D.R. Campbell, S.V. Babu, Langmuir 12 (1996) 3563.

1.14 M. Hariharaputhiran, J. Zhang, S. Ramarajan, J.J. Keleher, Y. Li, S.V. Babu, J. Electrochem. Soc. 147 (2000) 3820.

1.15 A. Jindal, S. Hegde, S.V. Babu, Electrochem. Solid State Lett. G 48 (2002) 5.

1.16 D. Zeidler, Z. Stavreva, M. Plotner, K. Drescher, Microelectron. Eng. 33 (1997) 259.

1.17 R. Carpio, J. Farkas, R. Jairath, Thin Solid Films 266 (1995) 238.

1.18 Q. Luo, R.A. Mackay, S.V. Babu, Chem. Mater. 9 (1997) 2101.

1.19 Y. Li, M. Hariharaputhiran, S.V. Babu, J. Mater. Res. 16 (2001) 1066.

1.20 A. Jindal, Y. Li, S.N. Barayanan, S.V. Babu, Mat. Res. Soc. Symp. Proc. 671 (2001) M4.10.1.

1.21 Y. Li, S.V. Babu, Electrochem. Solid State Lett. 148 (2001) G20.

1.22 Wonseop Choi, Seung-Mahn Lee, and Rajiv K. Singh, pH and Down Load Effects on Silicon Dioxide Dielectric CMP, Electrochemical and Solid-State Letters, 7 (2004) G141-G144

1.23 William A. Ducker, Tim J. Senden, and Richard M. Pashley, *Direct measurement of colloidal forces using an atomic force microscope*, Nature

353 (1991) 239

1.24 Xue Yun Lin, Francois Creuzet, Herve Arribart, *Atomic Force Microscopy for Local Characterization of Surface Acid-Base Properties*, J. Phys. Chem. 1993, 97, 7272-7276

1.25 Igor Sokolov, Quy K. Ong, Hasan Shodiev, Nina Chechik, David James, Mike Oliver, *AFM study of forces between silica, silicon nitride and polyurethane pads*, Journal of Colloid and Interface Science 300 (2006) 475–481

1.26 Elena Taran, Bogdan C. Donose, Ivan U. Vakarelski, Ko Higashitani, *pH dependence of friction forces between silica surfaces in solutions*, Journal of Colloid and Interface Science 297 (2006) 199–203

1.27 T. A. Michalske and S. W. Freiman, *J. Am. Ceram. Soc.,* **66**, 284 (1982)

1.28 T. A. Trogolo and K. Rajan, *J. Mater. Sci.,* **29**, 4554 (1994)

1.29 F. B. Kaufman, D. B. Thompson, R. E. Broadie, M. A. Jaso, W. L. Guthrie, D. J. Pearson, and M. B. Small, *J. Electrochem. Soc.,* **138**, 3460 (1991)

1.30 N. J. Brown, P. C. Baker, and R. T. Maney, *Proc. SPIE, Int. Soc. Opt. Eng.*, **306**, 42 (1981)

1.31 L. M. Cook, *J. Non-Cryst. Solids,* **120**, 152 (1990)

1.32 1.4 T. Hara Proceedings of VMIC Asia, 2002 (November) IMIC Publishers (http://www.imic.org) p. 161

1.33 S. Wang, G. Grover, C. Baker, J. Chamberlain, C. Yu, Solid State Technol. 2001 (September) S9

1.34 S. Kondo, S. Tokitoh, B.U. Yoon, A. Namiki, A. Sone, N. Ohashi,K. Misawa, S. Sone, H.J. Shin, T. Yoshie, K. Yoneda, M. Shimada, S. Ogawa, I. Matsumoto, N. Kobayashi, in: International Interconnect Technology Conference 2003 (IITC 2003), IEEE, Piscataway NJ, USA, 2003, pp. 86–88

1.35 T. Scherban, B. Sun, J. Blaine, C. Block, B. Jin, E. Andideh, in: International Interconnect Technology Conference 2001 (IITC 2001), IEEE, Piscataway NJ, USA, 2001, pp. 257–259

1.36 P. Leduc, M. Savoye, S. Maitrejean, D. Scevola, V. Jousseaume, G. Passemard, in: International Interconnect Technology Conference 2005 (IITC 2005), IEEE, Piscataway NJ, USA, 2005, pp. 209–211

1.37 S. Wang, G. Grover, C. Baker, J. Chamberlain, C. Yu, Solid State Technol. 2001 (September) S9

1.38 X.T. Chen, Y.T. Tan, Y.W. Chen, C.Y. Li, S. Balakumar, K. Chew, P.D. Foo, Proc. 19th VMIC conference, 2002, Singapore, 2002, IMIC Publishers (http://www.imic.org) p. 156

1.39 T. Hara, M. Uchica, M. Fuimoto, T.K. Doy, S. Balakumar, N. Babu, Electrochem. Solid State Lett. 7 (2004) G28

1.40 A.K. Sikder, P. Zantye, S. Thagrella, A. Kumar, B.M. Vinogradov, N.V. Gitis, CMP MIC Proceedings, 2003, IMIC Publishers (http://www.imic.org) p. 120

1.41 N. Endo, S. Kondo, S. Tokitou, B.U. Yoon, N. Ohashi, S. Sone, H.J. Shin, I. Matsumoto, N. Kobayashi, CMP-MIC Conference Proceedings, 2003, IMIC Publishers (http://www.imic.org) p. 101

1.42 Busch, Analyzing damage from ultralow-k CMP, *Solid State Technology* November, 2005

1.43 Balakumar and etc., Peeling and delamination in Cu/SiLK^{TM} process during Cu-CMP, Thin Solid Films 462-463 (2004) 161-167

1.44 Leduc and etc., Dependence of CMP-induced delamination on number of low-k dielectric films stacked, Microelectronic Engineering 83 (2006) 2072-2076

Chapter Two
Abrasive Particle Analog

2.1 Analogs of CMP abrasive particles

The AFM has been utilized to study the fundamentals involved in CMP at the single particle scale. Taran and et al. [1.26] attached a silica colloidal probe to a bare AFM cantilever as shown in Figure 2.1 and performed lateral force measurements on a silica substrate in various pH environments to measure friction. In their work, the applied normal load was on the order of a μN, which is typical for CMP. However, the colloidal probe radius was on the order of μm, which led to a contact pressure that was lower than the pressure applied by a single particle in CMP. Sokolov and coworkers [1.25] used thermal oxidization to grow a silica layer on an AFM probe to simulate a silica abrasive particle. The silica probe, as an analog of a silica particle in CMP, was used to measure the surface interaction forces between the AFM probe and the surface of an IC1000 polishing pad in KNO_3 solution with pH values ranging from 4 to 10. Chen and

Singh [2.1] studied a dilute HF cleaning procedure by measuring surface forces between a silicon wafer and a silicon nitride AFM probe to investigate the particle deposition mechanism of contamination particles on the surface of the silicon wafer. Devecchio et al. [2.2] used an AFM tip to study the removal rate of aluminum during CMP by applying high lateral force between the AFM tip and the aluminum sample for various normal loads and pH environments. Stevens et al. [2.3] discussed the wear of sodium trisilicate glass with a silicon nitride AFM tip by investigating the substrate removal rate.

One of the goals in this work is to investigate the friction contribution of an individual silica CMP polishing particle in contact with the CMP process materials. This is achieved by producing an AFM particle analog with dimensions similar to a nano-scale CMP abrasive particle using thermal oxidization. Lateral force microscopy (LFM) is performed on an oxide and polishing pad with similar contact pressure applied to a single abrasive particle in actual CMP with varying environments. Another goal is to apply the particle analog to replicate damage generated during CMP. When applied to patterned wafers, relationships between line pattern densities and the loads necessary to initiate deformation can be developed.

Figure 2.2 is a schematic that illustrates contacts of an abrasive particle with the surfaces of a substrate and a polishing pad during CMP process. The yellow circles represent abrasive particles in different sizes. As the substrate travels with a relative velocity (V), Some of the abrasive particles are in contact with the substrate (particle-wafer contact) and with the pad (particle-pad contact) while others are suspended in the slurry. The frictions of the two contact locations (shown in dotted circles) are mimicked in this work utilizing the particle analog. Figure 2.3 shows the replicated interactions of the silica particle analog with a substrate or pad. The yellow circle represents the silica particle with radius R and the oxidized AFM probe tip with similar radius. The rectangle in contact with the particle represents a sample (either wafer or pad). The oxidized AFM probe is an excellent analog of a nano-scale polishing particle in CMP because silica is one of the most used CMP polishing particles and the tip radius of the oxidized probe is at the similar order of magnitude as a typical silica CMP polishing particle.

2.2 Silica AFM probe

2.2.1 Fabrication of a silica AFM probe

To replicate the nano-scale Individual CMP particle, polysilicon AFM probes [Bare NSG01 (NT-MDT) and NSC19/NoAl (μmasch)] with a tip radius of 10 and 40 nm were oxidized by following the methodology developed by Huttl [2.4]. The polysilicon probe was placed in a high temperature muffle furnace (Barnstead International, Model #: F46248CM) for 2 hours at 1000 °C under standard atmosphere and pressure. An elapsed time of 5 minutes was necessary for the furnace temperature to be raised to 1000 °C. After 2 hours of oxidization, the furnace was allowed to cool down to room temperature before the sample was removed. During the oxidization process, oxygen reacts with the outer layer of the polysilicon. Following is the dry oxidation process:

$$\mathrm{Si} + \mathrm{O_2} \xrightarrow{1000^0 C} \mathrm{SiO_2}$$

The chemical reaction produces a silica layer on top of the existing polysilicon and the generation of the silica layer results in increase of the tip radius.

2.2.2 Tip characterization of a silica AFM probe

After probe tip oxidation, the probes were characterized with a Scanning

Electron Microscope (SEM) (Zeiss/Leo 1550). The thicknesses of the oxide layers were estimated by analyzing the SEM micrographs obtained with the in-lens detector. With an applied voltage of 20 kV and working distance of 4 mm, it was possible for the detector to see through the probe tips. The difference of contrast between the two layers was distinct enough to estimate the thickness of the oxide layer (see Figure 2.4). The oxide thickness of the probes ranged from 50 to 100 nm. The existence of the silica layer was verified by utilizing SEM EDAX analysis as shown in Figures 2.5 (a) and (b). The probe tip which was oxidized clearly shows a strong Oxygen peak, where the silicon probe does not. SEM micrographs obtained with the secondary electron detector were used to determine the tip radii of curvature of the oxidized AFM probes. The same applied voltage and working distance were selected for the secondary detector. Since the micrographs obtained with the in-lens detector had translucent regions to the SEM detectors, there was a chance for the images to lose detail of the tip edges. Since the secondary detector was more sensitive for thinner objects, the micrographs obtained with the secondary detector were used to characterize the tip radius of curvature. Figures 2.6 (a) and (b) show SEM micrographs of the tip of an AFM probe before and after oxidization, respectively. The radii of curvature of tip before and after oxidization were 40.74 nm and 51.85 nm, respectively. The tip radius is shown to increase with oxidation exposure.

2.3 Diamond-coated AFM probe

The second part of this work requires an AFM probe that can apply normal and lateral loads large enough to damage a patterned wafer and resist wear during LFM. To satisfy these two conditions, triangular AFM cantilever with a diamond-coated AFM probes were utilized [DCP20, NT-MDT]. The tip radius and thickness of the diamond coating of each probe were measured with SEM as in the case of the oxidized tips.

2.3.1 Tip characterization of diamond coated AFM probes

The diamond coating was observed with SEM to measure the thickness of the coating and the radius of curvature of the coated probes. The degree of wear of the diamond coating due to LFM experiments was also assessed by SEM. The back scattering detector with 20 kV and 8 mm working distance was utilized to see through the probe. The measured thickness and the radius of curvature were approximately 99.89 nm and 82.03 nm, respectively (see Figure 2.7 (a)). After performing LFM tests, the used tip was observed with SEM to measure the wear of the tip (see Figure 2.7 (b)).

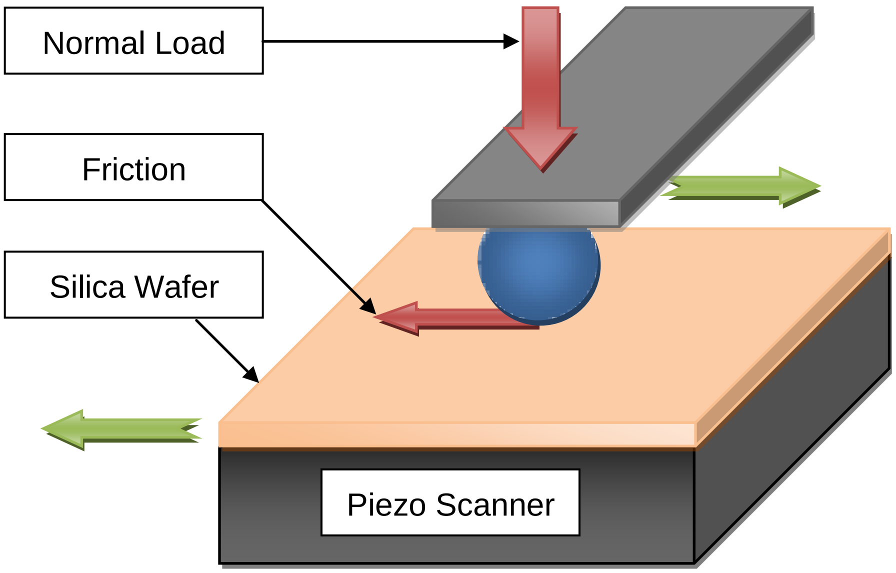

Figure 2.1: Schematic of a silica colloidal probe attached to an AFM cantilever, used for lateral force measurements on silica.

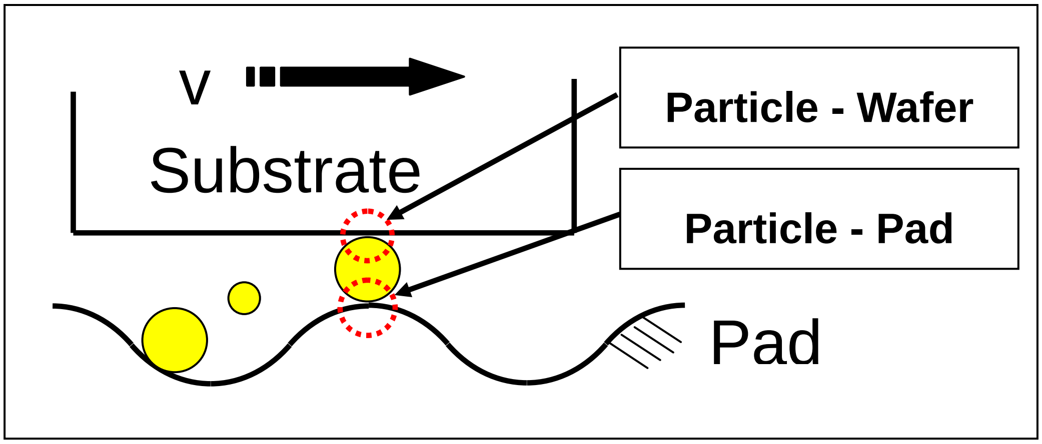

Figure 2.2: Schematic of contacts of an abrasive particle with the surfaces of a substrate and a polishing pad during CMP process. The yellow circles represent abrasive particles in different sizes. Some of the abrasive particles are in contact with the substrate (particle-wafer contact) and with the pad (particle-pad contact) while others are suspended in the slurry. The frictions of the two contact locations (shown in dotted circles) are mimicked in this work utilizing the particle analog.

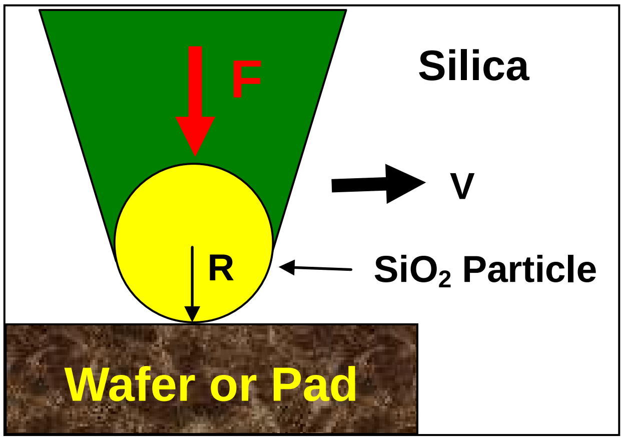

Figure 2.3: Analog of a CMP abrasive particle by an AFM probe tip in contact with a counterface material. The yellow circle represents the silica particle with radius R and the oxidized AFM probe tip with similar radius. Thus, the tip is the analog of the silica particle in CMP. The rectangle in contact with the particle represents a sample (either wafer or pad).

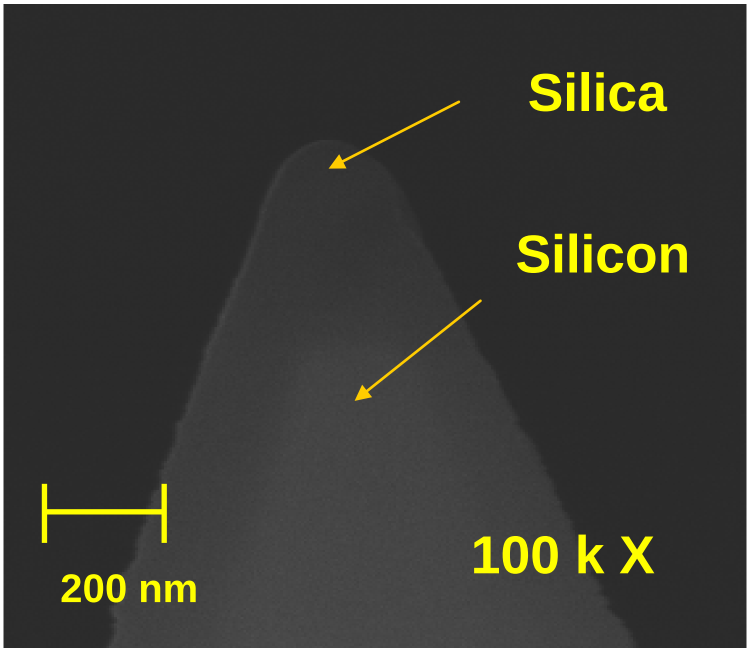

Figure 2.4: SEM micrograph obtained by the in-lens detector, which can see through the oxidized probe. The contrast difference between the silicon and silica was used to estimate the thickness of the oxide layer, which ranged from 50 to 100 nm.

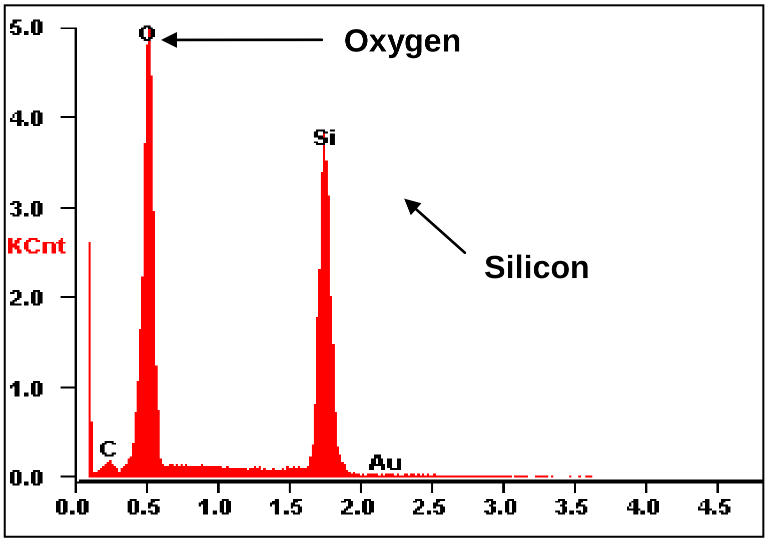

(a) Silica AFM Probe

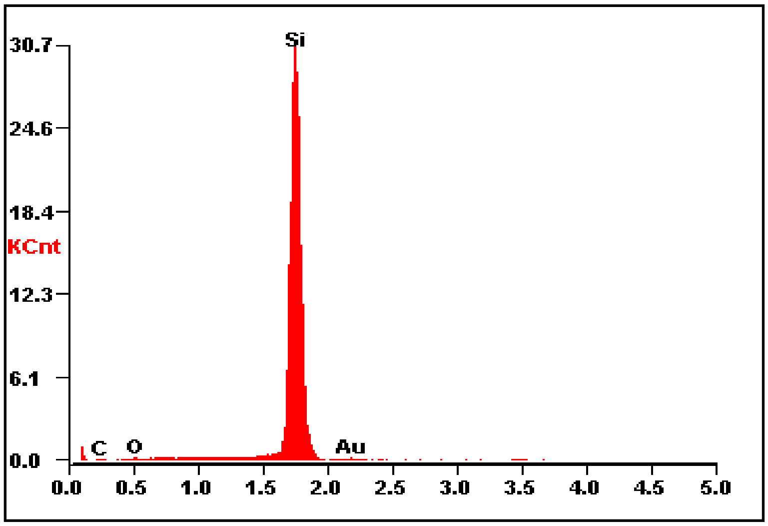

(b) Silicon AFM probe

Figure 2.5: SEM EDAX of a silica and silicon AFM probes. A strong Oxygen peak is clearly shown (a), which will not exist in a silicon AFM probe (b).

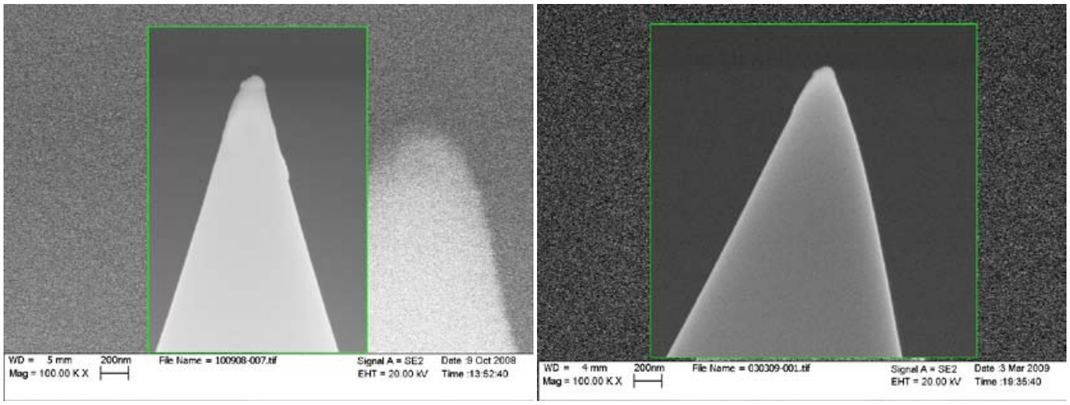

(a) (b)

Figure 2.6: SEM micrographs of the tip of an oxidized AFM probe (a) before and (b) after oxidization. These images obtained with the secondary electron detector were used to determine the tip radii of curvature of the oxidized AFM probes. The radii of curvature of tip before and after oxidization were 40.74 nm and 51.85 nm, respectively. The tip radius is shown to increase with oxidation exposure.

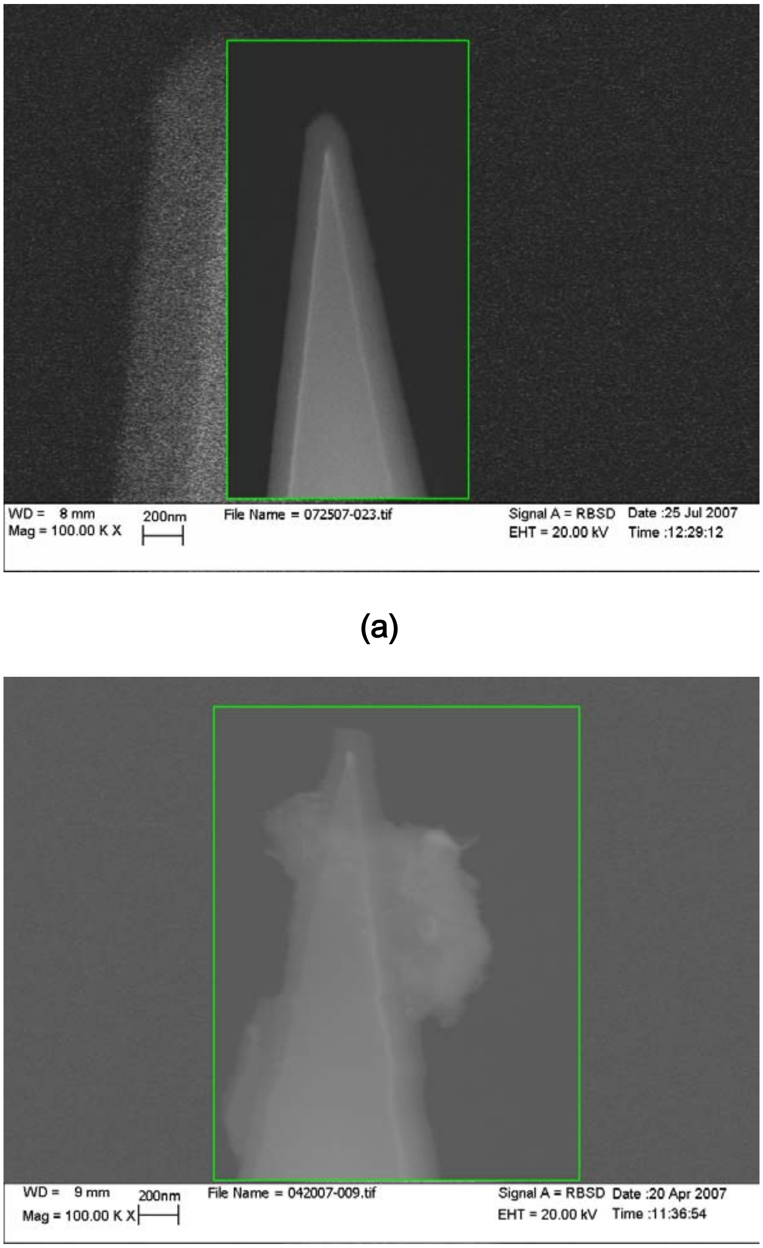

(a)

(b)

Figure 2.7: SEM micrographs of the diamond coated probe (a) to measure the radius of curvature and the thickness of the diamond coating and (b) to observe the tip wear after performing nanoscratch experiments.

2.4 References

2.1 Zhan Chen, and Rajiv K. Singh, Mechanism of Particle Deposition on Silicon Surface during Dilute HF Cleans, *Journal of The Electrochemical Society*, 150 (11) G667-G672 (2003).

2.2 D. Devecchio, P. Schmutz, and G. S. Frankel, *Electrochemical and Solid-State Letters,* 3 (2) 90-92 (2000).

2.3 F. Stevens, S. C. Langford, and J. T. Dickinson, Tribochemical wear of sodium trisilicate glass at the nanometer size scale, Journal of Applied Physics, **99**, 023529 (2006).

2.4 G. Huttl, D. Beyer, and E. Muller, Investigation of Electrical Double Layers on SiO_2 Surfaces by Means of Force *vs*. Distance Measurements, Surface and Interface Analysis, 1997, Volume 25, 543-547

Chapter Three

Application of Abrasive Particle Analogs to Oxide CMP

3.1 Application of nanoscale single particle analogs

In this work, AFM (SolverPro M, NT-MDT) is used to investigate the friction contribution of an individual nanoscale silica CMP polishing particle in contact with a compliant non-porous polyurethane polishing pad (JK111, Rohm and Haas), bulk silica and thermally grown oxide wafer (Wafernet) substrates during CMP polishing. Lateral force microscopy (LFM) is utilized with SiO_2 coated AFM probes, which act as an analog of the silica particle. To determine loads involved with experiments, normal spring constants of the cantilevers with oxidized AFM probes (discussed in Chapter 2) were evaluated by employing a thermal tuning technique developed by Hutter and Bechhoefer [3.1]. After the spring constant of an oxidized cantilever was determined, LFM experiments were performed with the AFM force lithography mode or AFM scanning mode on the samples for various normal loads and pH solutions to measure friction responses. This represents the friction contributions of 2-body contact between the nanoscale polishing particle and the CMP process materials such as an oxide wafer and a porous polyurethane polishing pad (IC1000). The load ranges were chosen to have a similar contact pressure during CMP and lateral forces were applied at a low speed to avoid hydrodynamic effects. The friction data was analyzed to observe the friction responses due to variation of applied normal loads and pH values.

Additionally, AFM force spectroscopy was performed during experiments or independently with the same environments to investigate the surface deformation during LFM experiments, which is used to determine the contributions of surface and adhesion forces to the friction results. At the macroscale, surface and adhesion forces are relatively insignificant because of a small area-to-volume ratio. Hertzian analysis is capable of predicting the pressure for various geometries in contact but it does not include adhesion forces. At the nanoscale, the ratio cannot be neglected because the magnitude of surface forces is at the similar order of magnitude as the external load applied at the interface. Thus, surface forces should be considered for the analysis of friction results at the nanoscale and has been discussed [1.23 – 1.25, 2.1, 3.2 – 3.3]. In this work, surface forces are estimated by calculating van der Waal and electric double layer forces between the silica AFM probe and the counterface materials. Adhesion forces are measured by utilizing the retraction force-distance curve obtained by force spectroscopy in solutions of varying pH. Effects of exposure time to solutions and pH environments on surface forces and adhesion forces are investigated, which are used to explain the effects on friction results and the contribution of pH variations. The resulting surface deformation measurements and friction responses can be used to develop accurate material removal models in oxide CMP.

When a friction model at the nanoscale is considered, the effect of surface forces on friction results should be considered as well. Short range surface forces are represented by the Johnson-Kendal-Roberts (JKR) model [3.4] while long range surface forces are represented by the Derjaguin-Muller-Toporov (DMT) model [3.5]. The intermediate cases are modeled by Carpick's transition model [3.6], which is based on Maugis' Dugdale model [3.7]. A nondimensional parameter in Carpick's model can be determined by observing friction data and the value of the parameter is designed to select a proper model for the data.

Thus, the friction data obtained by the single CMP particle analog can be used to determine the proper model for the friction data and estimate the friction response.

3.2 Background

3.2.1 Atomic Force Microscope (AFM)

Since invented by Binning in 1986, AFM has been utilized as an efficient method to obtain surface topographies down to atomic resolution and measure surface interaction forces. AFM is a high resolution scanning probe microscopes (SPM) which utilizes forces measured between a scanning probe and the surface of a sample. Figure 3.1 is a schematic of an AFM system which is composed of a laser, cantilever with a probe, photodiode, SPM controller and piezo scanner. The scanning probe is typically made of polysilicon or silicon nitride and has a tip radius of 10 nanometers. This probe is fabricated at the end of a micro-scale cantilever which is made out of the same material as the probe. The back side of the cantilever is generally coated with gold to increase the reflectivity and provide a greater intensity input to the photodiode. A photodiode is composed of four sections and its role is to sense the intensity of the reflected laser and convert it into an electrical signal. A piezo scanner controls the movement of a cantilever or a sample.

As an AFM probe tip rasters over the surface of a sample, the cantilever can either deflect or twist or experience both. Any change of the cantilever configuration causes the laser spot to be registered on a different location other than the original reference spot. The new location can be anywhere on the four quadrants of the photodiode. Cantilever deflection causes the vertical movement of the laser spot and the magnitude of deflection is determined by summing the laser intensities of the top and bottom quadrants. For the twist of a cantilever, the movement of the laser spot is horizontal and the laser intensities of left and the right quadrants are compared to generate a twist signal. The registered signals from the photodiodes are sent to a SPM controller to be used as feedback for the piezo-controlled scanner and as data for the control software to generate the topography of the surface and measure interaction forces between the probe and a substrate.

3.2.1.1 Normal spring constant calibration of an AFM cantilever

The normal spring constant of the fabricated probes was measured by a thermal tuning technique developed by Hutter and Bechhoefer [3.1] before each experiment. The AFM probe tip attached to the end of cantilever is modeled as a harmonica oscillator. The probe tip is considered as a sphere with radius R and with mass m. The cantilever is considered as a spring with a linear spring constant, *k*. Thermal fluctuation of the environment generates motions of the cantilever. The Hamiltonian of the system is expressed as

$$H = \frac{p^2}{2m} + \frac{1}{2} m {w_0}^2 q^2 \qquad (3.1)$$

where *p* is the momentum of the tip, w_0 is the resonant angular frequency of the system, and *q* is the displacement of the tip. By the equipartition theorem, the average value Hamiltonian can be described as

$$\left\langle \frac{1}{2} m {w_0}^2 q^2 \right\rangle = \frac{1}{2} k_B T \qquad (3.2)$$

where k_B is a Boltzmann's constant and *T* is the temperature.

Since ${w_0}^2 = k/m$, the equation above can be written again as

$$k = \frac{k_B T}{\langle q^2 \rangle}. \qquad (3.3)$$

However, thermal fluctuation is not the only source of the tip displacement. To filter out the contribution only due to the thermal fluctuation, the displacement data is plotted in the frequency domain. The power spectral density of the displacements has the shape of a Lorentzian line and the integral of it is equal to the mean square of the fluctuation in the time-series data. Then, the area under the curve with the background noise subtracted is the measure of the power spectral density of the displacements. The spring constant can be expressed as

$$k = \frac{k_B T}{P} \qquad (3.4)$$

where P is the area under the Lorentzian curve for the thermal fluctuations.

The thermal tuning model is employed by running a software script in the AFM analysis software (Nova version 972). The script requires two inputs: sensitivity of the cantilever and temperature of the surroundings in Kelvin. The sensitivity of the cantilever is measured by force spectroscopy. The force spectroscopy is performed on a rigid sapphire substrate which is cleaned with isopropyl alcohol and dried in laboratory air. It is assumed that there is no penetration of the cantilever into the surface of the sapphire substrate. After mounting the sapphire on the sample stage, an AFM cantilever is installed on the cantilever holder. Once the holder is mounted on the tip scanner, the laser and the photodiode are adjusted to achieve a proper signal response required for AFM operation. The head and the sample stage are isolated from an ambient laboratory environment by placing a specially designed metal hood to stabilize the experimental setup thermally and to minimize any possible noise from air flow or sound. The vibration from ground is minimized by an active vibration isolation system (Halcyonics Micro 40) where the AFM unit is housed. When the temperature inside the hood is stabilized, the temperature is measured by a digital thermometer. After reaching a thermal equilibrium inside the metal hood, the sample stage with a stepper motor is moved upward to bring the AFM probe in contact with the surface of the sapphire substrate in a contact mode. After scanning the surface briefly to verify that the probe is in good contact with the sapphire surface, force spectroscopy is performed to measure the cantilever sensitivity. The relationship between the cantilever displacement and the laser photodiode output is commonly referred to as the cantilever sensitivity and is necessary to determine the cantilever displacement during operation. The sensitivity is calculated by directly relating the z-piezo movement to the cantilever deflection, and is achieved by landing and lifting the probe onto and off of hard, stiff substrate (in this work sapphire is utilized). The force spectroscopy is composed of two steps: landing of the AFM probe onto a sample surface, and lifting the probe off the surface. Figure 3.2 shows typical force spectroscopy curves for approaching/landing (red line) and retracting/lifting (blue line). The vertical axis represents applied force and the horizontal axis represents tip-sample separation distance, thus the curve is known as the force-distance curve. Interaction forces between a probe tip and the surface of a sample can be extracted from this curve in terms of a separation distance. The sensitivity of a cantilever is determined by measuring the slope of either curve. In this work, the sensitivity is determined by averaging slopes of five Height-DFL data sets.

After obtaining the hood temperature and cantilever sensitivity, the scanner is switched to a semi-contact mode and the spring constant of the cantilever is obtained. A geometry correction factor ($k_{tri.} = 0.764 k_{rec.}$) determined by Stark et al. [3.8] using FEM was used for triangular cantilevers (used for the work in Chapter 4) because the thermal tuning method was developed for a rectangular cantilever. Once the spring constant is known, the lifting curve is utilized to determine the applied normal force and adhesion force. The load applied by an AFM probe to a substrate is generated through the bending moment of the polysilicon cantilever. When the AFM cantilever bends a pre-determined displacement, the load to achieve equilibrium can be calculated from elementary beam theory. Applied normal loads between the probe tip and the substrate are calculated by multiplying the spring constant by a distance that is measured from the force-displacement curve for a given DFL signal change.

3.2.1.2 Lateral Force Calibration Factor of an AFM cantilever

Lateral force calibration factor (α) is required to convert a lateral signal to a lateral force. One method to obtain it is to use geometry. The relationship between the lateral force (F_L) and twist angle (β) is given as [3.9]

$$F_L = \left(\frac{Ewt^3}{4l^3}\right)\left(\frac{l^2}{2h^2}\right)\left(\frac{h}{LB}\right)\beta \qquad (3.5)$$

h is the height of the probe and E, w, t, and l is the elastic modulus, width, thickness and length of the cantilever, respectively. $\frac{Ewt^3}{4l^3}$ is the normal spring constant measured from geometry. Since the value E and t are difficult to determine, it can be obtained numerically after determining the normal spring constant with the thermal tuning method describe in section 3.2.1.1. $\frac{l^2}{2h^2}$ is the ratio of the lateral spring constant and the normal spring constant. $\frac{h}{LB}$ is the lateral sensitivity of the cantilever. L is the distance between the cantilever and photodiode and B is the response of the lateral signal for a given displacement of the photodiode. It can be obtained by moving the photodiode for a given distance and measuring corresponding change in lateral signal.

3.2.2 Surface forces at the nanoscale

In addition to the direct contact force between two surfaces in contact, there exist indirect surface forces for abrasive-wafer and abrasive-pad interfaces. Sokolov et al. [1.25] investigated the interaction between the surface of IC1000 polyurethane polishing pads (Rohm and Haas Electronic Materials CMP Technologies) and AFM tips composed of silica and silicon nitride in various pH environments. The silica tip was oxidized and the radius of the curvature of the tip was measured to be 250 nm. After performing force spectroscopy on the surface of the polishing pad, the approach force-distance curves were analyzed to obtain the surface potential of the polishing pad and the retracting force-distance curves to obtain the adhesion forces. The surface potential of the polishing pad was derived by applying the DLVO theory. The interaction force (F) between the tip and the surface of the pad is divided into two forces: the London-van der Waals force (F_{vdW}) and the electrical double layer force (F_{EDL}) [1.25, 3.2].

$$F = F_{vdW} + F_{EDL} \qquad (3.6)$$

The London-van der Waals force [3.10] is an attractive force and it can be expressed as the following assuming the tip geometry as parabolic or spherical asperity

$$F_{vdW} = \frac{AR}{6(d + d_0)^2} \qquad (3.7)$$

where A_{wsp} is the Hamaker constant between the abrasive and the wafer, r_p is the radius of the abrasive particle (51.85 nm) and z_0 is the equilibrium interatomic distance (0.5 nm) [1.25]. The Hamaker constant can be determined by combining laws, which relate the unknown Hamaker's constant to known ones. The Hamaker constant of the wafer-slurry-particle system (A_{wsa}) can be calculated from Hamaker constants of the wafer (A_w), slurry (A_s) and abrasive (A_a) as follows [3.11]:

$$A_{wsa} = \left(A_w^{1/2} - A_s^{1/2}\right)\left(A_a^{1/2} - A_s^{1/2}\right). \qquad (3.8)$$

The values of A_w and A_a are the same as $6.5 \times 10^{-20}\,J$ [3.12] for this case and the Hamaker constant for the water ($A_s = 4.35 \times 10^{-20}\,J$) [3.2] is used for slurry. The Hamaker constant of the pad-slurry-abrasive system (A_{psa}) cannot be found with (3.8) because the Hamaker constant of the pad is unknown. Instead it was estimated by [3.13]

$$A_{psa} = \frac{3}{4}kT\left(\frac{\varepsilon_1 - \varepsilon_2}{\varepsilon_1 + \varepsilon_2}\right)\left(\frac{\varepsilon_2 - \varepsilon_3}{\varepsilon_2 + \varepsilon_3}\right) + \frac{3h\nu_e}{8\sqrt{2}}\frac{\left(n_1^2 - n_3^2\right)\left(n_2^2 - n_3^2\right)}{\left(n_1^2 + n_3^2\right)^{1/2}\left(n_2^2 + n_3^2\right)^{1/2}\left\{\left(n_1^2 + n_3^2\right)^{1/2} + \left(n_2^2 + n_3^2\right)^{1/2}\right\}}$$

(3.9)

where k is Boltzmann's constant, h is Planck's constant, T is the temperature, ε is the dielectric constant of a medium, *n* is refractive index of the medium in the visible, ν_e is the main electronic absorption frequency in the UV (typically 3 x 10^{15} s^{-1}). In this work, the dielectric constant (ε = 3) and the refractive index (n = 1.5) of the pad was approximated by that of the polymer.

The electrical double layer force is divided into two parts. For the surface potential less than 30 mV, the linear approximation is used and the form is given as [1.25]

$$F_{EDL,LA} = 28.91R\sqrt{M}\psi_1\psi_2 \exp\left(-\sqrt{M}\,\frac{d+d_0}{0.302\times10^{-9}}\right) \qquad (3.10)$$

where M is the molarity of the background solution and Ψ_1 and Ψ_2 are the surface potentials of the material 1 and 2. For the surface potential greater than 30 mV, the weak overlap approximation (WOA) is used and it is expressed as the following [1.25]

$$F_{EDL,WOA} = 0.303R\sqrt{M}\,\tanh\left[\frac{\psi_1}{0.103}\right]\tanh\left[\frac{\psi_2}{0.103}\right]\times\exp\left(-\sqrt{M}\,\frac{d+d_0}{0.302\times10^{-9}}\right). \qquad (3.11)$$

For this work, the weak overlap approximate was used to estimate the electrical double layer force because the magnitude of the zeta-potential of the pad and silica was over 30 mV. It is worthwhile to establish relationship between the surface potential and friction in CMP for various pH environments.

3.2.3 Modeling of friction between a single particle/asperity and surface

It has been well know that understanding of the contact area between two surfaces is a way to establish a relationship between normal loads and the corresponding friction loads [3.6]. In a continuum model, Hertzian analysis predicts contact areas of various geometries without considering surface forces at the interface. For a nanoscale contact area, the surface force cannot be neglected because of a high area-to-volume ratio, which means the magnitude of surface forces is comparable to the external load applied at the interface. Thus, the Hertzian analysis alone is not enough to describe the nanoscale contact area for AFM, so the analysis should include the surface forces.

When the probe tip is assumed to have a parabolic or spherical geometry with radius of R and the sample surface is assumed to be an infinite half-surface, the surface forces in nanoscale can be analyzed by three models: Johnson-Kendal-Roberts (JKR) model [3.4] for short range forces, Derjaguin-Muller-Toporov (DMT) model [3.5] for long range forces and Maugis model [3.7] for intermediate case. The JKR model is for the contact between a tip with large radius and a compliant substrate involving strong adhesion forces while DMT model is for tip with small radius and a stiff substrate involving weak adhesion forces. The Maugis model is derived from the Dugdale potential. Maugis defined a non-dimensional transition parameter (λ), which is a function of constant adhesive stress, tip radius, work of adhesion, the tip and sample elastic moduli and the tip and the sample Poisson ratios. The JKR model is appropriate for analysis for λ greater than 5 and the DMT model for λ smaller than 0.1. Otherwise, the transition model should be applied.

The contact areas estimated by Hertzian, JKR, DMT and intermediate models as a function of load depends on the surface forces. The Hertzian model has zero contact area when no external load (L) is applied. However, the other three models have non-zero contact areas even without any applied external load because of the negative loads presented in the plot. The negative load is an adhesion force, which is a critical load (L_c) required to separate the two surfaces. The ratios between the contact radius at non-zero load (a) and contact radius at zero load (a_0) for JKR and DMT are defined to be

$$\frac{a}{a_{0(JKR)}} = \left(\frac{1 + \sqrt{1 - L/L_{c(JKR)}}}{2} \right)^{\frac{2}{3}} \qquad (3.12)$$

and $\frac{a}{a_{0(DMT)}} = \left(1 - L/L_{c(JKR)}\right)^{\frac{1}{3}}$ (3.13)

, respectively. Carpick [3.6] introduced another non-dimensional parameter (α) to combine the two equations into a generalized transition equation as follows

$$\frac{a}{a_{0(\alpha)}}=\left(\frac{\alpha+\sqrt{1-L/L_{c(\alpha)}}}{1+\alpha}\right)^{\frac{2}{3}}. \qquad (3.14)$$

The equation becomes identical to JKR or DMT descriptions for α = 1 or 0, respectively. In the Maugis model, the relation between the contact area and the load is obtained by solving complex equations simultaneously, which are expressed in terms of parameterized non-dimensional variables for contact area ($\hat{a}$) and load ($\hat{L}$). Carpick et al. solved the complex equations for different values of λ and fitted the solutions with the results obtained from the generalized transition equation by choosing optimized α values for all values of λ's. By tabulating the values of λ's and corresponding α's, the empirically fitted relation between and λ and α is found to be $\lambda=-0.924\cdot\ln(1-1.02\alpha)$. In addition, the associated values of $\hat{L}_c$ and $\hat{a}_0$ to each value of λ is tabulated as well and the critical load ($\hat{L}_c$) and the contact radius at zero load ($\hat{a}_0$) is expressed with λ as below

$$\hat{L}_c(\lambda)=-\frac{7}{4}+\frac{1}{4}\cdot\left(\frac{4.04\cdot\lambda^{1.4}-1}{4.04\cdot\lambda^{1.4}+1}\right) \qquad (3.15)$$

and $\hat{a}_0 = 1.54 + 0.279 \cdot \left(\frac{2.28 \cdot \lambda^{1.3} - 1}{2.28 \cdot \lambda^{1.3} + 1} \right)$ (3.16)
.

The generalized transition model can be used to explain friction load as a function of normal load. It is assumed that friction is a linear function of contact area, so the friction force (F_f) can be expressed as the following

$$F_f = \tau \cdot \pi \, \mathrm{A_r}^2 \qquad (3.17)$$

where τ is the constant shear strength for the interface and *Ar* is the real area of contact. In the case of contacts that occur with multiple asperities or produce wear due to friction, this assumption may be not valid. Once the data of friction load or contact area as a function of applied normal load is obtained, the data can be fitted with the generalized transition equation to find the contact radius at zero load (a_0), the critical load (L_c) and α. Then, the value of α can be used to find the corresponding λ. This can lead to the determination of the interfacial energy (γ), which is necessary to calculate the contact area.

3.3 Experiments

3.3.1 Materials

AFM scans were performed on three materials: compliant non-porous polyurethane polishing pad material (JK111), bulk silica, and thermally grown oxide wafer substrates. JK111 is a non-porous bulk polyurethane pad and has an RMS roughness of 60 to 100 nm as measured by AFM. Figure 3.3 shows topographies of the pad, which possesses abrasion ridge obtained by (a) interferometer and (b) AFM. JK111 provides an analog of the flat region of porous polyurethane CMP polishing pads (IC1000), which is widely used in CMP processing. The IC1000 pad polishes during CMP by interacting at the pad asperity and the substrate, where abrasive particles are interacting with the surfaces. Pad asperities are the regions found between the surface pores in the IC1000. The roughness of these asperities is ~ 0.25 to 1 μm as measured by optical interferometer. The pore size of IC1000 is approximately 50 μm in radius and typically 5 μm in depth and the overall RMS roughness of IC1000 is 6 – 8 μm. Three dimensional topography of IC1000 and the surface profile were obtained with an optical interferometer and presented in Figure 3.4 (a) and (b), respectively. The bulk silica substrate is an analog of an oxide layer and has an

RMS roughness of 0.35 nm. Figure 3.5 is a three dimensional topography of the bulk silica substrate obtained with AFM. The image of the thermally grown oxide wafer is shown in Figure 3.6 and it has an RMS roughness less than 0.1 nm.

3.3.2 Procedure

All samples were cleaned with either isopropyl alcohol or by a portion of SC1 cleaning to remove organic contaminants. Alcohol cleaning process was implemented by submerging the samples in isopropyl alcohol for 2 hours and then drying in air. The SC1 cleaning a multi-step procedure. The cleaning solution was prepared by mixing 1 part of fully concentrated NH_4OH (28%), 1 part of fully concentrated H_2O_2 (30%) and 5 parts of deionized (DI) water **[3.14]**. The samples were dipped in the solution for 60 minutes and they were agitated for 15 seconds every 5 minutes. The samples were then rinsed in DI water for 4 minutes agitating for 15 seconds every 2 minutes. DI water rinse was repeated, and air-dried.

Once the normal spring constants of the cantilevers were measured in laboratory air, they were placed on the glass cantilever holder for LFM in liquid. Force spectroscopy was performed before friction measurements to obtain force-distance curves for surface and adhesion forces. Friction measurements were performed with either AFM force lithography mode or AFM scanning mode. The scanning distance was 1 μm with a speed of 0.1 μm/s. Normal loads ranging from 10 nN to 60 nN were applied to observe the cantilever twist response by measuring the lateral photodiode signal output. The testing solutions were made from 0.1 M NH_4OH with pH values of 7, 9, 10 and 11. NH_4OH is one of the most widely used slurry solutions in CMP. The pH variation was chosen to investigate the effect of pH on lateral responses.

3.4 Results and discussions

3.4.1 Surface deformation

3.4.1.1 Determination of Surface Deformation

To determine the deformation of sample surfaces during LFM, AFM force spectroscopy was performed before each LFM experiment or force spectroscopy experiments for all three samples were performed independently. The surface deformation is typically determined by subtracting the cantilever deflection measured on a stiff sapphire substrate for a given load from the cantilever deflection measured on the samples for the same load as demonstrated by Murakoshi et al [3.15]. Figure 3.7 describes how to analyze the force-distance curve for different situations. For the case of the stiff sapphire substrate (see Figure 3.7 (a)), the cantilever deflection ($DFL_{cant.}$) is identical to the cantilever movement ($MOV_{cant.}$):

$$MOV_{cant.} = DFL_{cant.} \qquad (3.18).$$

For the case of the compliant sample surface (See Figure 3.7 (a)), larger cantilever movement is required to obtain the same amount of the cantilever deflection as in the sapphire case due to the penetration of the probe tip into the sample surface (surface deformation due to direct contact, SD_{direct}):

$MOV_{cant.} = DFL_{cant.} + SD_{direct}$ (3.19).

The difference between the two equations above gives the surface deformation due to direct contact. The difference can be visualized by the slopes of the two curves. The slope obtained from the stiff substrate is larger than that from the compliant substrate. Thus, slope of the force-distance curve is a good indicator of change in the surface stiffness.

It has to be noted that the surface deformation obtained by the Murakoshi method does not include the effect of surface forces. At the vicinity of the contact point, cantilever deflection due to surface forces (DFL_{SF}) should be included as following:

$MOV_{cant.} = DFL_{cant.} + SD_{direct} + DFL_{SF}$ (3.20).

Attractive surface forces cause snap-in of the cantilever onto the surface of a sample. Larger cantilever movement is required to reach a required cantilever deflection (See Figure 3.7 (b)). Repulsive surface forces bend the cantilever before making a contact between the two surfaces. If the surface deformation is measured with the Murakoshi method, this is added to the measurement (See Figure 3.7 (b)). Thus, the surface deformation includes the effect of surfaces forces on the cantilever at the vicinity of the contact point.

3.4.1.2 Surface Deformations of Three Samples by the Silica AFM Analog

The surface deformation of the polyurethane pad (JK111), bulk silica and thermal grown oxide wafer samples for various pH environments (pH 7, 9, 10 and 11) and a normal load (50 nN) were shown in Figure 3.8, which was measured without considering the surface forces. In the case of the pad, the deformation at pH 7 (5.160 nm) was measured to be larger than the Hertzian estimation (3.961 nm), so the difference was 1.199 nm. The deformation increased from 5.160 nm to 13.969 nm gradually with increasing pH showing the increase of 8.809 nm due to pH. For the bulk silica and thermally grown oxide wafer substrates, the deformations at pH 7 were 0.945 nm and 0.017 nm, respectively. The deformation estimated from the Hertzian contact was 0.275 nm. The deformation differences between pH 7 and pH 11 for the bulk silica and thermal grown oxide wafer were 5.849 nm and 3.543 nm, respectively. In the case of the bulk silica substrate, the deformation at pH 9 showed a significant increase. The deformation at pH 10 was similar to the deformation at pH 7 but the deformation jumped to 6.794 nm at pH 11. A similar trend was observed with the thermally grown oxide. For this case, noticeable deformations were observed at pH 10 (2.433 nm) and 11 (3.560 nm) showing increase of the deformation with pH. The negative surface deformation at pH 9 is introduced because the error in the cantilever deflection obtained from the sapphire substrate was larger than the surface deformation of the thermally grown oxide wafer at pH 9. Thus, the actual deformation is close to zero. The deformations of the bulk silica substrate were smaller than the deformation of the pad in the same environment because silica has higher elastic modulus (70 GPa) than polyurethane (500 MPa).

3.4.1.3 Effects of pH on Surface Deformation Measurement

For all three samples, the same 50 nN normal load was applied, which means the increase of the surface deformation in each sample was caused by the pH variation of the solution. There are three possible effects of pH on the deformation results: (1) softening of the pad, (2) softening of the silica material (the probe, bulk silica and thermally grown oxide wafer substrates) and (3) variation on the interaction forces between the probe and counterface materials. The first and second factors affect the actual deformation of the three samples. The third factor contributes to the final surface deformation measurement. However, the deformation measured by this factor is not an actual deformation of the samples. Thus, deformation caused by this has to be taken out from the final deformation.

3.4.1.3.1 Effect of pH on the Pad

Softening of the pad applies only to the deformation of the polishing pad. The surface deformation of the pad will increase if the pad is softened with increase of pH. Figure 3.9 compares force-distance curves for the pad near the contact point at two different pH values (pH 7 and pH 10). When the two slopes were compared, the slope of the pad at pH 11 was shallower. This indicates that the pad was softened at higher pH. According to Obeng et al. [3.16], the hardness of IC1000 pad decreased with increasing pH. Thus, softening of the pad contributes to the surface deformation increase. However, when the force spectroscopy was performed on the pad with silicon tip, an opposite results was observed. Figure 3.10 shows the deformation of the pad obtained by performing force spectroscopy with an unoxidized silicon AFM probe (35.185 nm curvature radius) under 50 nN normal load for various exposure times and pH environments. When the error bars were considered, it seemed that there was no noticeable effect of exposure time on the surface deformation for each pH environment. Differences might have caused due to the rough surface of the sample. To observe the effect of pH, deformations of all exposure times are averaged for each pH and plotted in Figure 3.11. The surface deformation was the largest at pH 9 and decreased with increasing pH. This means the surface is stiffened with pH for the case of silicon probe. This will be explained in section 3.4.1.4.

3.4.1.3.2 Effect of pH on Silica Materials

Second, softening of the silica materials applies to the deformation of all three samples because it affects the silica substrates (bulk silica and thermally grown oxide wafer) as well as the silica-coated AFM probe. Chemical reaction between a silica surface and NH_4OH of the slurry breaks Si-O bonds and transforms a hard silica layer to a soft gel-like hydroxylated layer through the diffusion of water into the oxide layer [1.3]. This breaking of Si-O bonds is caused by a reversible depolymerzation reaction [1.22]. Siloxane bonds (Si-O-Si) of the silica surface reacts with water producing silanol, $Si(OH)_4$ as shown below:

$$(\mathrm{SiO_2})_x + 2\mathrm{H_2O} \leftrightarrow (\mathrm{SiO_2})_{x-1} + \mathrm{Si(OH)_4}. \quad (3.21)$$

When the pH of a solution is higher than the isoelectric point (IEP) of silica (less than 2), the Si-OH bonds are separated following the reaction below:

$\mathrm{Si}-(\mathrm{OH})+\mathrm{OH}^{-}\rightarrow\mathrm{Si}-\mathrm{O}^{-}+\mathrm{H_2O}$ for pH > isoelectric point of silica.

This is how a hydroxylated layer is generated on the silica surface. It should be noted that the solubility of silanol increases significantly for pH greater than 10, which means softening is enhanced greatly at pH 10 and above. Evidence of silica softening is reported in the literature. The microhardness of silica glass decreased due to water diffusion [3.17] and the fracture strength of silica decreased when water content amount increased [3.18]. Nevot and Croce [3.19] observed that the silica density near the surface was lower than the bulk with grazing X-ray reflection. In addition, the evidence of physical modification of a silica surface at pH 10.5 was observed with transmission electron microscopy (TEM) by Trogolo and Rajan [1.28]. Thus, the formation of this gel layer exists at high pH and it can be a factor to increase surface deformations of all samples. In addition, larger surface deformation is expected when both probe and counterface are silica. Third, the interaction forces between the two surfaces can be a factor that affects the surface deformation for all three samples because the surface forces affects the cantilever deflection at the vicinity of the contact point and their magnitudes vary with pH.

3.4.1.3.3 Effect of pH on Surface Forces

3.4.1.3.3.1 Observation of Force-Distance Curve near the Contact Point

The effect of the surface forces on the surface deformation can be explained by observing the cantilever behavior near the contact point. One way to achieve this is to analyze the force-distance curve at the vicinity of the contact point. Figure 3.9 is an example of the cantilever deflections on the pad near the contact point at pH 7 and pH 10. At the vicinity of the contact point, the deflection is not linear because its deflection was not only affected by the applied normal load but also by the surface forces between the two surfaces. To investigate the effect of the surface forces at the contact point, the distance of the non-linear section was estimated by measuring the distance between the contact point and the point where linear section initiates as shown in Figure 3.9. The distance at pH 10 was longer than that at pH 7, which showed the effect of pH on the distance of the non-linear section. Figure 3.12 is a plot of the distances measured from the force-distance curves obtained by force spectroscopy with the oxidized silica AFM probe on the three samples for various pH environments. The general trend for all three cases was that the distance of non-linear section increased with pH. The bulk silica showed an opposite trend at pH 9 and pH 10. For the case of the bulk silica sample, the distance at pH 9 seemed to be overestimated while the value at pH 10 underestimated. This is why the corresponding deformations in Figure 3.8 are deviated from trend of others. The results showed that the distance for the pad increased by 6.844 nm while the distance for the bulk silica and thermally grown oxide wafer substrates increased by 4.623 nm and 3.384 nm when pH varied from 7 to 11. For the case of silicon probe, a similar trend was observed. The non-linear section distance obtained with the silicon probe on the pad for various exposure times and pH environments are presented in Figure 3.13. It was observed that the exposure time did not affect the distance of non-linear section. Since the exposure time was not a significant factor of the distance measurement of the non-linear section, the average of all exposure times for each pH is obtained (see Figure 3.14). The results showed that the distance for the pad increased by 2.049 nm while the distance for the bulk silica substrate increased by 1.904 nm when pH varied from 7 to 11.

3.4.1.3.3.2 Effect of pH on Force-Distance Curve

The increase of the non-linear section shown in Figure 3.12 and Figure 3.14 was caused by the increase of surface forces with pH. The most dominant interaction forces between the two surfaces are van der Waals and electric double layer (EDL) forces [1.25, 3.2], which is affected by the zeta potential of each material. The zeta potential represents the potential difference between the medium and surface of a particle, so the magnitude is used to determine the stability of colloids suspended in a medium. Sokolov et al. [1.25] derived zeta-potential of the pad from the force-distance curve between the silica AFM probe and polyurethane pad with AFM. For the calculation of the surface force that affects the force-distance curve, they considered two dominated surface forces: van der Waals and EDL forces. Sine the EDL force is a function of the zeta potential, fitting of the force-distance curve provides the values of the zeta potential for the pad surface. The results showed that the magnitude of the pad surface potential increased from 40 mV to 60 mV as pH varies from 7 to 10. This suggests that the surface becomes more repulsive with pH, which results in the increase of the non-linear section with pH. They also derived the surface potential of the silica, which had an isoelectric point at pH less than 2 and the magnitude of the zeta potential increased from 50 mV to 60 mV as pH increased from 7 to 9. This will lead to the increase of the cantilever deflection with pH as well.

It has to be noted that the distance of the non-linear section was mostly affected by the repulsive surface force. The force-distance curve did not show snap-in during approaching, which is an evidence of strong attractive surface force near the contact point. The van der Waals force between the silica probe and silica substrate was estimated to be 0.074 nN using (3.7). The attractive van der Waals force between the silica probe and the pad was estimated to be 0.900 nN. The Hamaker constant for the silica-NH_4OH-silica system was found using (3.8) while that for the silica-NH_4OH-silica system was found using (3.9). The repulsive electrical double layer force was calculated using (3.11). Both silica and pad have a similar zeta-potential as a function of pH. The force was estimated to be 9.395×10^{-4} nN at pH 7 and 0.114 nN at pH 11 showing significant increase with pH. This explains the dominance of repulsive surface at high pH. Another way to verify the dominance of the repulsive surface force is to investigate the behavior of pull-off forces with pH. When two bodies are in contact, it is necessary to apply a load to separate the two surfaces. An attraction force enhances the adhesion force while a repulsive force does opposite. Figure 3.15 shows pull-off forces required for the silica probe to be separated from (a) the pad and (b) thermally grown oxide wafer. For both cases, the pull-off forces decreased with pH, which means the repulsive force becomes a dominant surface force as pH increases. The same trend of pull-off force with pH for the pad was observed in the work of Sokolov et al. [1.25].

How a zeta potential can affect the surface force can be observed by comparing the non-linear section distances obtained by the silica and silicon probes. The non-linear section distances for the pad are compared in Figure 3.16 (a) while those for the bulk silica in Figure 3.16 (b). For both cases, the distance obtained with the silica probe was larger. Even though the zeta potential of the silicon showed the similar trend with pH, the magnitude increased only up to 40 mV as pH 12. The interface between the silicon probe and its counterfaces experiences smaller repulsive force. This result shows how the non-linear section distance is affected by the surface forces acting at the interface.

3.4.1.4 Estimation of Actual Surface Deformation

It has been shown that the surface deformation measured with the silica probe under 50 nN (see Figure 3.8) was overestimated because it did not include the effect of surface force. At pH 7, the effect is not significant. However, the surface deformation of the pad at pH 11 is overestimated by the increase of the surface force with pH, which contributes to the deformation by 6.844 nm. Thus, the cantilever deflection increased by the surface force was subtracted from the measured surface deformation and the actual pad deformation at pH 11 was estimated to be 7.125 nm, which was caused by the softening of the pad and the silica probe at high pH. In the same manner, the actual surface deformation of the bulk silica substrate was estimated to be 2.171 nm, which was produced by the simultaneous softening of the probe and the substrate. Since both probe and the substrate deform simultaneously for this case, only half was taken as the actual surface deformation for the silica substrate and it was estimated to be 1.086 nm at pH 11. For the case of thermally grown oxide wafer, the actual deformation was estimated to be 0.088 nm. Actual surface deformation for other conditions can be seen in Table 3.1. Determination of the actual deformation is important because it is directly related to the real area of contact. In addition, it can be used to determine the mode of friction (see section 3.4.2)

For the surface deformation of the pad measured with the silicon probe, the decrease of the surface deformation was caused by the increase of tip radius due to removal of the silicon at high pH. Even though the zeta potential of the silicon probe is lower than that of the silica probe, it is still repulsive. The surface deformation should increase due to this repulsive force. The increase of the surface deformation from pH 7 to pH 9 is caused by this or pad softening. However, the decrease of the deformation from pH 9 to pH 11 is caused by the increase of the tip radius. Figure 17 (a) and (b) compares the tip end before and after experiments. The radius increased from 35.185 nm to 48.15 nm after use. Based on Hertzian contact, the increase of the deformation due to tip radius of estimated to be 0.504 nm.

3.4.2 Plowing determination

The surface deformation is important because it is used to calculate the contact radius of two surfaces in contact. When considering friction, the knowledge about the contact radius is utilized to determine whether plowing friction contributes to global friction or not. Figure 3.18 is a schematic of a plowing friction. A stiff abrasive particle of radius *R* produces a groove of width *w* and depth *d* as it plows a soft substrate. When the ratio of the scratch width and the particle diameter (w/2R) is greater 0.2, the plowing can affect friction results significantly [3.20]. In this work, R is represented by the tip radius of the AFM particle analog. The depth of scratch (*d*) is estimated from the surface deformation results. The width of scratch (*w*) is twice of the contact radius estimated by the Hertzian contact between the particle analog and its counterface material. The contact radius (*a*) is determined by

$$a = \left(\frac{3}{8} \frac{R^* \bullet P}{E^*} \right)^{\frac{1}{3}} \qquad (3.22).$$

R* is the effective tip radius, which is defined to be $R^* = \frac{1}{1/R_1 + 1/R_2}$ where R_1 and R_2 is the radii of the body 1 and body 2, respectively. *P* is the applied normal load. *E** is the contact modulus, which is defined to be $E^* = \frac{1}{\frac{1-\nu_1^2}{E_1} + \frac{1-\nu_2^2}{E_2}}$ where ν_1 and ν_2 are the Poisson's ratio of the body 1 and body 2, respectively and E_1 and E_2 are the elastic modulus of the body 1 and body 2, respectively. The scratch depth (d) is determined

$$d = \frac{a^2}{R^*} \qquad (3.23).$$

The contact radius is estimated by using the parameters given in Table 3.2. It is assumed that the testing materials have a flat surface. The contact radii between the silica probe and the pad for 50 nN normal load and various pH environments were calculated using the actual surface deformations and are presented in Table 3.3. In addition, the ratio of w/2R for each pH environment is tabulated as well. The values of the ratio were greater than 0.3 for all pH environments, which means the plowing friction would contribute to the global friction results for pad and the contribution increases with pH. The same analysis is performed for the bulk silica substrate and the ratios are presented in Table 3.4. The silica surface does not experience significant plowing friction.

3.4.3 LFM results

3.4.3.1 Determination of Lateral Response

The friction response of the AFM cantilever during LFM is recorded for the pad, bulk silica and thermally grown oxide wafer samples under various normal loads and pH environments. As the particle analog scans the surface of the samples back and force, the lateral force signals in both directions were obtained. Figure 3.19 is an example of lateral responses of the cantilever for one complete scan cycle during LFM. The responses are in nA and measured as a function of a scanning distance. The negative (blue diamonds) and the positive (red squares) lateral response signals are obtained during forward and backward cantilever movements, respectively. The sign difference resulted from that fact the scanning direction of the two signals were opposite. The lateral responses shown in Figure 3.20 were obtained by scanning the pad at pH 10 for various normal loads (10, 20, 30, 40 and 50 nN). Each data point is the average of each scan line in one direction and a set of five data points represents each load. The friction signal increased with the load as expected. The actual lateral response was determined by calculating half of the signal difference as shown in Figure 3.20. The lateral signal is converted to the lateral friction using the lateral force calibration factor. It was obtained by the method described in section 3.2.1.2 and estimated to be 2.161 x 10^{-7} N/nA.

3.4.3.2 Effect of pH on Lateral Response

To see the effect of pH on the friction results, lateral responses of all three samples for varying solutions of pH under 50 nN were plotted in Figure 3.21. For the pad, the lateral response decreased with increasing pH from pH 7 to pH 10 and then increased from pH 10 to pH 11. As the hardness of the pad surface decreases with pH, the stress required to shear the pad surface decreases as well. The pad might have reached a critical condition environment at pH 11 as in the silica surface. Increase of contact area due to larger surface deformation will result in a significant increase of friction at pH 11. For the bulk silica and thermal grown oxide wafer substrates, the lateral response did not vary from pH 7 to pH 9 but started decreasing at higher pH values. The response was the smallest at pH 11 for both materials. This is caused by the formation of the gel layer at high alkaline environments. The decrease of friction with pH was also observed in actual CMP [1.22]. The results also showed that the lateral response experienced by the pad was larger than the other two samples because the plowing friction was added to the adhesive friction for the pad. The friction coefficients for the pad at 50 nN for pH varying from 7 to 11 ranged 0.131 to 0.181 while those for the bulk silica and thermally grown oxide wafer for the same conditions ranged 0.02 to 0.056. A Summary of friction coefficients of the three samples for pH environments under 50 nN are given in Table 3.5. A similar value of friction coefficient (~ 0.04) was observed by Taran [1.26] for the friction response between the colloidal probe and the silica wafer at pH 10.6.

3.4.3.3 Effect of pH on the Determination of Adhesive Friction Models

Since the friction at the silica-silica interface does not involve a plowing friction, the origin of friction is due to an adhesive friction. Considering the scale of friction, the surface forces are a possible source that can increase the global friction. Figure 3.22 shows the lateral responses of the cantilever with the bulk silica substrate for various loads and pH environments. The lateral responses at pH 7 and pH 9 were close to each other while the lateral responses at pH 10 and pH 11 were close to each other. The lateral responses at pH 10 and pH 11 were lower than those at pH 7 and pH9 due to formation of gel layer at high pH environments. Determination of a proper friction model for the silica lateral response results can be achieved by applying Carpick's generalized transition model. The first step is to determine the value of the parameters such as the transition parameter (α), lateral response at zero load ($F_{f,0}$) and pull-off force at zero load (L_c) based on the lateral responses. Since the lateral responses at pH 7 and pH 9 were similar, fitting was performed on the results at pH 7. The lateral response at zero load ($F_{f,0}$) was estimated from Figure 3.22 and the value was 0.279 nN. The pull-off force at zero load (L_c) was measured from the force-distance curve and the value was -0.449 nN. Based on these two parameters, the best fit was obtained with α = 1. Figure 3.23 compares the measured lateral responses at pH 7 with the estimated lateral responses with α = 1 and α = 0. When α = 0 was used, the estimated deviated more from the measured value. This means the proper friction model for the lateral responses at pH 7 and 9 is the JKR model. The same procedure was applied for the lateral responses at pH

10 and pH 11. For this case, the estimated lateral responses at zero load ($F_{f,0}$) at pH 10 and pH 11 from Figure 3.22 were 0.188 nN and 0.102 nN, respectively. This is expected because the pull-off force at zero load (L_c) is close to zero due to increased repulsive force at high pH values. When these two parameters were used for the estimation, it was shown in Figure 3.24 that the two extreme values of the transition parameters (α = 0 and α = 1) are not proper for fitting. There is no significant surface force effect on the lateral responses at pH 10 and pH 11, so the lateral responses cannot be analyzed the friction model that integrates adhesion at the interface such as JKR or DMT model. The data will be analyzed without the effect of surface forces.

3.4.3.4 Contact Area and Interfacial Shear Strength

For the lateral response results for the silica substrate at pH 7 and pH 9, the friction model was determined to be the JKR model. Due to existence of pull-off force, the contact area at zero load for the JKR model, $a_{0(JKR)}$, still exists, which is expressed as [3.6]

$$a_{0(JKR)} = \left(\frac{6\pi\gamma R^2}{E^*} \right)^{1/3} \qquad (3.24)$$

where γ is the interfacial energy per unit area (work of adhesion). Following the procedure given by Carpick, the contact area can be written as

$$a_{0(JKR)} = \left(-\frac{4RL_c}{E^*} \right)^{1/3} \qquad (3.25)$$

where L_c is the pull-off force measured from the force-distance curve at pH 7. The contact area was estimated to be 1.373 nm. It has to be noted that the contact area estimated by Hertzian at 50 nN was 7.502 nm only. Thus, the increase of contact area due to surface force will increase the friction force at pH 7 because the friction force is related to square of the contact area.

It was explained that the lower friction experienced by the silica surface at higher pH environment was due to formation of the silica gel layer on the surface at high pH. The softening can be explained by observing the difference of the interfacial strengths between the two surfaces at different pH values. For the case of the silica at high pH, the adhesive friction (F_f) is given as [3.21]

$$F_f = \tau_0 A_r + \beta P \qquad (3.26)$$

where τ_0 is the interfacial shear strength, A_r is the real area of contact, β describes the normal load dependency of the shear strength and P is the applied normal load. By fitting the friction-load data with (3.26), the interfacial shear strength was estimated to be 29 MPa for the silica surface at pH 7. The real contact area was calculated using (3.12). For the case of the silica at pH 10 and pH 11, the interfacial shear strength was measured by dividing the friction force by the contact area calculated from the Hertzian contact radius based on the measured actual deformation. The values were estimated to be 22 MPa for pH 10 and 7.9 MPa for pH 11. The decrease of the interfacial shear strength with pH means the decrease of the surface stiffness, which will result in lower friction. The increase of contact area and the highest value of the interfacial shear strength at pH 7 is why the lateral responses at pH 7 and pH 9 in Figure 3.21 are larger than those at pH 10 and pH 11.

3.5 Conclusion

In this chapter, AFM is used to study fundamental frictional response during CMP polishing. Silica coated AFM probes were used as the analog of a nanoscale individual silica CMP abrasive particle. Lateral force microscopy (LFM) is performed with the particle analogs to investigate the 2-body friction contribution of an individual silica CMP polishing particle in contact with the polishing pad and silica substrates for various normal loads and pH solutions. The deformations of all three samples were measured considering effect of pH on the pad, silica materials and surface forces. It was shown that the softening of the pad and silica materials due to increase in pH increased the surface deformation. In addition, the effect of surface forces on the measured deformation results was investigated to determine the actual surface deformation. To determine the friction mode involved in LFM experiments, the actual deformation of the pad, the bulk silica and thermally grown oxide wafer were measured for 50 nN at pH 11 and estimated to be 7.125 nm, 1.086 nm and 0.088 nm, respectively. The ratio between the contact radius and the tip radius showed that the plowing friction was dominant for the pad and the adhesive friction was dominant for the silica substrates, which should consider the increase of the contact area due to adhesion forces. The frictions of the pad, bulk silica and thermally grown oxide wafer at pH 11 under 50 nN were estimated to be 0.165, 0.028 and 0.016 nN, respectively. Largest friction coefficient was observed for the pad at the same pH due to plowing. The frictional response of the silica substrates decreased with pH due to formation of the silica gel layer. It was found that the proper friction model for the bulk silica substrate at pH 7 and pH 9 was the JKR model and the contact area estimated by the JKR model explained why the friction response was higher for these two cases. Since adhesion was observed for the case at high pH environments, it was determined that the frictional response for these cases could not be analyzed with the friction models based on pull-off forces.

Understanding of material removal mechanism in oxide CMP can be achieved by investigating the interaction between a single abrasive particle analog and substrates. This will lead to the development of proper models for material removal rate (MRR). MRR models based on a single particle should not use material responses obtained in global scale because the interaction between the particle and the substrate is not the same. The simulation of the contact in nanoscale can provide the information such as surface forces and the material responses (surface deformation and softened surface layer) directly, which cannot be obtained with a microindenter or mm scale balls. The surface deformations and surface forces measured with the particle analog can lead to a better understanding of friction in nanoscale. The measured friction coefficient and the effect of chemistry can be integrated into MRR models as inputs.

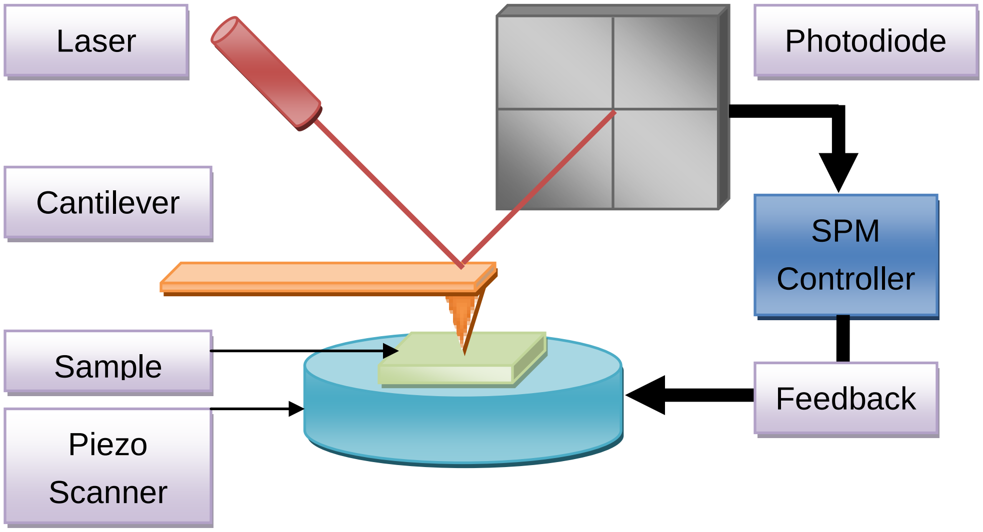

Figure 3.1: Schematic of an AFM.

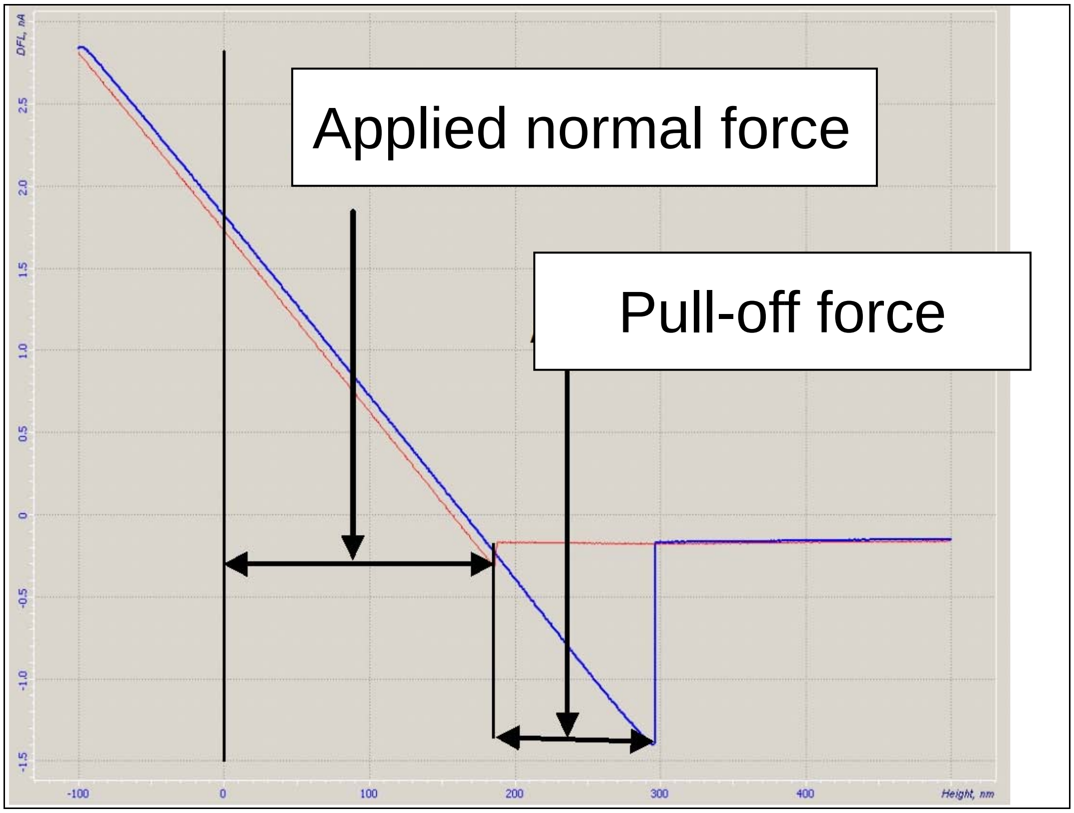

Figure 3.2: Typical force spectroscopy curve.

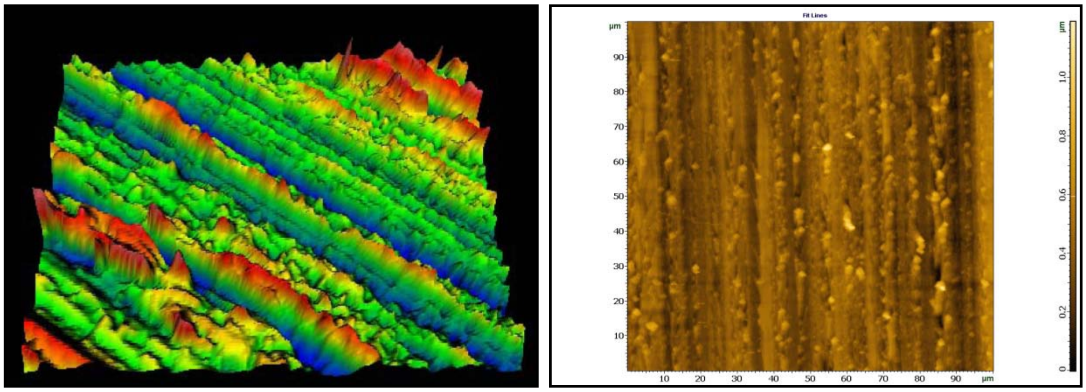

Figure 3.3: Topographies of the pad, which possesses unidirectional stripes, obtained by (a) interferometer and (b) AFM.

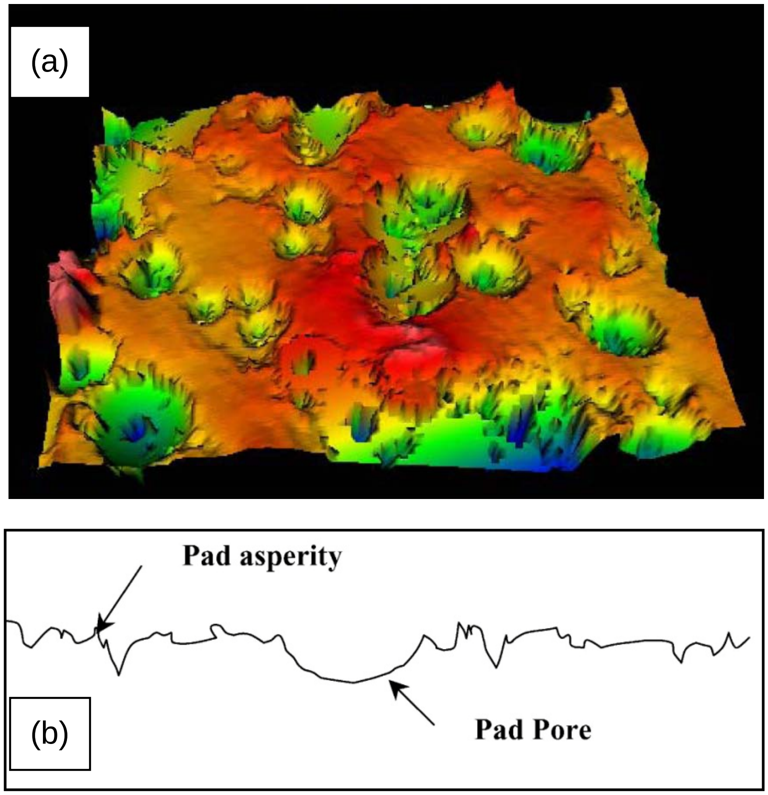

Figure 3.4: (a) Three dimensional topography and (b) surface profile of the IC1000 obtained by light interferometer.

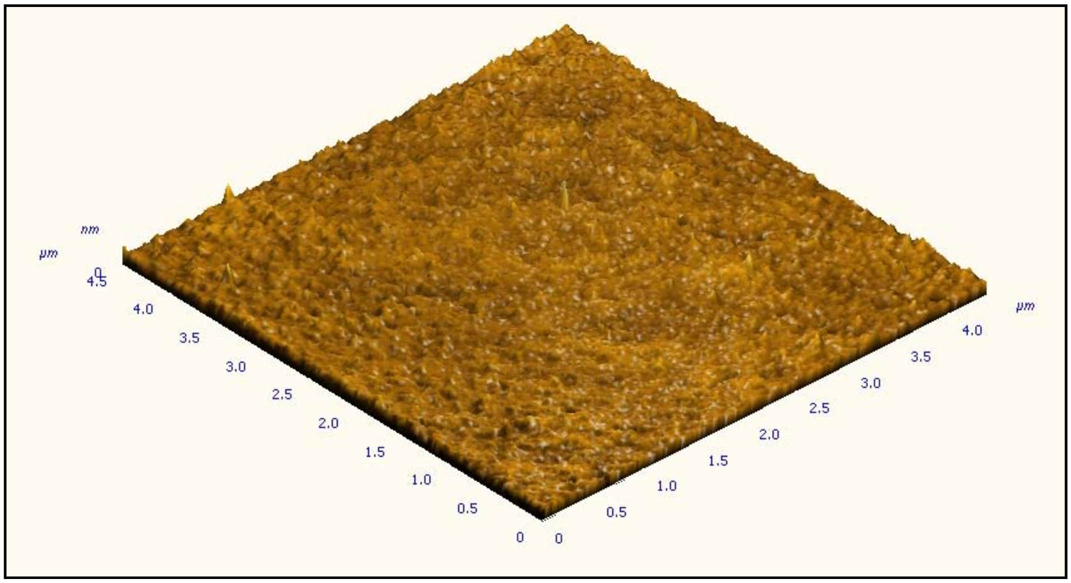

Figure 3.5: Three dimensional topography of the bulk silica substrate obtained with AFM. The bulk silica substrate is an analog of an oxide layer and this sample has the RMS roughness of about 0.35 nm (Scan size: 5 μm by 5 μm).

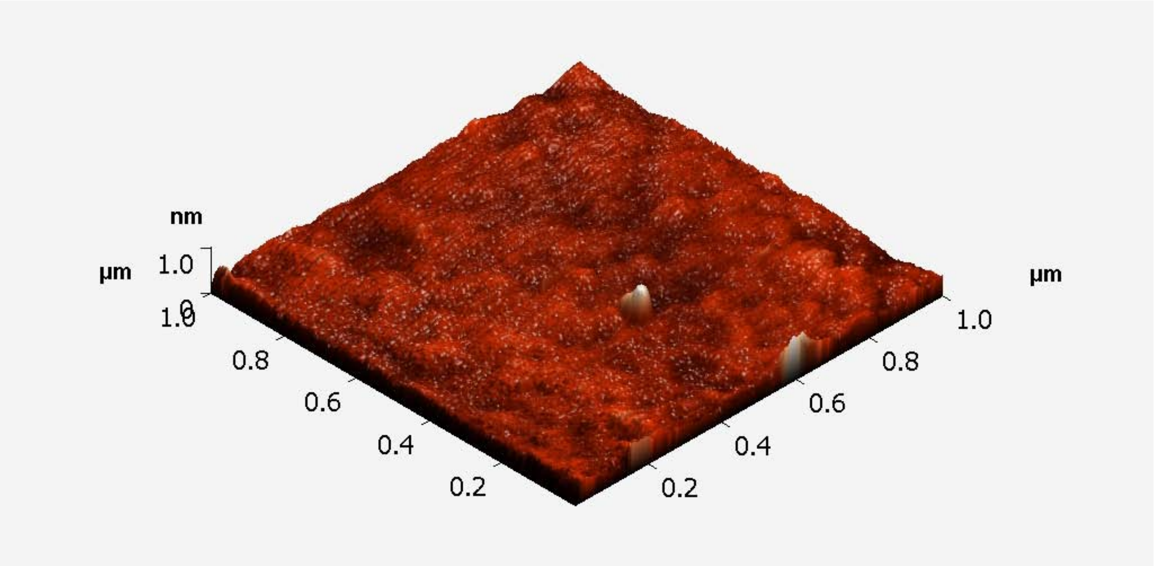

Figure 3.6: Image of the thermally grown oxide wafer obtained with AFM. It has the RMS roughness of about 0.0740 nm (Scan size: 1 μm by 1 μm).

(a) Surface deformation determination without surface force

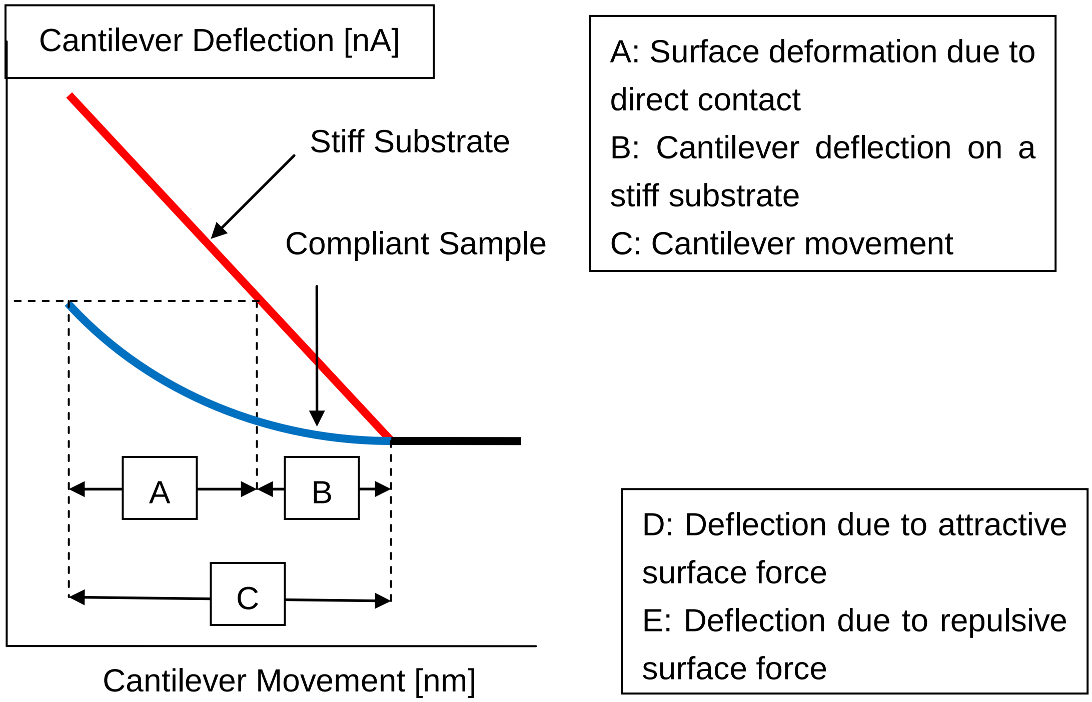

(b) Effect of surface forces on the cantilever deflection

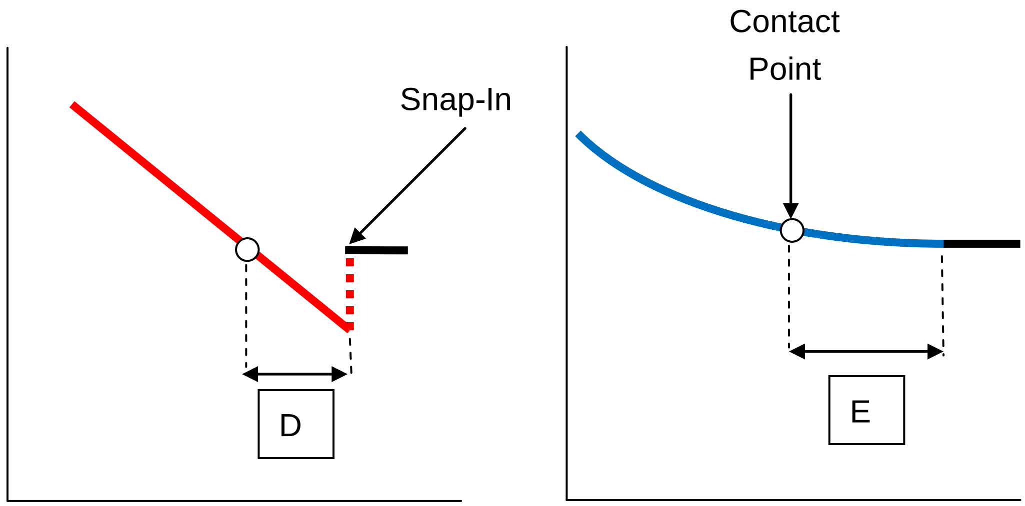

Figure 3.7: Determination of surface deformation (a) without and (b) with surface forces.

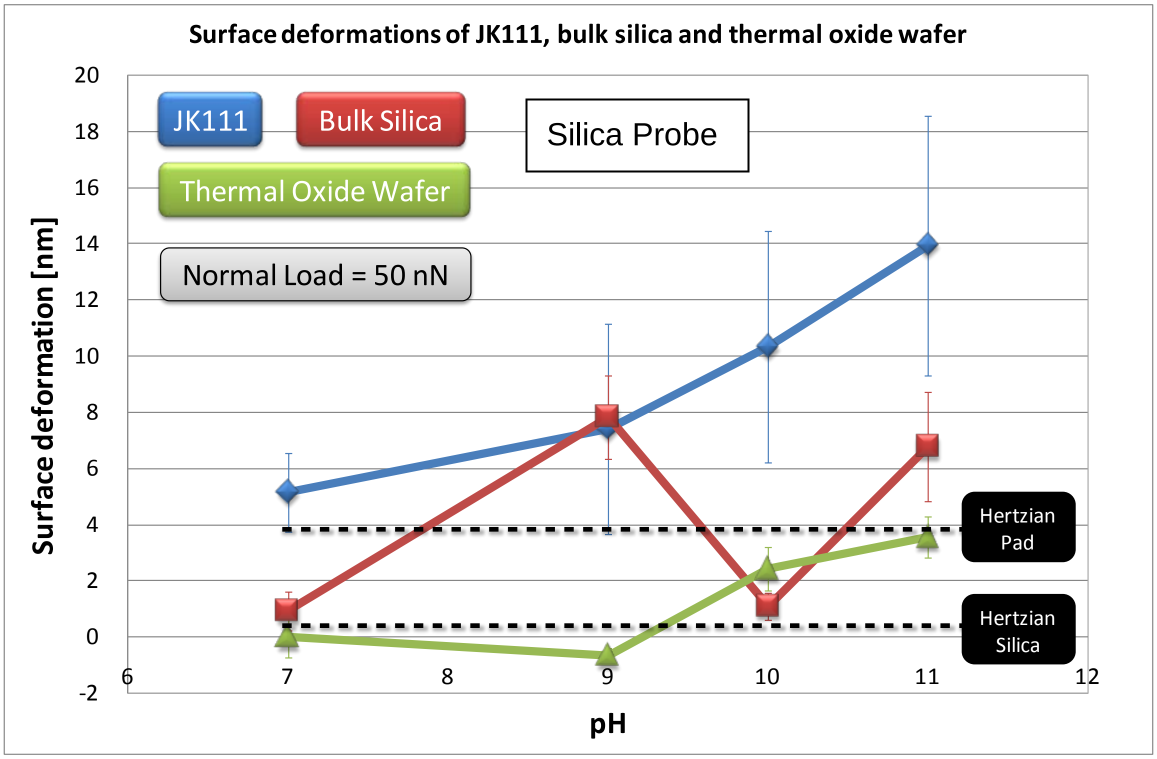

Figure 3.8: deformation of the pad, bulk silica and thermally grown oxide wafer surfaces with various pH environments under 50 nN normal load.

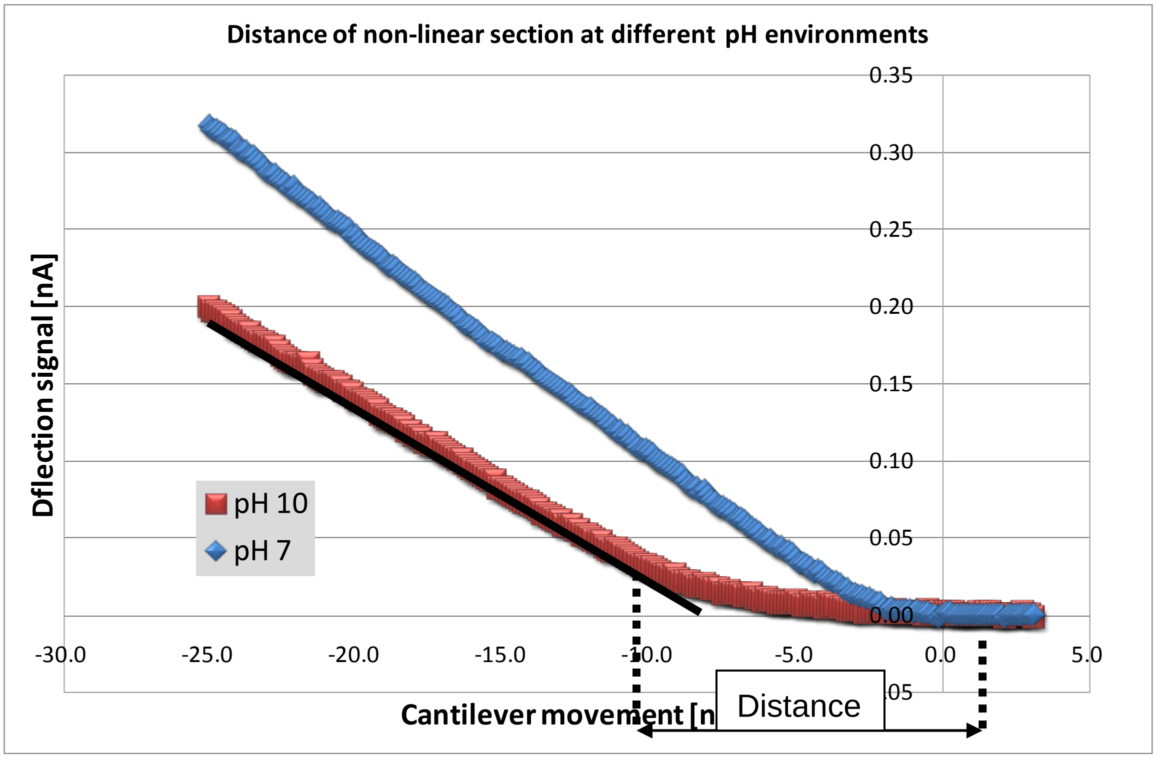

Figure 3.9: An example of the cantilever deflections on the pad near the contact point at pH 7 and pH 10.

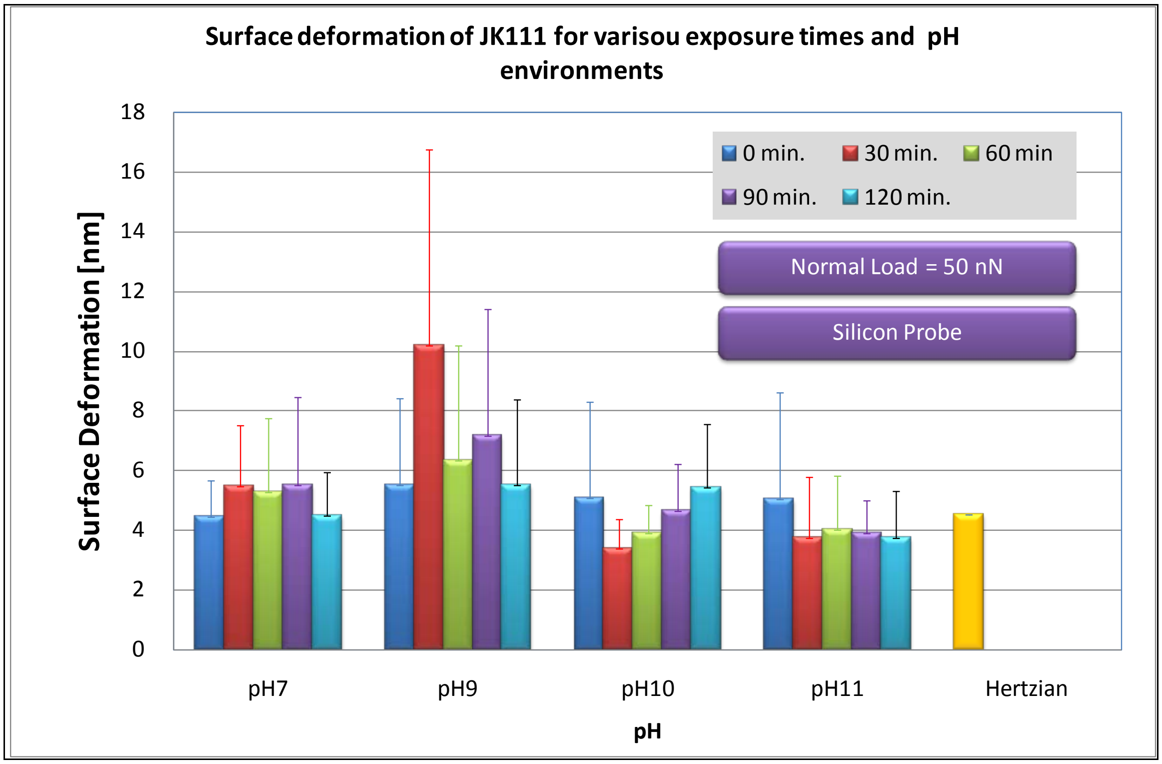

Figure 3.10: Surface deformations of JK111 for various exposure times and pH environments.

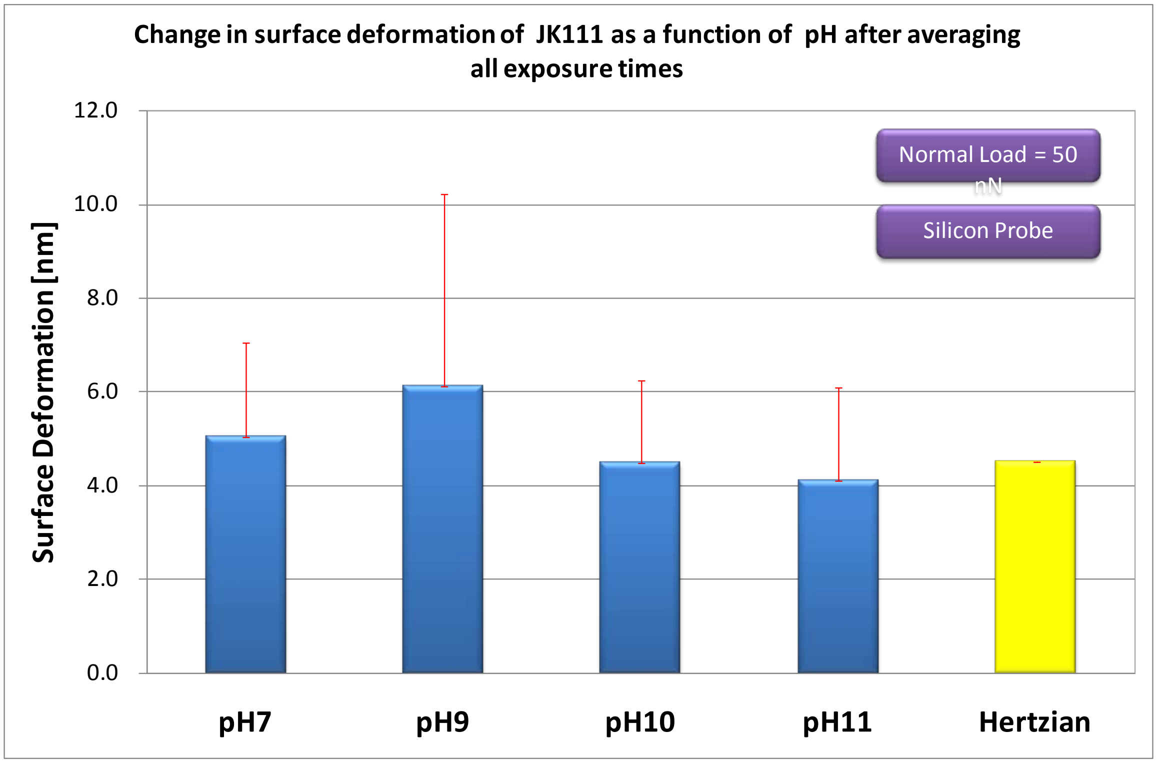

Figure 3.11: Surface deformations of JK111 as a function of pH after averaging all exposure times.

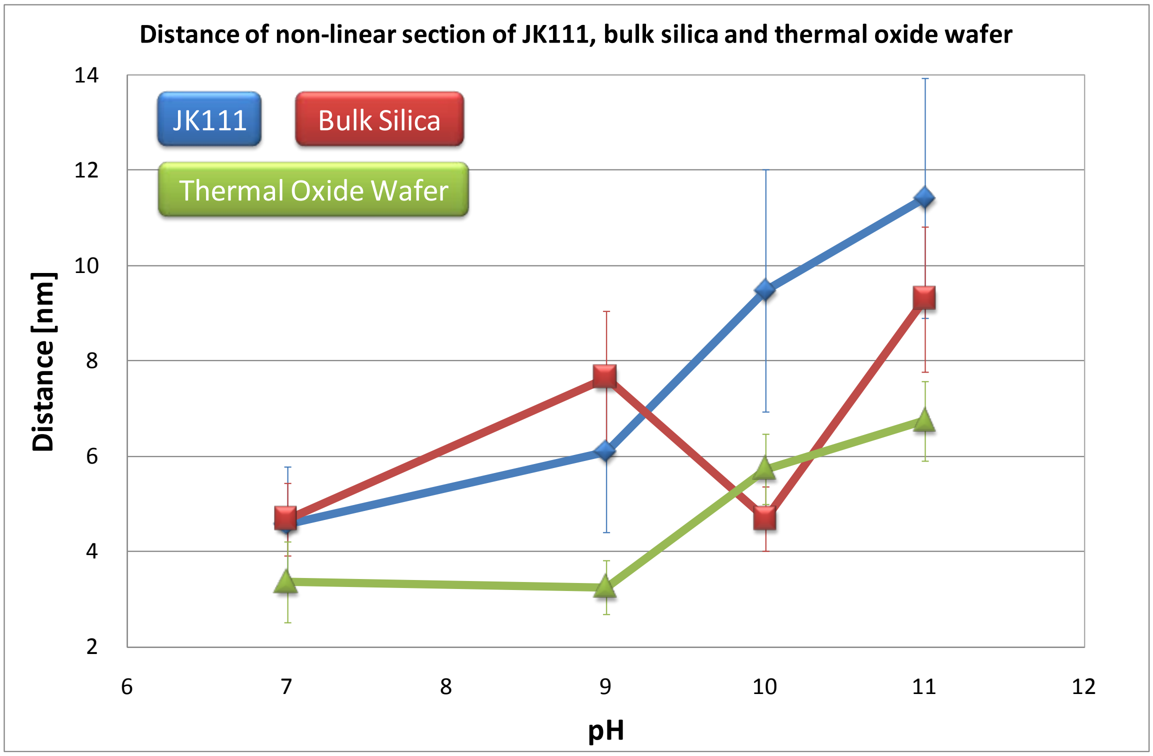

Figure 3.12: Distance of non-linear section near the contact point at various pH environments.

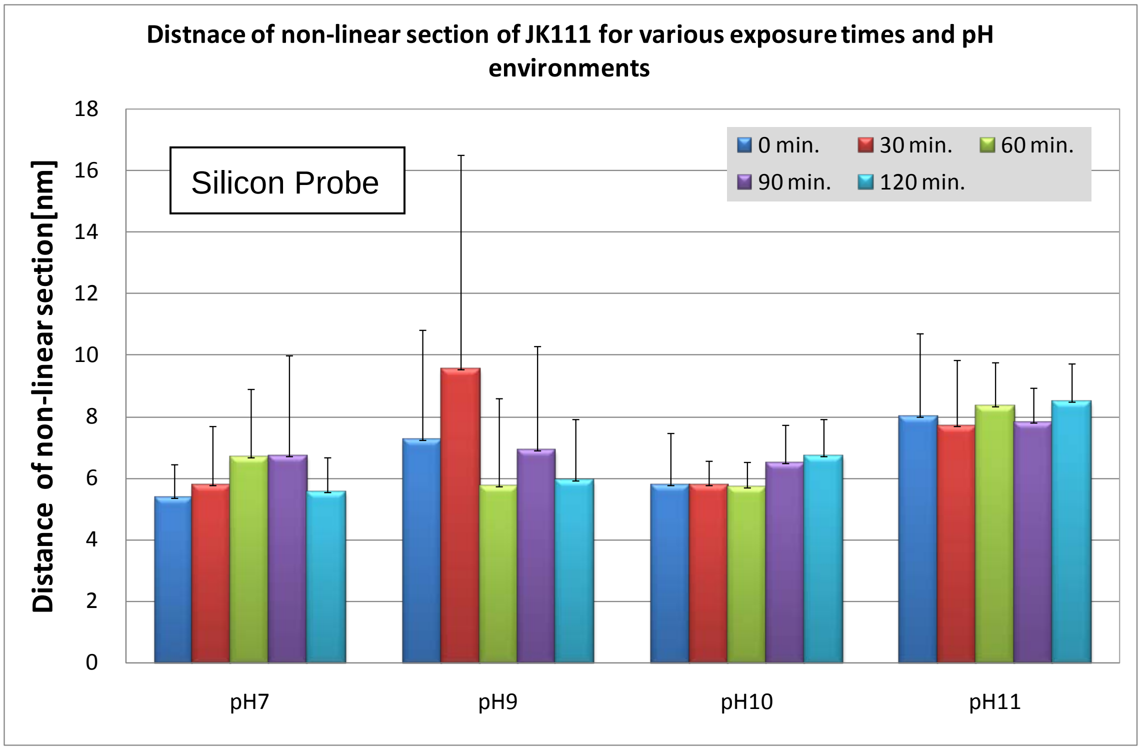

Figure 3.13: Distance of non-linear section of JK111 for various exposure times and pH environments.

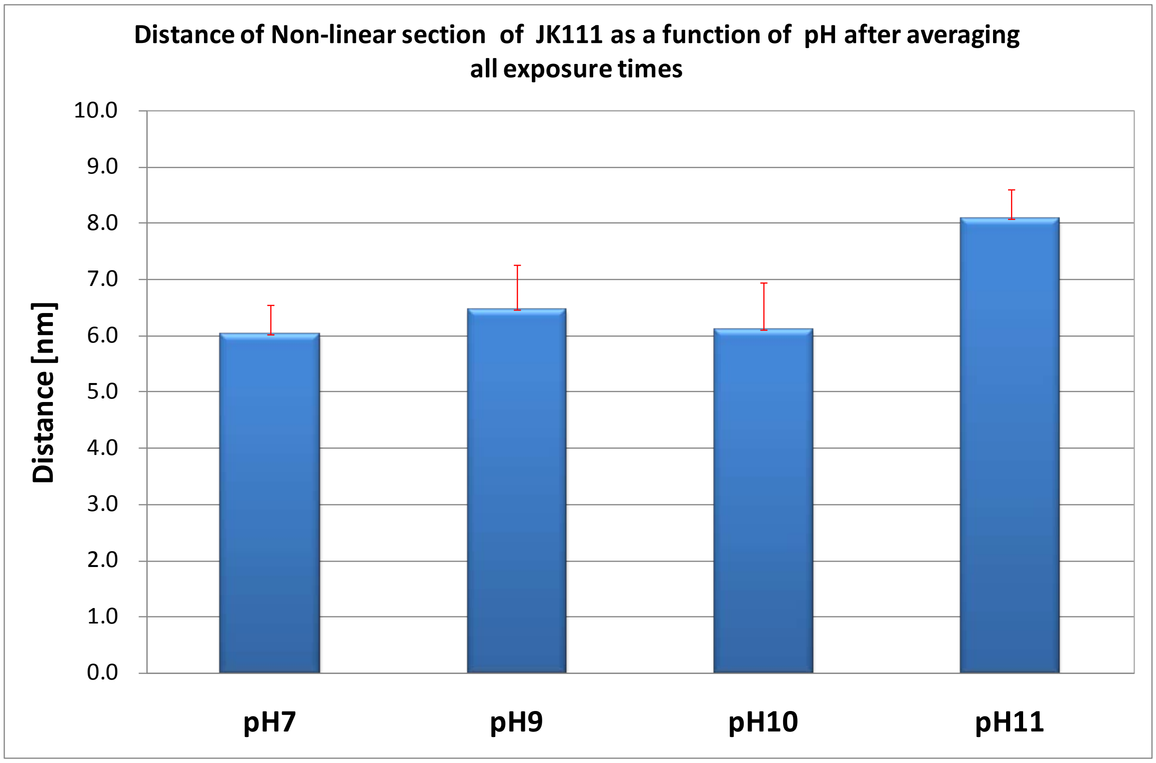

Figure 3.14: Distance of non-linear section of JK111 as a function of pH.

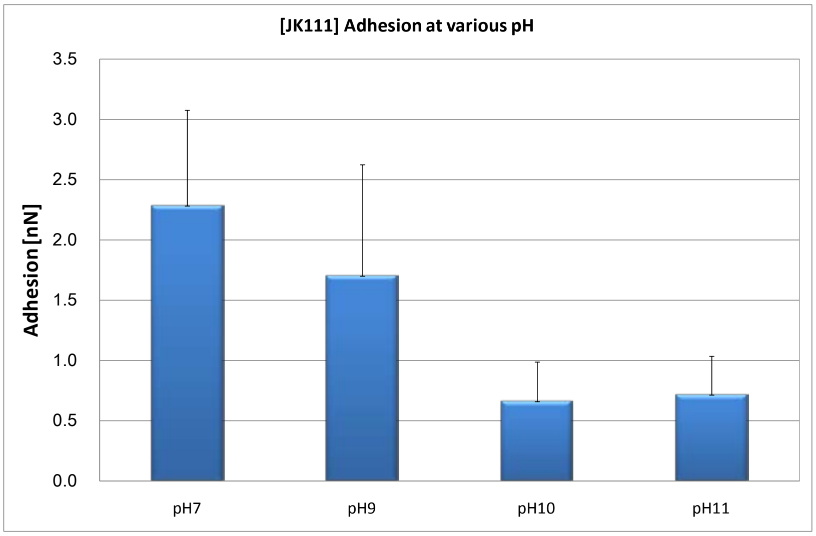

(a)

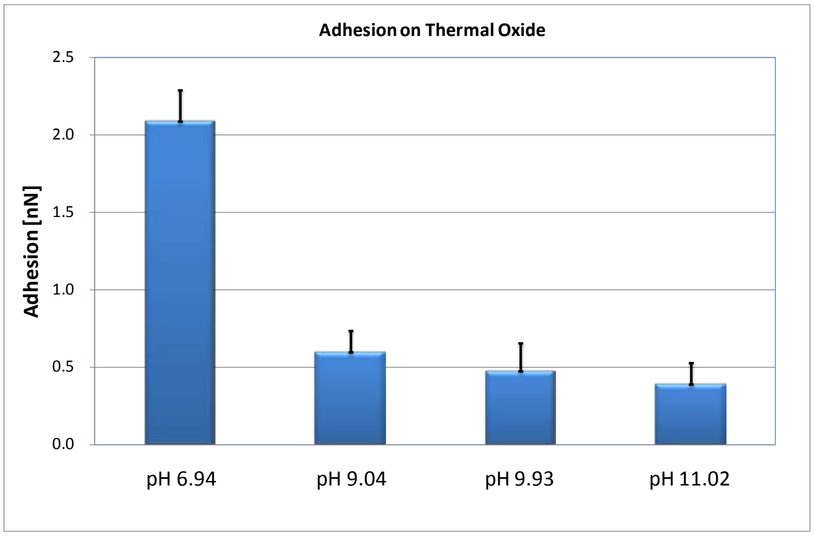

(b)

Figure 3.15: pull-off forces required for the silica probe to be separated from (a) the pad and (b) thermally grown oxide wafer.

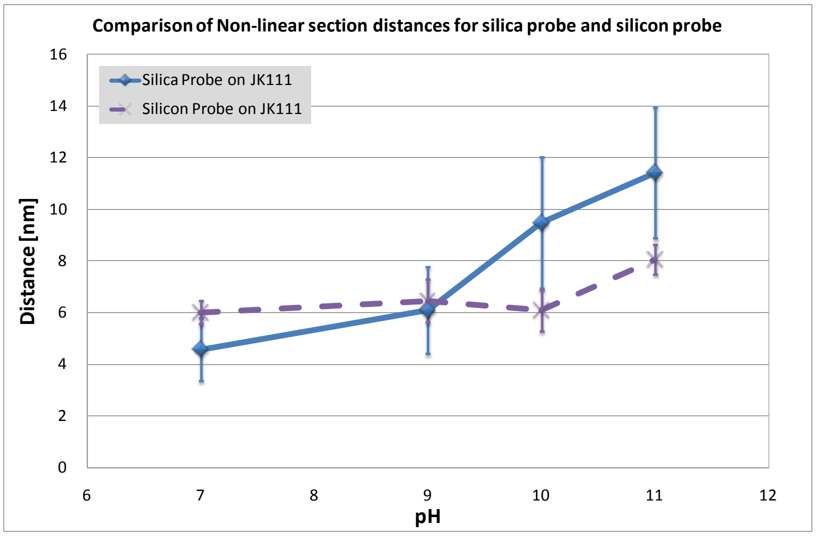

(a)

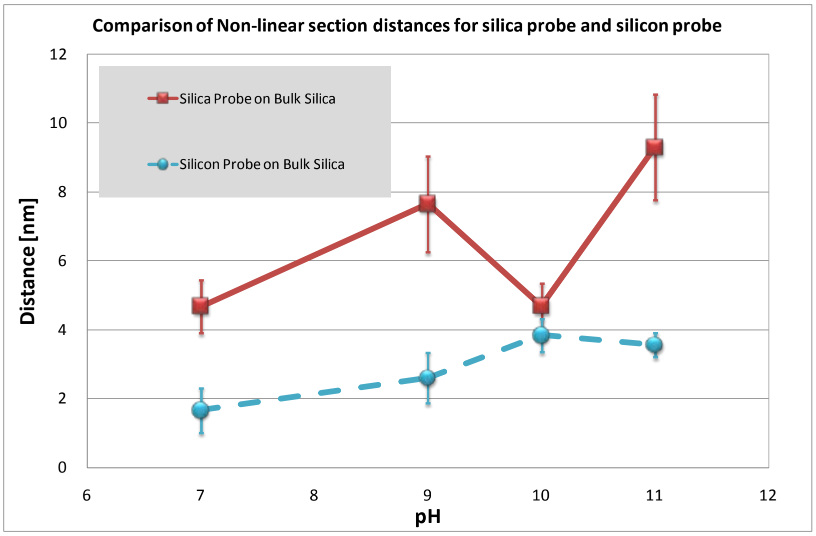

(b)

Figure 3.16: Comparison of the non-linear section distances for (a) the pad and (b) the bulk silica substrate

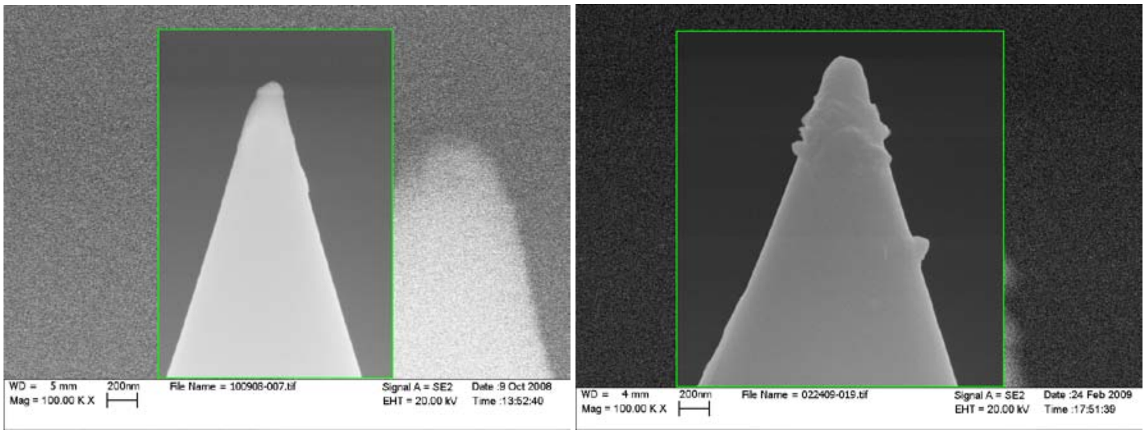

(a) (b)

Figure 3.17: SEM images of the silicon tip (b) before and (b) after indentation experiments.

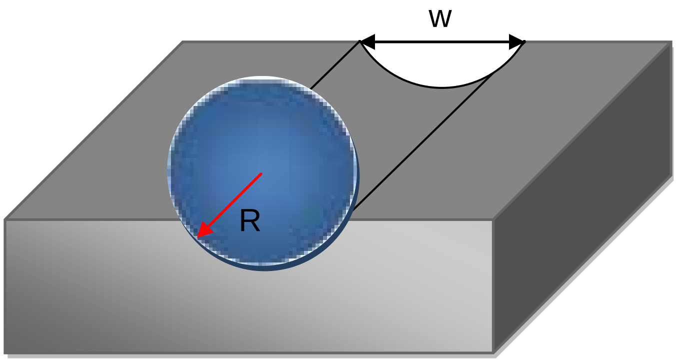

Figure 3.18: Schematic of plowing friction.

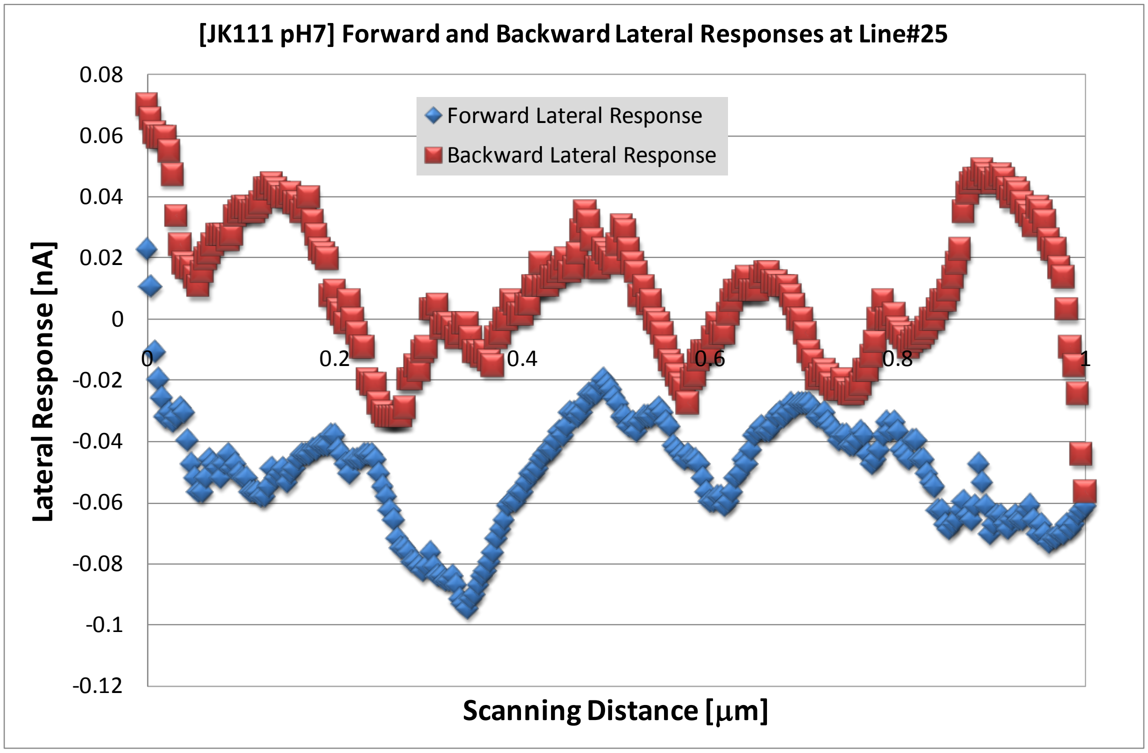

Figure 3.19: Forward and backward lateral responses recorded during scanning.

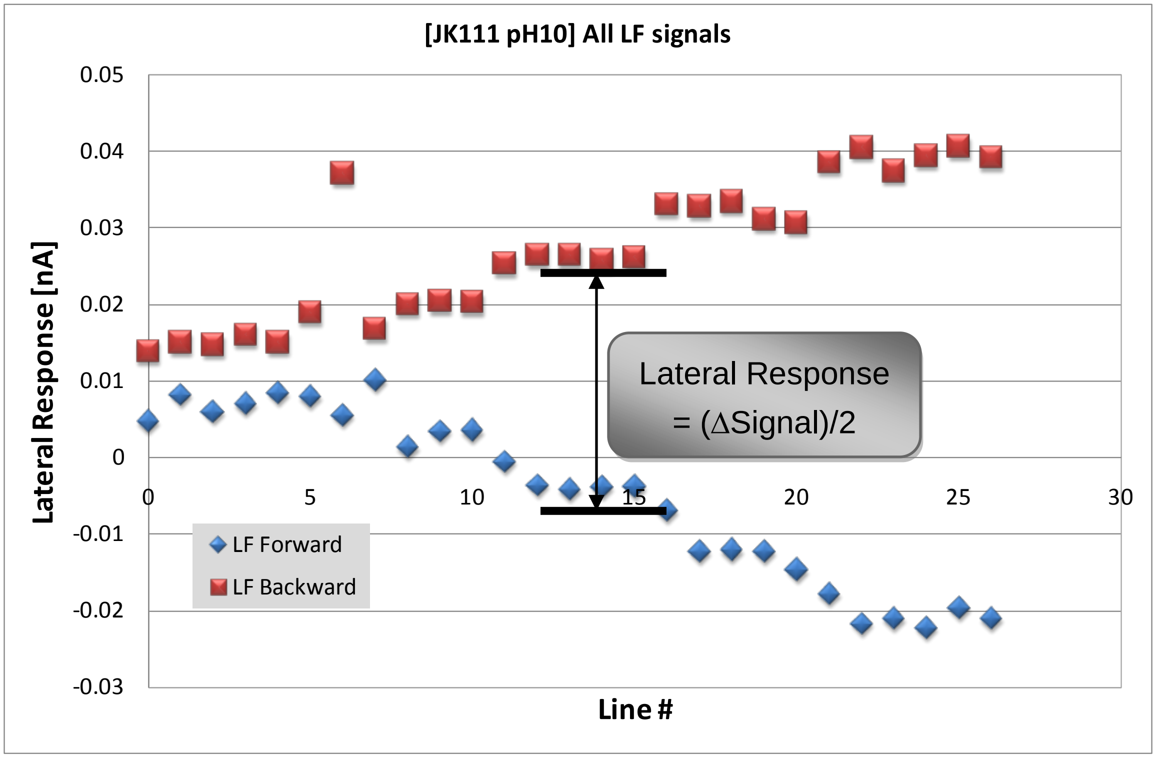

Figure 3.20: Average of each scan line during LFM for 10, 20, 30, 40 and 50 nN.

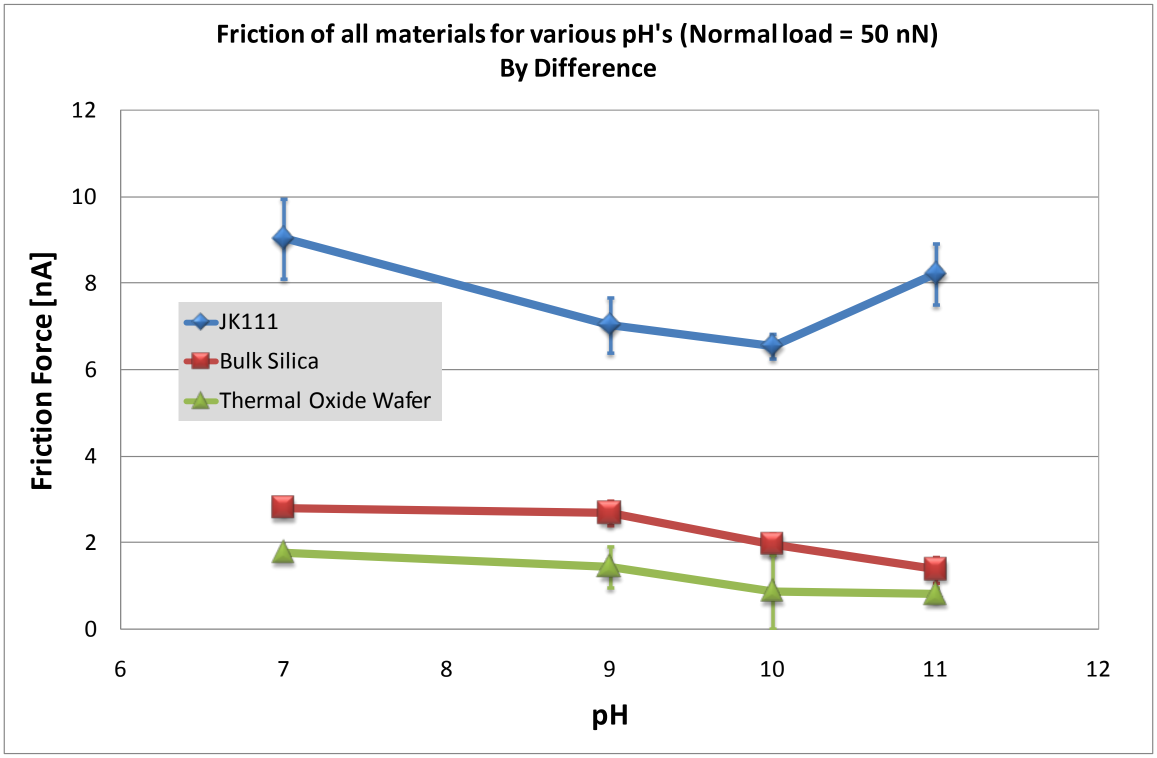

Figure 3.21: Lateral responses of all three samples for various pH environments under 50 nN.

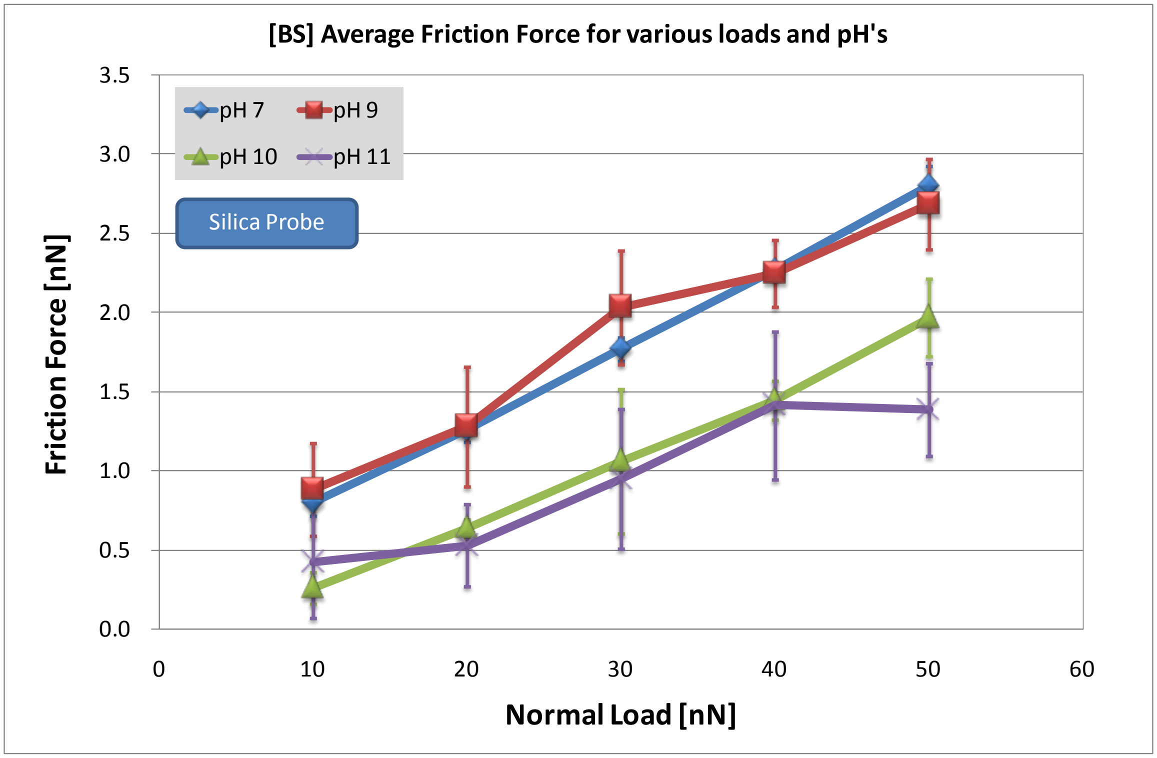

Figure 3.22: Lateral responses of the cantilever with the bulk silica substrate for various loads and pH environments.

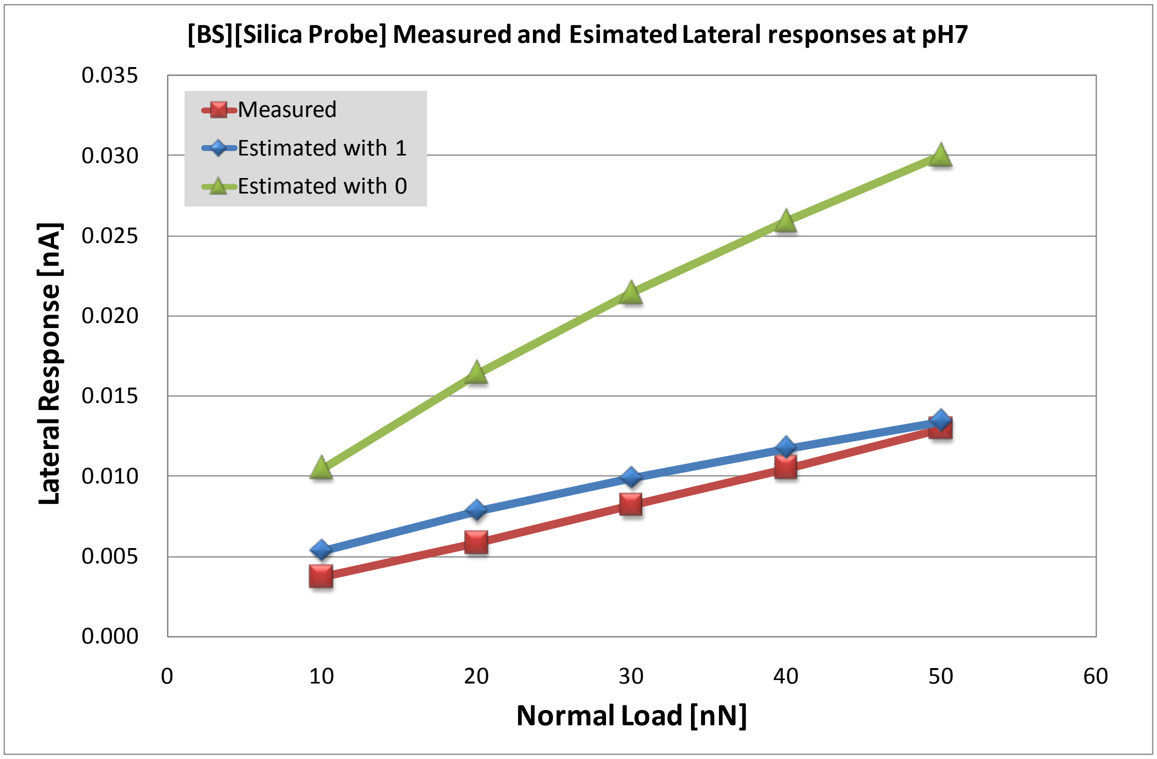

Figure 3.23: Comparison of the measured lateral responses at pH 7 with the estimated lateral responses with α = 1 and α = 0.

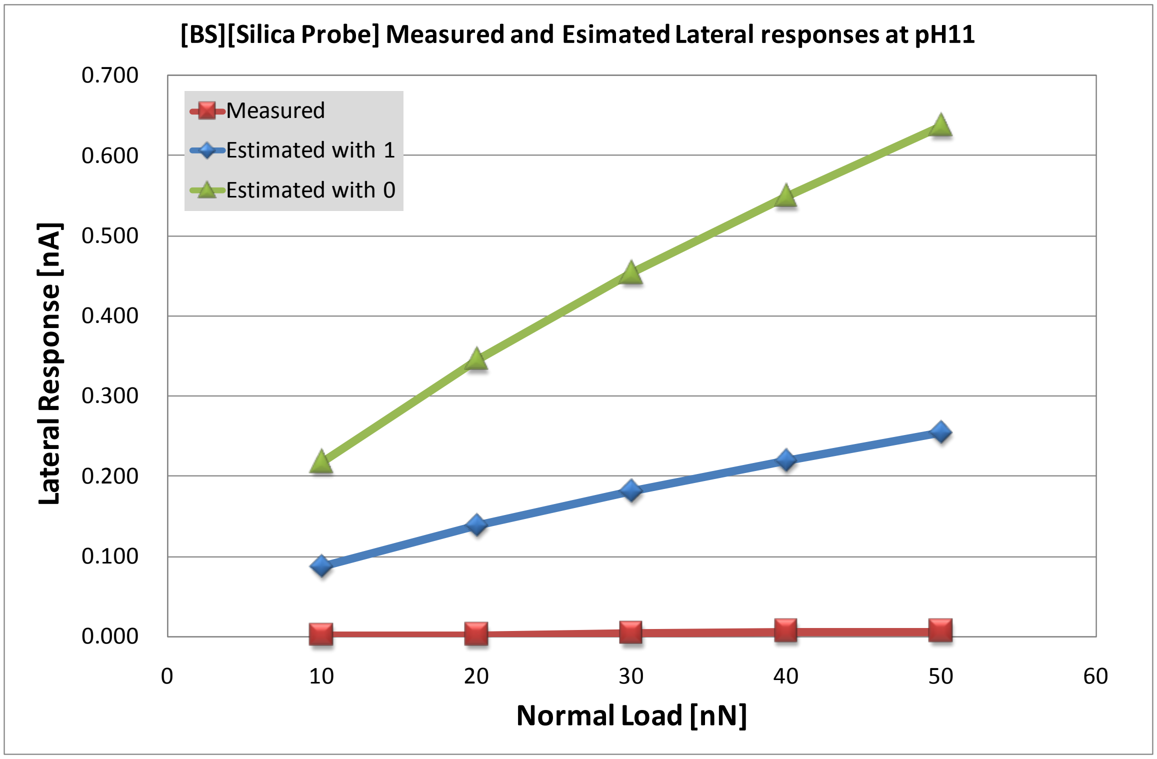

Figure 3.24: Comparison of the measured lateral responses at pH 11 with the estimated lateral responses with $\alpha = 1$ and $\alpha = 0$.

pH	JK111	BS	TGO
7	5.160	0.473	0.009
9	5.908	2.434	0.000
10	5.450	0.550	0.030
11	7.125	1.086	0.088

Table 3.1: Actual surface deformation in nm caused by the silica AFM probe under 50 nN for various pH environments.

Materials	Radius [nm]	Elastic Modulus [GPa]	Poisson's ratio
Silica Probe	51.85	70.0	0.17
Bulk Silica, Thermal Oxide Wafer	Infinity	70.0	0.17
JK111	Infinity	0.50	0.50

Table 3.2: Parameters used to calculate the contact radius.

pH	Actual deformation [nm]	Hertzian Contact Radius [nm]	w/2R
7	5.160	16.357	0.315
9	5.908	17.502	0.338
10	5.450	16.811	0.324
11	7.125	19.220	0.371

Table 3.3: Estimation of 1) contact radii between the silica probe and the pad and 2) w/2R ratios by Hertzian contact based on the actual deformations for 50 nN normal load and different pH environments.

pH	Actual deformation [nm]	Hertzian Contact Radius [nm]	w/2R
7	0.473	4.950	0.095
9	2.434	11.233	0.217
10	0.550	5.340	0.103
11	1.086	7.502	0.145

Table 3.4: Estimation of 1) contact radii between the silica probe and the bulk silica substrate and 2) w/2R ratios by Hertzian contact based on the actual deformations for 50 nN normal load and different pH environments.

pH	JK111	BS	TGO
7	0.181	0.056	0.036
9	0.141	0.054	0.029
10	0.131	0.039	0.018
11	0.165	0.028	0.016

Table 3.5: Friction coefficients of the three samples for pH environments under 50 nN

3.6 References

3.1 J. Hutter and J. Bechhoefer, Calibration of atomic-force microscope tips, Review of Scientific Instruments, 1993, Volume 64, 1868-1873.

3.2 Bozkaya et al. Proceedings of the STLE/ASME International Joint Tribology Conference IJTC2008 (2008) 71122.

3.3 Karuppiah et al., Material Research Society Symposium Proceedings, 2007, Volume 977, 0977-FF04-04-DD05-04

3.4 Johnson, K. L., Kendall, K., and Roberts, A. D., Proc. R. Soc. London A **324,** 301 (1971).

3.5 B.V. Derjaguin, V.M. Muller and Y.P. Toporov, "Effect of Contact Deformations on Adhesion of Particles," *Journal of Colloid and Interface Science* , **53**, 314-326 (1975).

3.6 Robert W. Carpick,1 D. Frank Ogletree, and Miquel Salmeron, "A General Equation for Fitting Contact Area and Friction vs Load Measurements," *Journal of Colloid and Interface Science* **211**, 395-400 (1999).

3.7 Maugis, D., *J. Colloid Interface Sci.* **150,** 243 (1992).

3.8 R.W. Stark, T. Drobek, and W.M. Heckl, Thermomechanical noise of a free v-shaped cantilever for atomic-force microscopy, Ultramicroscopy 86 (2001)

207-215.

3.9 NT-MDT, *Probe-Sample Interaction: Lateral Forces*, Application Notes.

3.10 I. Sokolov, Surf. Sci. 311 (1994) 287

3.11 Maugis, *Contact, Adhesion and Rupture of Elastic Solids*. Springer-Verlag (2000), Berlin.

3.12 Oliver M.R. (ed), 2004. *Chemical mechanical planarization of semiconductor materials*. Springer, NY.

3.13 Jacob Israelachvili, *Intermolecular $ Surface Froces*, Academic Press (1992)

3.14 http://www.erc.arizona.edu/Education/MME%20Course%20Materials/MME%20Modules/Surface%20Prep%20Module/Wet%20Etching%20and%20Cleaning%20-%20Surface.ppt#260

3.15 Murakoshi et al., *Local mechanical properties of mouse outer hair cells: Atomic force microscopic studyAuris*, Nasus Larynx, 2006. **33** 149-157.

3.16 Obeng et al. Obeng, Y., Dogariu, A., and Forsthoefel, K., Mechanical and Chemical Properties of Pads for Use in Chemo-Mechanical Processing (CMP)

3.17 M. Tomozawa, K. Yang, H. Li, and S. P. Muraka, *Mater. Res. Soc. Symp.*

Proc., **337**, 89 (2002).

3.18 M. L. Hammond and S. F. Ravitz, *J. Am. Ceram. Soc.,* **46**, 329 (1963).

3.19 L. Nevot and P. Croce, *Rev. Phys. Appl.,* **15**, 761 (1980).

3.20 Williams, Engineering Triboloy, Cambridge University Press, 2005

3.21 R.W. Carpick and M. Salmeron, "Scratching the surface: Fundamental investigations of tribology with atomic force microscopy," *Chemical Reviews* **97**, 1163-1194 (1997).

Chapter Four

CMP Generated Defects in Cu/low-k Patterned Wafers

4.1 Application of nanoscale single particle analogs

In this section, the goal is to measure the surface and lateral deformation of copper/low-k dielectric patterned wafers by the analog of a single CMP particle and determine the loads that will initiate damage to sample surfaces. This was achieved by the use of Atomic Force Microscopy (AFM) nanoscratching in KOH to mimic the surface damage introduced during CMP, which are generated by agglomeration of CMP abrasive particles, non-uniformities of polishing pad and integration of weak, low-k dielectrics. The damaged surfaces were investigated with AFM and SEM to observe the scratch depth and line bending of patterns, respectively. Critical loads that initiate deformation or line-bending were estimated for each structure and the results can be used as a guide for determining preferred pattern ratios. A contact analysis is applied to understand the generation of stresses which drive the surface damage.

The concept of the CMP particle analog was adopted again to simulate the damage caused by friction on the patterned wafer during CMP. A triangular cantilever with a diamond-coated AFM probe was the analog of a nanoscale individual polishing particle in CMP. The normal spring constants were obtained before their use. The radius of curvature and thickness of the diamond coating of each probe was measured with SEM (See Section 2.3.1). The wafer was composed of a copper interconnect and two silica dielectrics and it had structures with different pattern widths for the copper and dielectric.

4.2 Experimental

4.2.1 AFM Cantilevers

Since friction measurements on a patterned silicon wafer are subject to a high load, it is necessary to have a probe that is highly resistant to wear and a cantilever that is stiff enough to apply large normal and lateral loads for scribing. Au-coated reflective triangular Si cantilevers with a diamond-coated probe tip (DCP20, NT-MDT) were used. Typical dimensions and spring constant range of cantilevers from the manufacturer is presented in Table 4.1. Since the range of the spring constant provided by the manufacturer had a large variation, to know with precision the applied load during experiments, the cantilever spring constants were calibrated prior to performing experiments. In addition, lateral calibration factor was obtained to convert the lateral signals to lateral forces.

4.2.2 Normal Spring Constant Calibration of a Triangular AFM cantilever and Determination of Lateral Calibration Factor

Spring constants of triangular cantilevers are determined by using the thermal tuning methods [3.1]. The method is developed for a rectangular cantilever, thus a correction for triangular cantilever geometry is used

($k_{tri.} = 0.764 k_{rec.}$) determined by Stark et al. [3.8] using FEM. Thus, the normal spring constant ($k_{N,Tri}$) of the triangular can be determined by,

$$k_{N,Tri} = 0.764 \frac{k_B T}{A} \qquad (4.1)$$

where k_B, T and A represent the Boltzmann constant, measured temperature in Kelvin and the area under the power spectrum-frequency curve, respectively. Applied normal loads are calculated by multiplying the spring constant (k) by a distance that is measured from the force-displacement curve for a given photodiode signal change.

The procedure to determine the lateral force calibration factor for a triangular cantilever is similar to the rectangular cantilever case (see section 3.2.1.2). The lateral spring constant (k_L) estimated by geometry [4.1] is sensitive to E^*t^3 where E is the elastic modulus and t is the thickness of the cantilever. Since it is difficult to measure the exact value of the elastic modulus and thickness of the cantilever, the lateral spring constant measured from geometry may deviate from its real value significantly. This can be avoided by determining the value of E^*t^3 numerically after measuring the normal spring constant experimentally and comparing that to the normal spring constant of the triangular cantilever found from geometry [4.2]. The ratio of the lateral and normal spring constant can be obtained by comparing the two calculated values. Since the lateral sensitivity does not depend on geometry, it can be found in the same ways as in the rectangular cantilever case.

4.2.3 Materials – Patterned Wafer

Patterned silicon wafers acquired from an industrial supplier contained a copper serpentine line pattern within a silica dielectric (See Figure 4.1). Samples were diamond-scribed from 300 mm wafers into specimens of 10 mm x 5 mm in size. Copper interconnect and dielectric film patterns had variations in line width and in spacing, ranging from 80 nm to 235 nm and 80 nm to 245 nm, respectively. To assist in normalizing the patterns, a pattern density is defined by the ratio of the dividing a copper interconnect width to the sum of the copper interconnect and dielectric film widths. SEM was used to measure widths of the copper interconnect and dielectric film and the widths and pattern densities are presented in Table 4.2.

In addition, two different dielectric (k_A = 3.05; k_B = 2.50) materials were compared, and taken from separate wafers. Properties of the two dielectrics varied by a factor of 1.08 for the elastic modulus (E_A/E_B) and 0.92 for nanohardness (H_A/H_B). The properties of the two dielectric materials provided in Table 4.3. Porosity differed by a factor of 0.27 a clear indicator of the change in dielectric constant of the film.

4.2.4 AFM Force Lithography

AFM force lithography is a technique used to scan a prescribed region of a sample with a controlled load and geometry. The method can be considered as a “write”-technique and when integrated with fluid reservoirs and heated probes can be used for a variety of applications. By recording the cantilever deflection and torsion signals while scanning, lateral forces and coefficients of friction can be calculated. Friction force (FFM) or lateral force measurements (LFM) are similar techniques which apply normal loads orders of magnitude smaller. Here, samples are mounted in an open wet cell where force lithography is performed on specific line patterns found on the surface with a diamond coated probe tip connected with a high stiffness cantilever. After completing the spring constant measurements and the sample preparation, the sample was mounted in a wet cell and the calibrated cantilever was installed on a glass prism holder. KOH (pH = 9.21) filled the wet cell, completely submerging sample and cantilever. Patterns of interest were identified using an optical microscope attached to the AFM, and series of scans were performed to locate the pattern. After exposure to KOH for one hour, force lithography was used to produce scratches perpendicular to the serpentine line patterns. A wide span of applied normal loads was applied to determine the minimum load to plastically deform the surface and to obtain deformations such as the scratch depth and line bending of patterns as a function of an applied normal load. For all lithography scans, the scratch length was 2 μm and the scribing speed of the AFM probe was 0.3 μm/s. Separation between scratches was 1 μm. Due to potential wear of the diamond coated probes, single cantilever was used for force lithography of two patterns. After completion of the lithography, the sample surfaces were scanned in an intermittent contact mode to observe surface deformations made on the copper interconnects and the dielectric films after scratching. This allows for observations and analysis of the 3-D topography and profiles of the scratches to measure the depth and corresponding pile-up to investigate relationships between the applied loads and scratch depths. In addition, SEM was used to image deformation of copper interconnects and dielectric films due to lateral forces applied during scratching. AFM, though effective in observing changes of topography, was unable to determine deformation of line patterns.

4.3 Results

4.3.1 Measurement of scratch deformation

After performing scratch tests, the used tip was observed again with SEM to observe tip wear. The SEM micrographs of the probe tip presented in Figure 4.2 (a) and (b) show a significant change in the probe tip after scratch testing. Debris from surface machining and wear is formed on the tip ends. Surface topography after scratching was measured with an AFM in intermittent contact mode directly after testing to avoid contamination such as dust. Intermittent contact mode is used so that damage does not occur due to topography scanning with high spring constant cantilever. Figure 4.3 shows (a) an AFM image of the surface topography with deformed structures and (b) the SEM micrograph for the same structure. The dark regions of the serpentine line structure represent dielectric material. The copper lines had an ~ 12 nm height change from the dielectric film. Lines were verified with SEM (Figure 4.3 (b)) and energy dispersive X-ray spectroscopy (EDX) to determine the chemical composition as a function of spectral location. Material removed can be seen in the middle and on the right side. In Figure 4.3 (b), the white and black lines are the copper interconnect and the dielectric film, respectively.

The topography data was analyzed along the scratching direction and perpendicular to the scratches. For the profiles along the scratch directions, deformations of copper interconnects and dielectric films were analyzed simultaneously to measure average scratch depth for a given applied normal load. Surface profiles perpendicular to the scratches on the copper interconnects and dielectric films were measured separately to observe the effect of applied normal loads on the two materials. The same analysis was repeated for structures with different line densities to observe the effect on the deformations.

Figure 4.4 shows the scratch depth measured along scratches made on Structure 1 for applied normal loads from 10 – 19 μN. A reference profile, which is a profile along the intact copper interconnects or dielectric films, was used to measure the height variations of the intact copper interconnects and dielectric films, was 7.59 nm and 5.49 nm, respectively. As expected, the scratch depth increased as the applied normal load increased. This relationship can be considered linear because the depth changes in the first two loads are compatible with the roughness of the intact structure, thus the second data point can be considered that it is not located far from the regression line. By extrapolating the regression line down to the x-axis, a critical load, which is the normal load that initiates the plastic deformation of the surface, was estimated to be 9.62 μN. This estimation is a good indicator of the maximum normal load that should be avoided during a CMP process. The normal pressure for this load is estimated to be 544.64 MPa using Hertzian contact.

It was observed that the deformation of the dielectric film was negligible since the deformation of the film was on a similar magnitude as the roughness measured from the reference profile. However, a noticeable variation of scratch depth was observed on the copper interconnect and this indicates that the dielectric film is less susceptible to lateral load compared to the copper interconnect. The results in Figure 4.5 represent the scratch depth of the copper interconnects and the height of the corresponding pile-up as a function of normal loads. An example of where scratch depth and pileup are located is shown in Figure 4.5. Both scratch depth and pile-up increased with increasing loads. The magnitude of the pile-up height was generally smaller than that of the scratch depth. However, it increases drastically with copper deformation. This indicates that the pile-up may worsen with an increased downforce. Thus, it is crucial to estimate the load for the onset of the plastic deformation of the copper interconnect because the pile-up is observed to be generated after the initiation of the plastic deformation and increases rapidly.

4.3.2 Analysis of Line Pattern Effect on Scratch Deformation

The effect of the pattern line density was observed by comparing the scratch deformation results. Structure 2 (I = 0.467) and Structure 3 (I = 0.751) were chosen so that the effect of a wider copper interconnect line with respect to the dielectric width could be observed. In Figure 4.6, the scratch depths of both structures are presented as a function of applied normal load. The critical loads (i.e. the loads to initiate a permanent deformation) for Structures 2 and 3 were estimated to be 8.84 μN and 8.69 μN, respectively, implying that both structures began to incur permanent deformation at a similar normal load. In addition, the red arrows drawn in Figure 4.6 indicate that the structure 2 requires a higher normal load to obtain the same deformation as structure 3. Alternatively, this may be quantified by the slopes, m, of linear regression lines (m = 0.0038, 0.0074; structure2, 3, respectively. The results indicate a smaller slope for the lower density structure 2 implying that a lower density will decrease the scratch deformation. This may be explained by the confinement of the copper line within the lower-k dielectric film. Since copper has a lower hardness than the dielectric, the stress necessary to deform the copper is achieved at a lower contact pressure. A wider copper line (as in structure 3) will have a larger span which unconstrained by the dielectric film, allowing for an increase in surface deformation.

4.3.3 Analysis of Dielectric Stiffness Effect on Scratch Deformation

Two structures which had a similar line density but were composed of different dielectric materials were tested with the AFM nanoscratch technique. The relative elastic modus and nanohardness of the two dielectric materials can be seen in Table 3. The scratch deformation response to normal loads is presented in Figure 4.7. The material properties of film B were approximately 70 % of those of film A due to porosity introduced during processing. Structure 2 and 4 had a similar line density, though the responses to lateral forces were markedly different. Structure 4 with weaker dielectric film B was far more susceptible to plastic deformation than Structure 2 with dielectric film A. The critical load to deform Structure 4 was estimated to be 1.04 μN, compared with 8.834 μN for Structure 2. A regression analysis of the data shows a larger slope for dielectric film B than that for dielectric film A, indicating that Structure 4 is more susceptible to deformation. The advantage of using the dielectric film B can only be maintained by controlling the contact pressure more carefully. The results are expected since the lower stiffness and hardness of film B provides less constraint to the contact stresses during scratching.

4.3.4 Line bending of Patterned wafers

An illustration of how to measure line bending of a pattern is presented in Figure 4.8. It was assumed that a copper interconnect and a dielectric film bent the same amount. The distance between the intact and the bent copper interconnect is measured to determines the displacement of the copper pattern due to bending.

4.3.5 Analysis of Line Pattern Effect on Line Bending

Bending of the copper and dielectric line patterns for Structures 1 and 2, which had different line densities (I = 0.623, I = 0.476; for structure 1, 2, respectively), were obtained after scratches were performed on both structures. The dielectric film material was the same for both tested patterns. Measurement techniques were followed as described in the experiment section and utilized scanning electron microscopy and digital imaging software. Structure 1 was observed to exhibit more resistance to bending due to a lateral applied force (see Figure 4.9). The critical normal loads where initial was observed for Structures 1 and 2 were estimated to be 5.27 μN and 10.6 μN, respectively. A large slope of the regression line for Structure 1 indicates that there requires less load to achieve the same amount of line bending compared to Structure 2. The thinner dielectric film width between copper lines increased the amount of observed line bending. The decreased constraint of the dielectric thickness between copper lines of the same width allowed lateral forces translated into shear stresses to shift the pattern. This can be considered as a two-dimensional element of material, where the free surface contains a shear traction and the lower surface is assumed constrained to the substrate. The extent of the linear deformation (bending) has not been observed, though it is postulated that the materials remain adhered to the substrate, as long as applied loads were not high enough to remove and wear material. Since the surface displacements observed are on the order of 10 nm, and the vertical film thickness is on the order of microns, the contact stress field is a local phenomenon. For thinner film thicknesses or different size indenter tips, results are hypothesized to be affected by these size effects, due to the contact stress field in the subsurface being related to the film thickness through a substrate effect and the indenter size by a contact pressure similarity.

4.3.6 Analysis of Dielectric Stiffness Effect on Lind Bending

The effect of film materials on line bending was observed in Structures 2 and 4, which had a similar pattern density but different dielectric film materials. Figure 4.10 shows the observation that a difference in the dielectric film material properties has a significant effect on the amount of line bending. Dielectric film A showed over two times more resistance to line bending. This result is partly expected because the width of the dielectric film was observed to be critical in the previous analysis. This can be considered an element of material which is effectively thinner due to the property decrease. An interaction between line structures surely is an important factor as observed, though the property effect seems to play a greater role in the mechanism of line bending than the line density.

4.4 Discussion

4.4.1 Scratch Mechanics

The deformation and stresses in contact between the particle analog (probe tip) and the substrate is described in Figure 4.11. Surface deformation is governed by the mechanical properties of the materials and the boundary conditions due to the free surface, substrate, and line interfaces. Considering a half-space of a homogeneous material the contact stresses on the surface and within the sub-surface are calculated following Hamilton and Goodman [4.3, 4.4] for a three-dimensional sliding contact (with circular contact area of radius *a*), where the boundary conditions inside the contact circle are based on the Hertzian pressure relation,

$$\sigma_z = -\frac{3P}{2\pi a^3}\sqrt{a^2 - r^2} \qquad (4.2)$$

and the shear traction relation,

$$\tau_{zx} = -\frac{3F}{2\pi a^3}\sqrt{a^2 - r^2} \qquad (4.3)$$

with the condition that $F = \mu P$, where F is the friction force, μ is the friction coefficient and, and P is the applied normal load. The combined stresses based on superposition of the normal and shear traction distributions, at the surface (z = 0) and in the contact area (r < a) are given by:

$$\sigma_x = \frac{3P}{2\pi a^3}\left[\frac{1}{r^2}\left\{\frac{y^2-x^2}{r^2}\left[\frac{1-2\nu}{3}\left\{(a^2-r^2)^{3/2}-a^3\right\}\right]-(x^2+2\nu y^2)(a^2-r^2)^{1/2}\right\}\right]+\frac{3F}{2\pi a^3}\left[-\frac{\pi x}{2}\left(\frac{\nu}{4}+1\right)\right] \quad (4.4)$$

$$\sigma_y = \frac{3P}{2\pi a^3}\left[\frac{1}{r^2}\left\{\frac{x^2-y^2}{r^2}\left[\frac{1-2\nu}{3}\left\{(a^2-r^2)^{3/2}-a^3\right\}\right]-(y^2+2\nu x^2)(a^2-r^2)^{1/2}\right\}\right]+\frac{3F}{2\pi a^3}\left[-\frac{3\pi\nu x}{8}\right] \quad (4.5)$$

$$\tau_{xy} = \frac{3P}{2\pi a^3}\left[\frac{xy(1-2\nu)}{r^4}\left\{-(a^2-r^2)^{1/2}r^2-\frac{2}{3}(a^2-r^2)^{3/2}+\frac{2}{3}a^3\right\}\right]+\frac{3F}{2\pi a^3}\left[\frac{\pi y}{4}\left(\frac{\nu}{2}-1\right)\right] \quad (4.6)$$

$$\tau_{zy} = 0 \quad (4.7)$$

The maximum stress for friction coefficients greater than 0.3 (for ν = 0.3) will reside at the surface. Since a large deformation (plowing) is present, assumption of at least μ = 0.3 is assumed between the diamond probe tip and the surface materials (copper and a low-k dielectric) in the analysis.

Contact stresses normal to the surface are calculated for 8 μN normal load from equation (1), where the maximum contact stress for the copper and dielectrics (A and B) are located at the center of contact and estimated to be 4.199, 0.926 and 0.745 GPa. The contact area, *a*, was calculated by Hertzian contact using the values given in Table 4.4. For the diamond-coated AFM probe, the radius of curvature was assumed to be 500 nm because of the tip wear during experiments. Compared with the hardness of copper, ~1 GPa, the material is expected to incur permanent deformation when a yield criteria of the material is exceeded. To realize the effect of the normal and tangential tractions together, it is more relevant to represent the stress in a combined state with the von Mises yield parameter:

$$J_2 = \frac{1}{6}\left[(\sigma_x-\sigma_y)^2+(\sigma_y-\sigma_z)^2+(\sigma_z-\sigma_x)^2\right] + \tau_{xy}^2 + \tau_{zx}^2 + \tau_{zy}^2 \qquad (4.8)$$

On the surface centerline (*z* = 0, *y* = 0), $\sqrt{J_2}/p_{max}$ is plotted in Figure 4.12 using ν= 0.3 and μ=0.3. It is known that as the COF increases, surface stresses are more dominant than sub-surface stresses, and that significant yielding will occur at the surface. The center of the trailing edge of the probe represents the critical stress location as indicated in Figure 4.12. When the COF is less than 0.3, the material is predicted to yield predominantly in the sub-surface. When the values of *J₂* are greater than or equal to a critical stress value, yielding would be expected. This is given by,

$$J_2 \geq \frac{Y^2}{3} \qquad (4.9)$$

For $\frac{\sqrt{J_2}}{p_{mx}} = 0.378$ (assuming μ = 0.3), then $p_{mx} = 2.65\sqrt{J_2}$. Taking $\sqrt{J_2} = \frac{Y}{\sqrt{3}}$ where *Y* is the yield strength in simple tension, for surface yield $p_{mx} = \frac{2.65}{\sqrt{3}}Y$. Considering the mean pressure of the normal contact, where $\bar{p} = \frac{2}{3}p_{mx}$, then $\bar{p} = \frac{2}{3}\frac{2.65}{\sqrt{3}}Y$. Assuming the Meyer's hardness relationship for the materials, $Y \approx$

$\frac{H}{3}$, then the mean pressure is given as $\bar{p} = \frac{2}{3}\frac{2.65}{3\sqrt{3}}H$. The critical load ($P_{cr}$) to initiate yielding is determined using the Hertzian relationship between load, geometry, material properties, and the contact area [4.5],

$$P_{cr} = \pi\left(\frac{3PR}{4E^*}\right)^{2/3}\frac{2}{3}\frac{2.65}{\sqrt{3}}H \tag{4.10}$$

The critical load can be re-written as.

$$P_{cr} = \frac{9R^2}{16E^{*2}}\left(\frac{\pi*2*2.65}{9\sqrt{3}}H\right)^3 \tag{4.11}$$

For the copper with *E* = 110 GPa and *H* = ~1 PGa, the load was only 14.3 nN. For low-k dielectrics (A and B), with *E* = 8 – 11 GPa and *H* = 1 – 2 GPa, as measured from nanoindentation, the range of load is *P* = 6.587 to 12.214 μN. It is clear that since the Cu lines have a modulus an order of magnitude greater and a similar hardness (~1 GPa), then the load necessary to yield the Cu is much lower. This lead to the change in normal surface deformation observed in the post-scratch scans (see Figure 4.8). As applied normal load was increased, the deformation difference became even more significant. It has to be noted that the critical load for the copper was too low if the copper film is considered only. According to the surface deformation result, the critical load of the copper film initiated at 1.1 μN and 8.8 μN when it was combined with the low-k dielectrics A and B, respectively. If it is assumed that the Cu/low-k film is an effective material with E^*_{eff}, the values were estimated to be 12.48 GPa and 44.13 GPa. For the normal load of 1.1 μN, the contact depth was estimated to be 3.463 nm. The deformation is less than ten percent of the film thickness, so there is no substrate effect on the deformation. Based on the effective moduli calculated above, values of normal load to yield the materials as a function of friction coefficient are found in Table 4.5. The critical load decreased with the increase of friction coefficient showing smaller load is required with a large friction coefficient. The results can be compared with those of Saka et al. [4.6], which performed microscratches on copper and low-k dielectric blanket coatings using a plowing scratch model. Contact stresses of their work were found to be ~ 700 MPa for the scratches. For actual CMP single abrasive particles, if 500nN load is assumed on a particle, then mean pressures are expected to be ~1.5 GPa and larger.

4.4.2 Surface Deformations

The surface deformation results of the same ILD with a different density (section 4.3.2) showed that a larger load was required to obtain the same amount of surface deformation for the structure with lower line density (Structure 2). If the two structures have a different effective modulus but a similar hardness, the deformation depths (h) of the two structures can be expressed with the slopes of Structure 2 and 3 (m_2 and m_3), respectively, as following:

$$h = m_2 P_2 = m_3 P_3 \qquad (4.12)$$

where P_2 and P_3 are the loads to deform the two surfaces by the same amount. Since both structures have a similar hardness, the relation between the load and the effective modulus can be expressed as

$$\frac{E^*_{eff,3}}{E^*_{eff,2}} = \sqrt{\frac{m_3}{m_2}} \qquad (4.13)$$

where $E^*_{eff,2}$ and $E^*_{eff,3}$ are the effective moduli of Structure 2 and 3, respectively. When the values of the two slopes were substituted, the ratio was 1.40 suggesting that the effective modulus of Structure 3 was 1.40 times larger due to the difference in the width of the dielectric film. The increase of ILD in the film reduces the effective modulus which leads to higher loads necessary to deform the surface. A similar value of ratio was observed when the pattern densities of the two structures (I_3/I_2 = 0.751/0.476 = 1.58).

When the structures with similar line densities but a different dielectric materials (A and B) (section 4.3.3) were compared, it was observed that the critical load for the structure with stiffer dielectric material (A) was 8 times larger.

Assuming that both structures have a similar effective modulus, the critical load is governed by the hardness. The ratio of the two critical loads can be express with hardness as

$$\frac{P_{crit,A}}{P_{crit,B}} = \left(\frac{H_A}{H_B}\right)^3 \qquad (4.14)$$

where $P_{crit,A}$ and $P_{crit,B}$ are the critical loads and H_A and H_B are the hardness of for the structures with the dielectric film A and B. Since the ratio of the two hardness values are approximately 2, the critical load ratio calculated from Equation (13) is close to the observed ratio (~8) of the critical loads for the two structures.

4.4.3 Lateral Deformations

Lateral surface deformations as seen in Figure 4.8 are observed to have a semi-circular shape with maximum lateral deformation occurring along the centerline of the scratch. This follows the contact stress analysis and the assumption that material will yield at a critical stress, which predicts the highest stress occurs at the center region of the contact. It is also observed that there is no separation between the copper and low-k dielectric line structures, until significant plastic deformation and delamination occur. Even in this case, there is evidence from SEM analysis that material removal occurs as a single ‘chip’ (see Figure 4.8), with intact copper and low-k regions. This result indicates a strong bond between the materials and the adhesion of the films to the underlying substrate. From the analysis one can predict the critical stresses necessary for significant line deformation, which is the tensile stress at the trailing edge of the contact. For the observed experimental cases, the value was estimated to be 0.326 GPa using equation (4.4) with $y=0$, $x=-a$. This stress is a major contribution to the lateral surface deformations present on the sample. The lateral deformation follows the same response to loading as described in sec. 4.1. The contact stresses will generate a maximum stress state (J_2) in the material which can lead to yielding based on a specified criterion. Though for the lateral deformations, surface driven yield is the dominant mechanism to create the yielding of the Cu and low-k interfaces. The lateral deformation is more affected by the line spacing and widths than the normal deformation and is due to the fact that deformations at the interface are being measured. As the probe traverses one domain to the next, the stress field will interact with the domain interface. The problem of a normal shear traction boundary condition at a bi-material interface has been studied by Bogy [4.7 – 4.8]. When approaching a stiffer material domain in a bi-material, the interface will deform less. The mismatch between the two material stiffness will govern the surface deformation of the interface. As the domain widths are made finite, the effect of the Cu stiffness lowering the load to yield the surface will become more pronounced with a higher Cu line density, which was observed experimentally. An increase of the dielectric spacing (i.e. a decrease in Cu density) will lead to less lateral surface deformation and bending of the domain boundary.

The lateral surface deformation is more intrinsically associated with the stiffness of the Cu/low-k interface than the Cu normal deformation, and therefore the effects of the low-k material will be more pronounced. For results of structures with the different ILD material but the similar line density (section 4.3.6), the load necessary for lateral deformation was different by 2 times. The ratio of the critical loads can be written as

$$\frac{P_{cr,A}}{P_{cr,B}} = \frac{\left(H_A / H_B\right)^3}{\left(E_A / E_B\right)^2} \quad (4.15)$$

Substitution of the values gives 1.9 for the ratio, which as very close to the ratio based on the experiment (1.8).

For the results of the same ILD with differing line density (section 4.3.4), the low-k region width corresponds to the changes in the slope measured from the depth-load plot. The width ratio of the dielectric material A and B (1.71) was similar to the square root of the slope ratio (1.69).

4.4.4 Environmental Effects on Contact Conditions

All tests reported were carried out as explained in a KOH solution with pH = 9. The value was chosen to simulate to a reasonable degree the contact conditions observed during industrial CMP processing. The effect of chemical solution and the aqueous environment was observed to alter results for either prolonged exposure or lack of solution in the contact space. When patterned samples were exposed to KOH solutions for over 1 hour, low contact force (order of nN) AFM topography imaging was observed to deform and cause a material removal process on the surface. This is believed to be due to a significant chemical softening of the materials, which lead to material removal even at low contact pressures. This was also observed with SEM, showing distinct wear grooves and material smearing on the surface in the AFM scanning directions. When diamond coated AFM probes were used for AFM-based scratch tests in a dry environment, significant probe tip wear was observed. This was due to the lack of an aqueous environment between the particle analog and the substrate at the applied scratch loads. The probe wear was detrimental to accurate contact analysis, since the varying tip shape and dimensions would alter the contact conditions. It was clear that performing tests in an aqueous environment were important for adequate understanding of the lateral and normal deformations reported.

4.5 Conclusion

Surface deformation during a CMP process was simulated by utilizing a diamond-coated AFM probe as an analog of a nanoscale individual abrasive particle in CMP and performing AFM force lithography on various structures on a patterned wafer under KOH environment. The analysis of the modified structures by lateral force was investigated in two categories: scratch depth of copper interconnects and line bending of patterned structures. Profile of scratches on both materials showed that the deformation of the dielectric film was negligible compared to that of the copper interconnects. As expected, both scratch depth and pile-up increased as higher normal loads were applied. It is worth noting that the pile-up around the copper interconnects was not significant for small loads but its magnitude increased significantly as more copper was removed. In addition, weaker dielectric film was far more susceptible to plastic deformation. Thus, it is crucial to estimate the load for the onset of the plastic deformation of copper interconnects. When structures with different structure densities were compared, the structure with lower density was preferred to lower a chance of damaging the surface. For bending of pattern, it was found that the structure with larger dielectric film width and with stiffer dielectric material was more resistant to bending. The extent of the lateral deformations in unknown at this point, though due to the small surface deformations during scratching, the profile change is believed to be occurring at the near surface

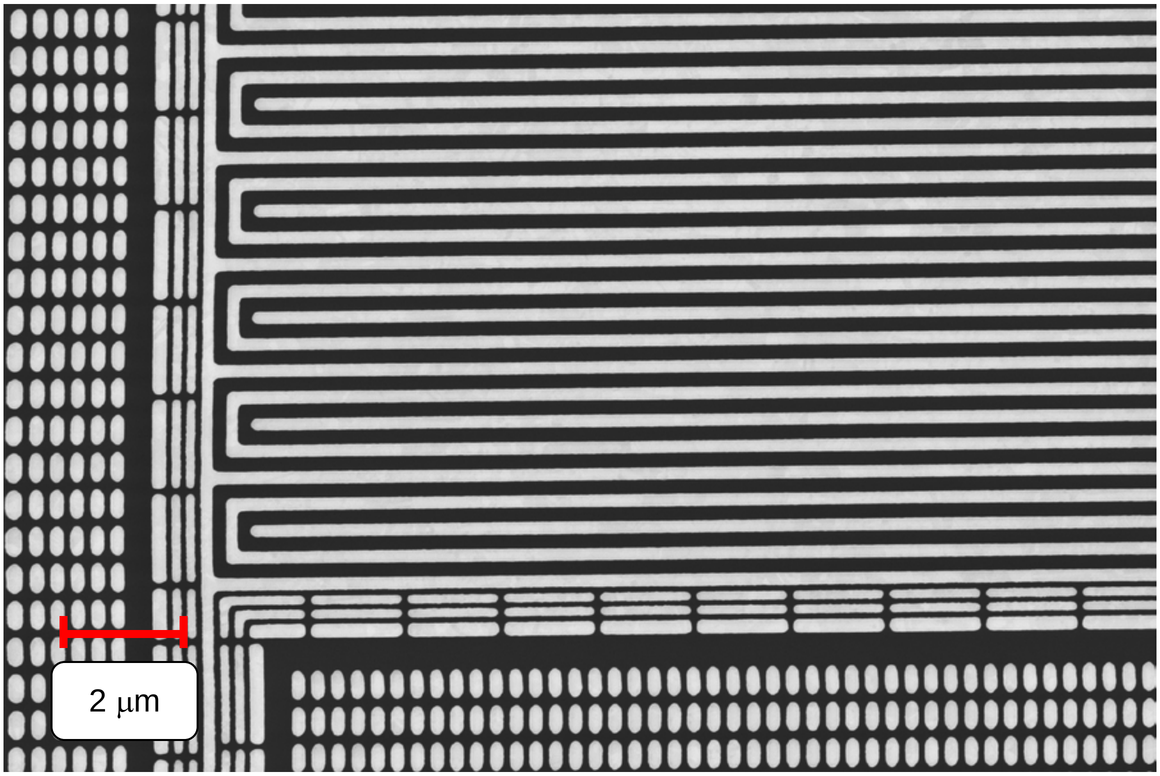

Figure 4.1: Patterned silicon wafers containing a copper serpentine line pattern within a silica dielectric

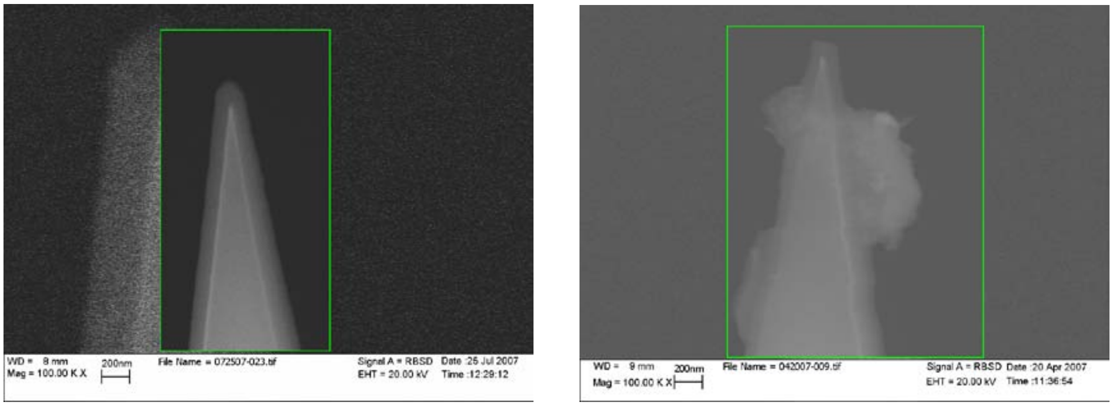

(a) (b)

Figure 4.2: SEM micrographs of the diamond coated probe (a) before and (b) after scratching testing. A significant change in the probe tip after scratch testing is shown forming debris from surface machining and wear on the tip ends.

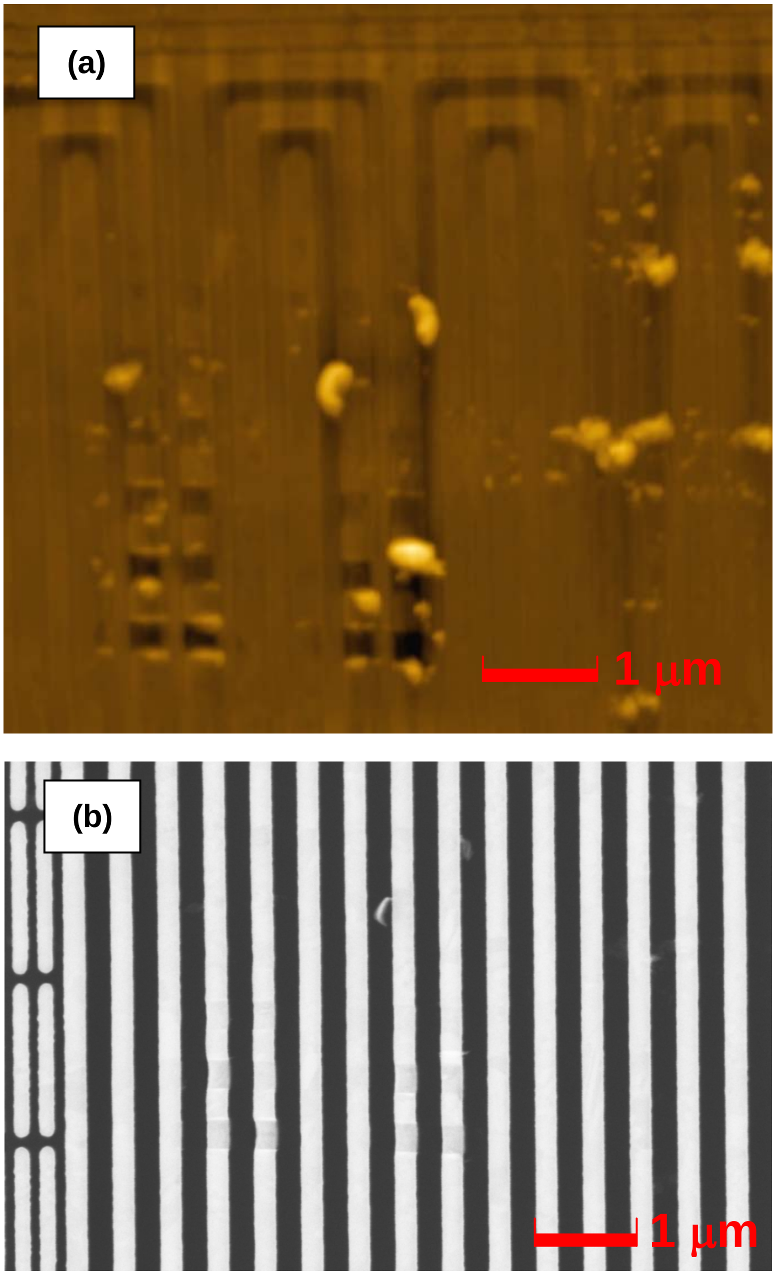

Figure 4.3: (a) AFM topography image of the scratched line structure. Peak to valley height of image is 200 nm. (b) SEM micrograph of the same structure.

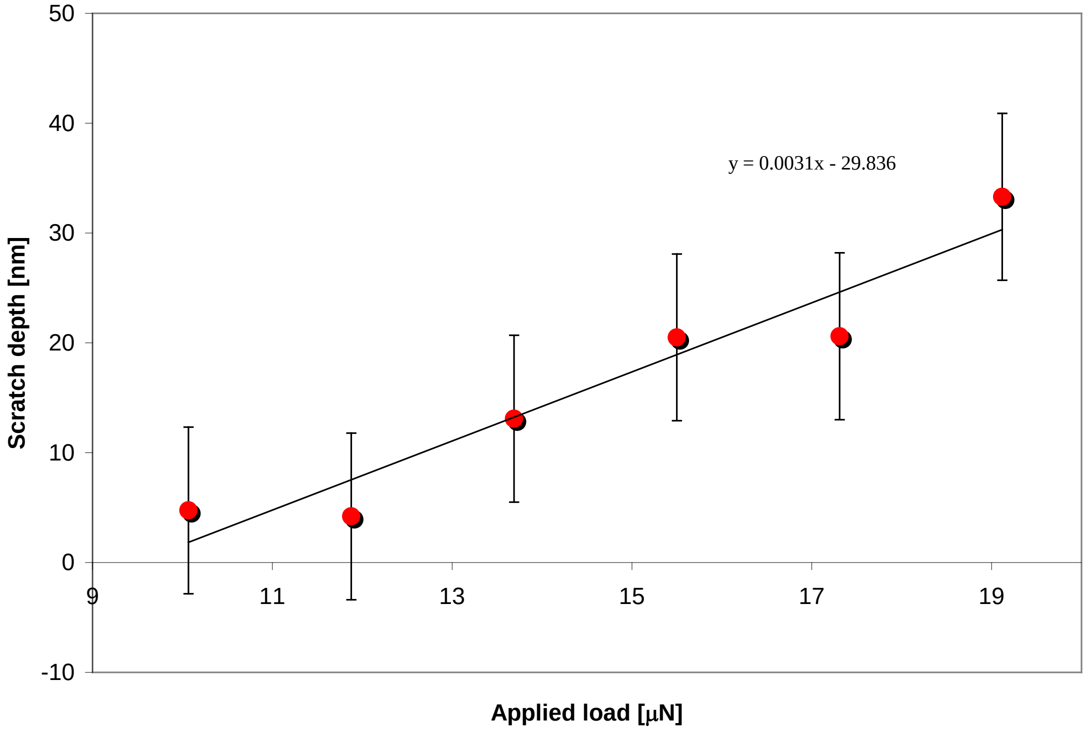

Figure 4.4: Scratch depths as a function of applied loads.

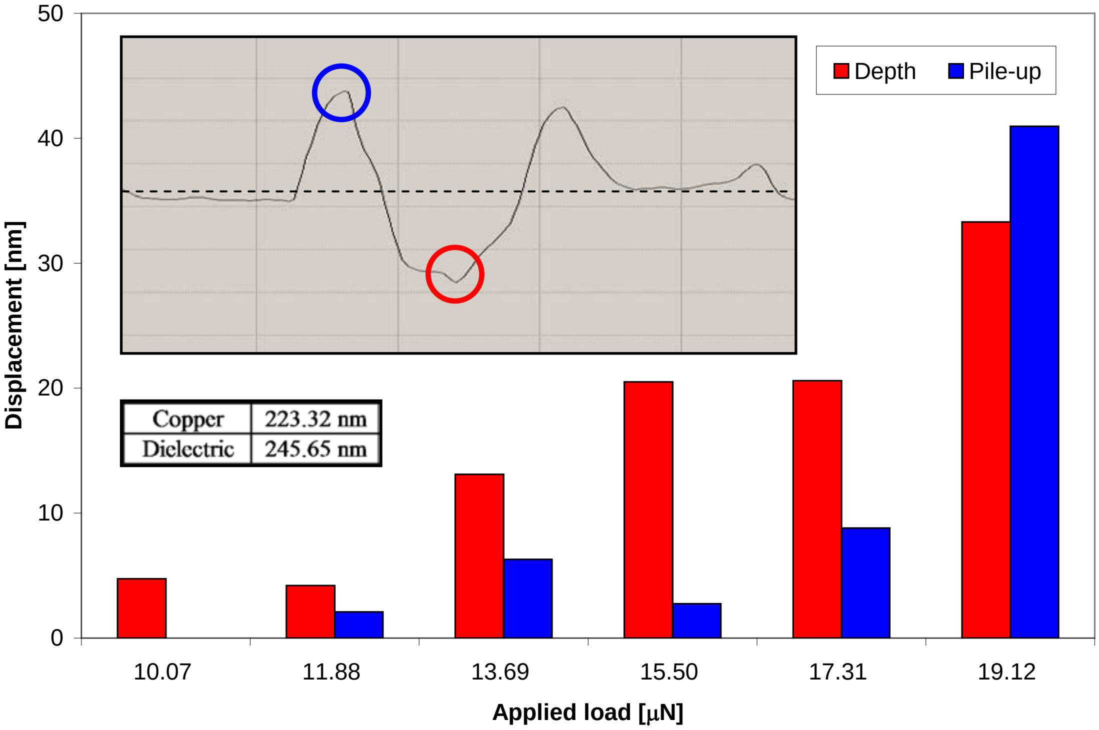

Figure 4.5: Scratch depth and pile-up of copper interconnects with increasing normal loads.

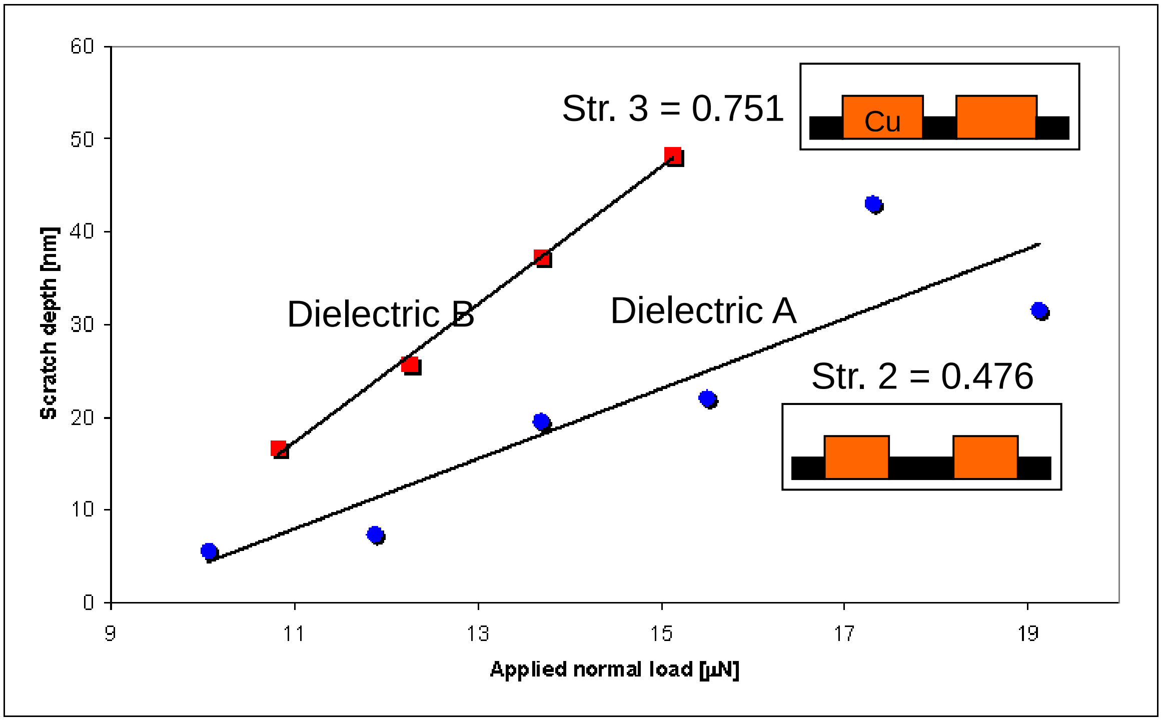

Figure 4.6: Scratch depth as a function of a normal load for the structure with different structure densities.

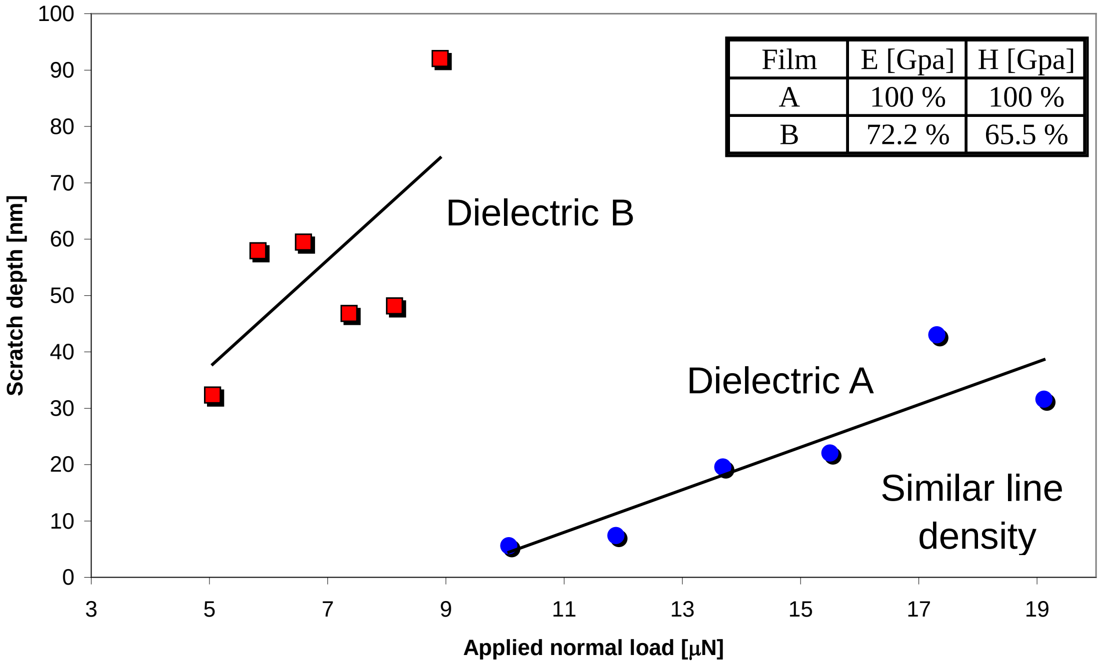

Film	E [Gpa]	H [Gpa]
A	100 %	100 %
B	72.2 %	65.5 %

Figure 4.7: Scratch depth as a function of a normal load with different material properties

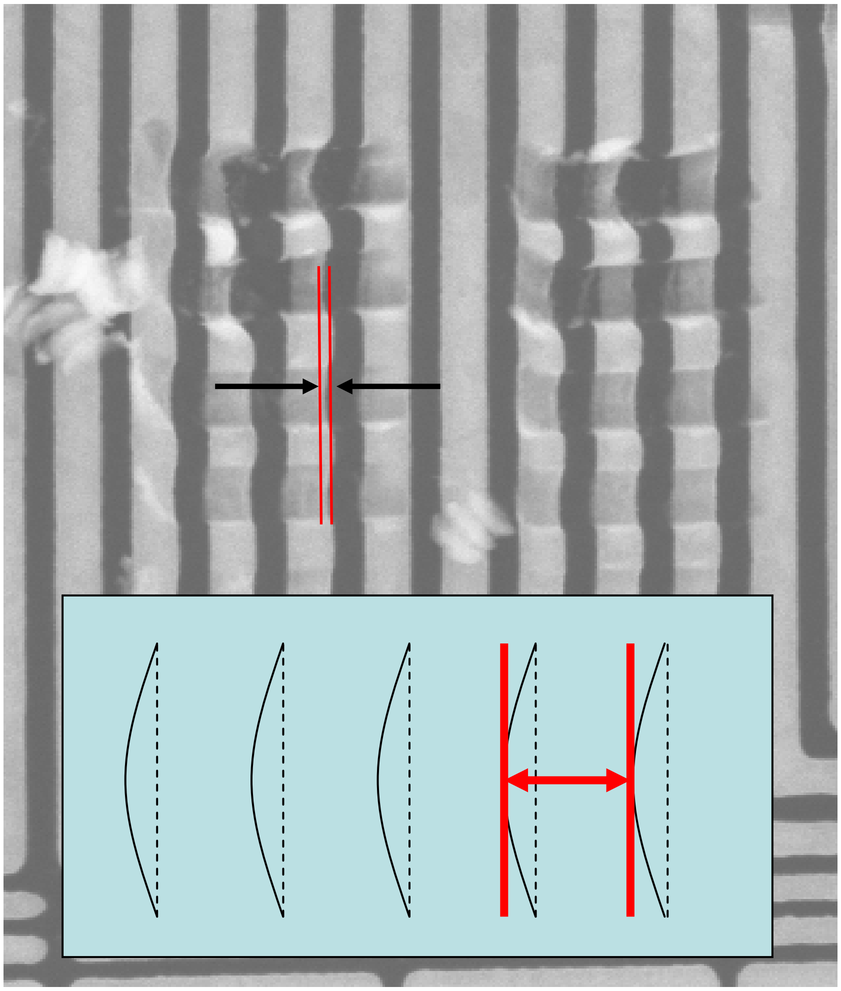

Figure 4.8: Illustration of measurement of line bending with SEM.

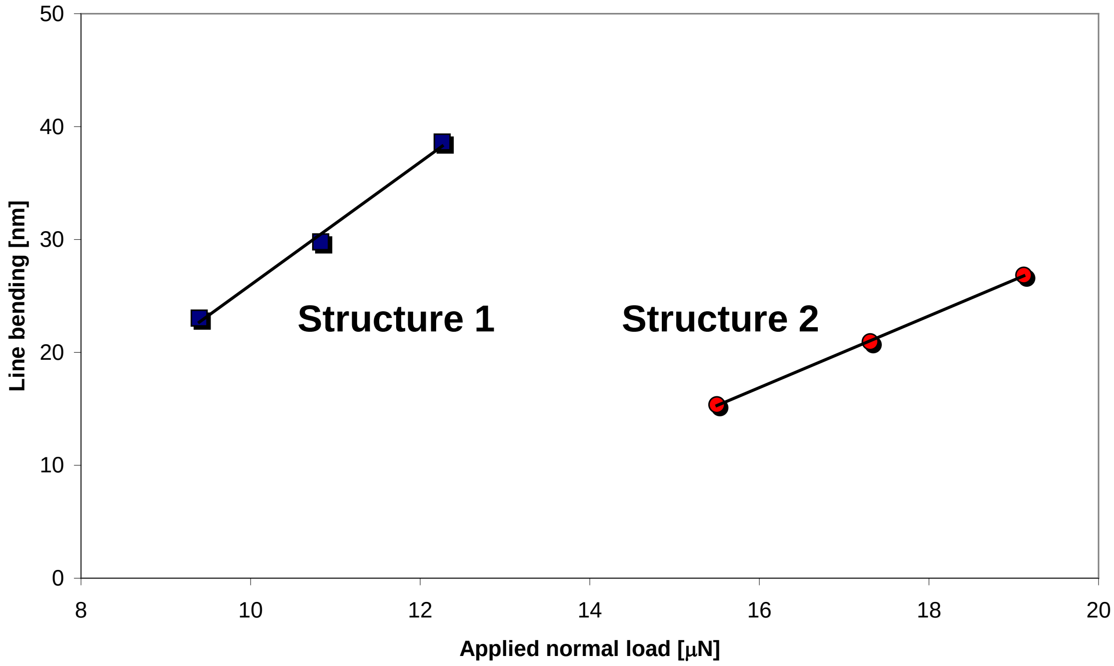

Figure 4.9: Line bending for two structures with different dielectric widths

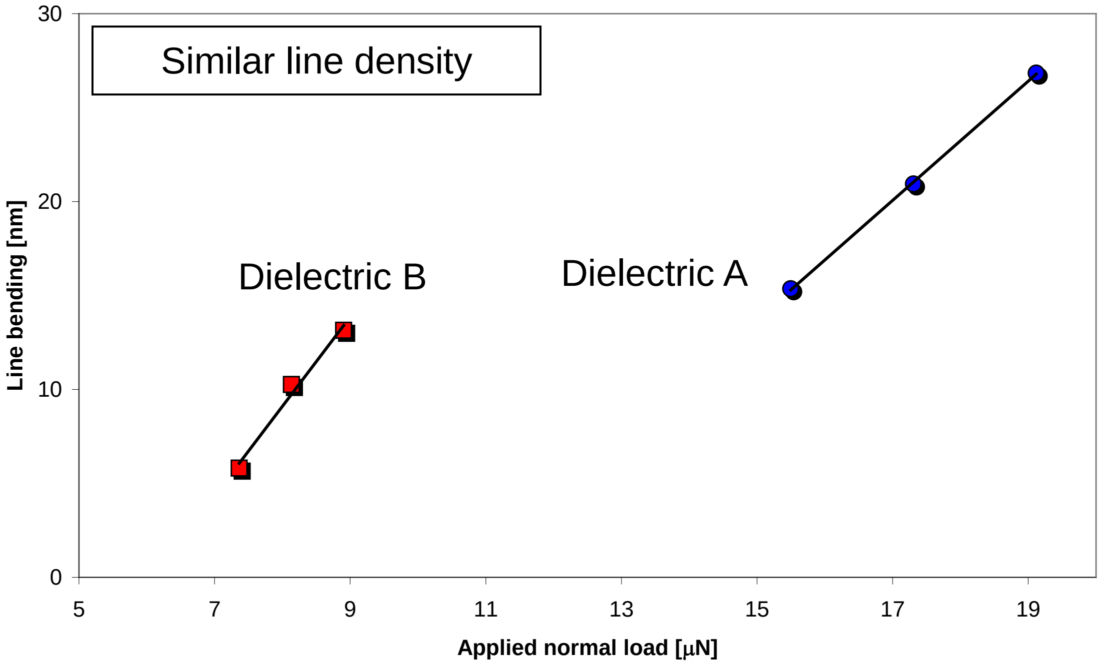

Figure 4.10: Effect of film materials on line bending of the pattern

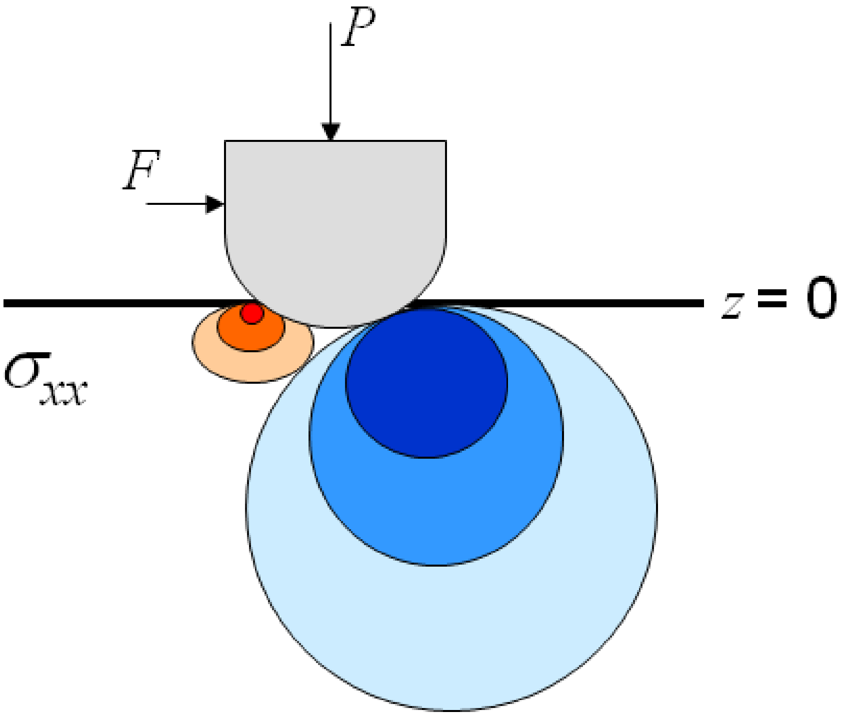

Figure 4.11: Description of the contact stress field (σ_{xx}) between the particle analog and the substrates during sliding contact; red contours represent tensile stresses and blue contours represent compressive stresses.

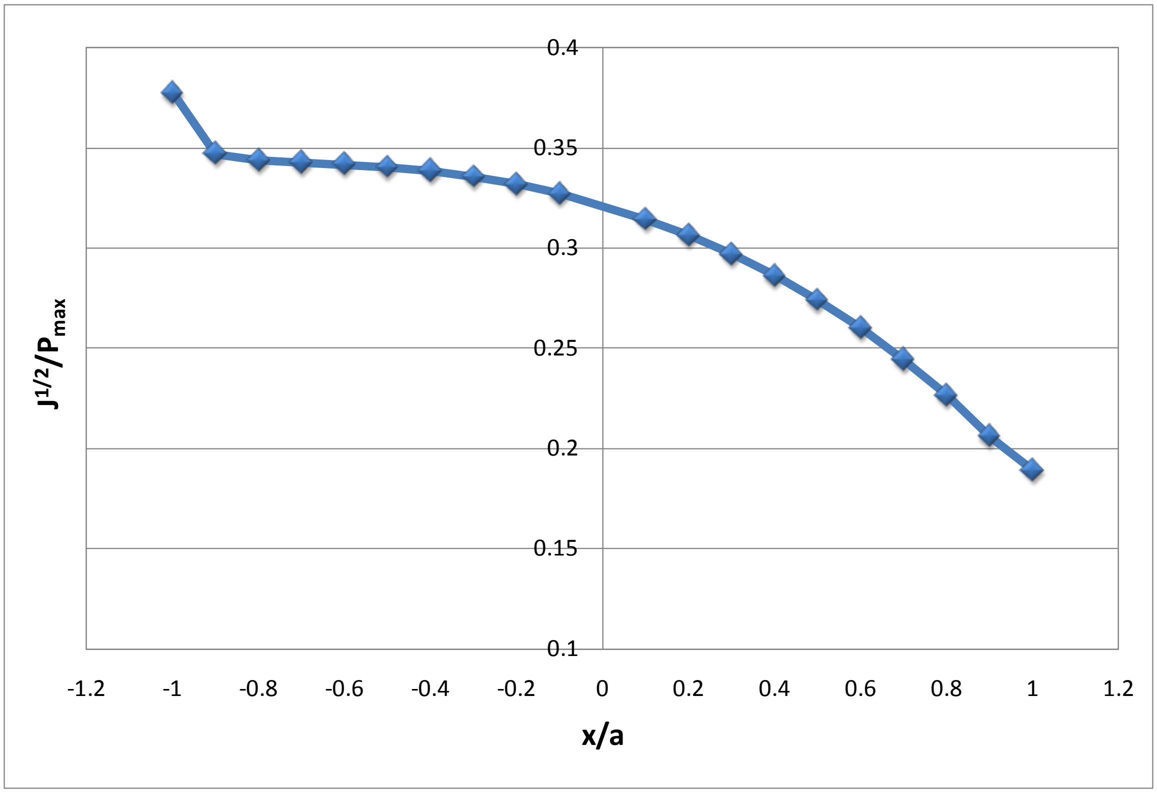

Figure4.12:Vaules of $J^{1/2}/P_{\max}$ on the surface centerline (z = 0, y =0).

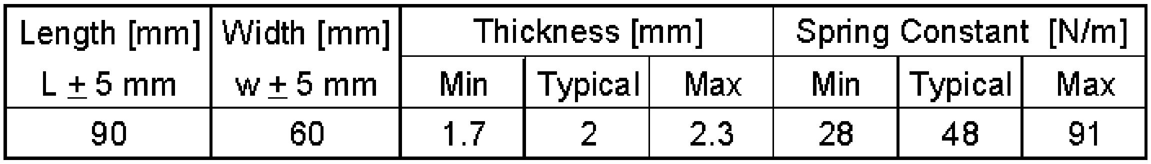

Length [mm]	Width [mm]	Thickness [mm]			Spring Constant [N/m]		
L ± 5 mm	w ± 5 mm	Min	Typical	Max	Min	Typical	Max
90	60	1.7	2	2.3	28	48	91

Table 4.1: Dimensions and a range of a spring constant of cantilevers used in the experiments.

Structure	Width [nm]		Dielectric Material
	Copper	Dielectric	
1	234.57	141.97	A
2	223.32	245.65	A
3	123.72	40.93	A
4	80.93	81.86	B

Table 4.2: Widths of the copper patterns and dielectric materials and their ratios for structures.

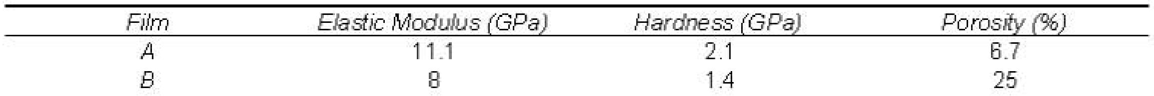

Film	*Elastic Modulus (GPa)*	*Hardness (GPa)*	*Porosity (%)*
A	11.1	2.1	6.7
B	8	1.4	25

Table 4.3: Properties of nonporous and porous dielectric materials.

Material	Curvature Radius [nm]	Elastic Modulus [GPa]	Poisson ratio
Diamond probe	500	1141	0.07
Copper	Infinity	110	0.3
Dielectric A	Infinity	11	0.17
Dielectric B	Infinity	8	0.17

Table 4.4: Values to calculate contact radii of the contact between the diamond probe and its counterfaces.

μ	P_{cr} based on 12.48 GPa [μN]	P_{cr} based on 44.13 GPa [μN]
0.1	6.512	52.100
0.2	2.381	19.045
0.3	1.098	8.784
0.4	0.589	4.714
0.5	0.351	2.806
0.6	0.225	1.800
0.7	0.153	1.222
0.8	0.108	0.866
0.9	0.080	0.636
1.0	0.060	0.481

Table 4.5: Critical loads as a function of friction coefficient for two effective moduli.

4.6 References

4.1 J. M. Neumeister, W.A. Ducker, Rev. Sci, Instrum. 65 (1994) 2427-2531.

4.2 J.E. Sader, Rev. Sci. Instrum. 66 (1995) 4583-4587.

4.3 G. M. Hamilton, L. E. Goodman, Journal of Applied Mechanics. (1996) 371 – 376

4.4 G. M. Hamilton, Proc. Instn. Mech. Engrs. Vol 197C (1983) 53 – 59

4.5 K. L. Johnson, *Contact Mechanics*, Cambridge University Press, 1987

4.6 N. Saka, T. Eusner, J.-H. Chun, *Nano-scale scratching in chemical-mechanical polishing*, CIRP Annals – Manufacturing Technology 57 (200) 341 - 344

4.7 D. B. Bogy, Edge-Bonded Dissimilar Orthogonal Elastic Wedges Under Normal and Shear Loading, Journal of Appl. Mech., Vol.35, (1968) 460 – 466.

4.8 D. B. Bogy, Two Edge-Bonded Elastic Wedges of Different Materials and Wedge Angles Under Surface Traction, Jour. Of Appl. Mech., Vol.38 (1971) 377 – 386.

Chapter Five
Conclusions

In this work, lateral force microscopy (LFM) was performed with analogs (silica-coated AFM probe and diamond-coated AFM probe) of a nanoscale individual CMP abrasive particle to mimic a chemical mechanical polishing (CMP) process. The silica-coated AFM probes were used to investigate the 2-body friction contribution of an individual silica CMP polishing particle in contact with the polishing pad (JK111) and silica substrates (bulk silica and thermal grown oxide wafer) for load and pH ranging from 10 nN to 50 nN and 7 to 11, respectively. Actual surface deformations of the three samples were obtained by considering the effect of pH on softening of the pad and silica materials (silica probe and silica substrates) and on the surface force, which caused overestimation of the measured surface deformation. The actual deformation was used to determine which mode of friction was involved during LFM. It was shown that the predominant friction mode for the pad surface was plowing friction while the friction of the silica substrates was governed by adhesive friction. This difference was why the pad experienced larger friction than the silica substrates. For the bulk silica substrate, the friction was lower due to the formation of a presumed silica gel layer by the high pH solution. A proper friction model for the bulk silica was determined by fitting the friction results with Carpick's generalized transition equation. The friction results at pH 7 and 9 were determined to follow the JKR model. The friction response at pH 10 and 11 did not show any friction at zero normal load, so the analysis of the friction data was based on a Hertzian contact model. The measured surface deformation and friction coefficient in this work can be used as inputs to material removal rate (MRR) models because they are measured with a particle analog of an individual CMP abrasive particle.

The diamond-coated AFM probes were used to simulate the surface deformation during a CMP process. AFM force lithography on structures composed of various copper-dielectric pattern densities and two dielectric materials under a KOH environment was performed. The modified surfaces due to lateral force were analyzed to obtain the scratch depth of copper interconnects and line bending of patterned structures. It was observed that the deformation of the dielectric film was negligible as compared to that of the copper interconnects when the profiles of the scratches were analyzed. Both scratch depth and pile-up of copper interconnects increased with normal loads. Removal of copper at low load did produce pile-up but the magnitude of the pile up increased significantly with larger loads. It was observed that the structure with higher pattern densities were susceptible to deformation because the ratio of the copper interconnect to the dielectric was larger. Thus, it is crucial to estimate the load for the onset of the plastic deformation of copper interconnects for the surface deformation. In addition, a weaker dielectric film was far more susceptible to plastic deformation as expected. For bending of pattern structures, it was found that the structure with a similar pattern density but larger dielectric film width or with stiffer dielectric material was more resistant to bending.

Bibliography

1.1 Perry, Chemical Mechanical Polishing: The Impact of New Technology on an Industry, 1998 Symposium on VLSI Technology Digest of Technical Papers

1.2 http://www.sia-online.org/pre_resources_FAQ.cfm

1.3 Guanghui Fu, Abhijit Chandra, Sumit Guha, and Ghatu SubhashF, IEEE TRANSACTIONS ON SEMICONDUCTOR MANUFACTURING, A Plasticity-Based Model of Material Removal in Chemical–Mechanical Polishing (CMP) 14 (2001) 406 – 417

1.4 J. M. Steigerwald, S. P. Murarka, and R. J. Gutmann, *Chemical Mechanical planarization of Microelectronic Materials*, John Wiley & Sons, New York (1997)

1.5 R. K. Singh, S.-M. Lee, K.-S. Choi, G. B. Basim, W. Choi, Z. Chen, and B. M. Moudgil, *MRS Bull.,* **27**, 752 (2002)

1.6 J. M. Steigerwald, S. P. Murarka, and R. J. Gutmann, *Chemical Mechanical Planarization of Microelectronic Materials*. New York: Wiley, 1997

1.7 R. K. Singh and R. Bajaj, in *Advances in Chemical-Mechanical-Planarization 2002*, R. K. Singh and R. Bajaj, Editors; PV 27-10, p. 743, Materials Research Society Bulletin, Warrendale, PA (2002)

1.8 S. M. Lee, W. Choi, V. Craciun, S. H. Jung, and R. K. Singh, Paper I4.11, presented at Materials Research Society Meeting, San Francisco, April 2002

1.9 Yuan, C A, Driel, W D van, Silfhout, R B R van, Sluis, O van der, Engelen, R A B, Ernst, L J, Keulen, F van, & Zhang, G Q, Delamination Analysis of Cu/low-k Technology Subjected to Chemical-Mechanical Polishing Process Conditions, Microelectronics Reliability 46 (2006) 1679-1684

1.10 Vlassak, *A model for chemical–mechanical polishing of a material surface based on contact mechanics*, Journal of the Mechanics and Physics of Solids 52 (2004) 847 – 873

1.11 J. Bai, Y.W. Zhao, Y.G. Wang, *A mathematical model for material removal and chemical–mechanical synergy in chemical–mechanical polishing at molecular scale*, Applied Surface Science 253 (2007) 8489–8494

1.12 Luo and Dornfeld, *Material Removal Mechanism in Chemical Mechanical Polishing: Theory and Modeling*, IEEE TRANSACTIONS ON SEMICONDUCTOR MANUFACTURING, VOL. 14, NO. 2, (MAY 2001) 112-133

1.13 Q. Luo, D.R. Campbell, S.V. Babu, Langmuir 12 (1996) 3563.

1.14 M. Hariharaputhiran, J. Zhang, S. Ramarajan, J.J. Keleher, Y. Li, S.V. Babu, J. Electrochem. Soc. 147 (2000) 3820.

1.15 A. Jindal, S. Hegde, S.V. Babu, Electrochem. Solid State Lett. G 48 (2002) 5.

1.16 D. Zeidler, Z. Stavreva, M. Plotner, K. Drescher, Microelectron. Eng. 33 (1997) 259.

1.17 R. Carpio, J. Farkas, R. Jairath, Thin Solid Films 266 (1995) 238.

1.18 Q. Luo, R.A. Mackay, S.V. Babu, Chem. Mater. 9 (1997) 2101.

1.19 Y. Li, M. Hariharaputhiran, S.V. Babu, J. Mater. Res. 16 (2001) 1066.

1.20 A. Jindal, Y. Li, S.N. Barayanan, S.V. Babu, Mat. Res. Soc. Symp. Proc. 671 (2001) M4.10.1.

1.21 Y. Li, S.V. Babu, Electrochem. Solid State Lett. 148 (2001) G20.

1.22 Wonseop Choi, Seung-Mahn Lee, and Rajiv K. Singh, pH and Down Load Effects on Silicon Dioxide Dielectric CMP, Electrochemical and Solid-State Letters, 7 (2004) G141-G144

1.23 William A. Ducker, Tim J. Senden, and Richard M. Pashley, *Direct measurement of colloidal forces using an atomic force microscope*, Nature

353 (1991) 239

1.24 Xue Yun Lin, Francois Creuzet, Herve Arribart, *Atomic Force Microscopy for Local Characterization of Surface Acid-Base Properties*, J. Phys. Chem. 1993, 97, 7272-7276

1.25 Igor Sokolov, Quy K. Ong, Hasan Shodiev, Nina Chechik, David James, Mike Oliver, *AFM study of forces between silica, silicon nitride and polyurethane pads*, Journal of Colloid and Interface Science 300 (2006) 475–481

1.26 Elena Taran, Bogdan C. Donose, Ivan U. Vakarelski, Ko Higashitani, *pH dependence of friction forces between silica surfaces in solutions*, Journal of Colloid and Interface Science 297 (2006) 199–203

1.27 T. A. Michalske and S. W. Freiman, *J. Am. Ceram. Soc.,* **66**, 284 (1982)

1.28 T. A. Trogolo and K. Rajan, *J. Mater. Sci.,* **29**, 4554 (1994)

1.29 F. B. Kaufman, D. B. Thompson, R. E. Broadie, M. A. Jaso, W. L. Guthrie, D. J. Pearson, and M. B. Small, *J. Electrochem. Soc.,* **138**, 3460 (1991)

1.30 N. J. Brown, P. C. Baker, and R. T. Maney, *Proc. SPIE, Int. Soc. Opt. Eng.*, **306**, 42 (1981)

1.31 L. M. Cook, *J. Non-Cryst. Solids,* **120**, 152 (1990)

1.32 1.4 T. Hara Proceedings of VMIC Asia, 2002 (November) IMIC Publishers (http://www.imic.org) p. 161

1.33 S. Wang, G. Grover, C. Baker, J. Chamberlain, C. Yu, Solid State Technol. 2001 (September) S9

1.34 S. Kondo, S. Tokitoh, B.U. Yoon, A. Namiki, A. Sone, N. Ohashi,K. Misawa, S. Sone, H.J. Shin, T. Yoshie, K. Yoneda, M. Shimada, S. Ogawa, I. Matsumoto, N. Kobayashi, in: International Interconnect Technology Conference 2003 (IITC 2003), IEEE, Piscataway NJ, USA, 2003, pp. 86–88

1.35 T. Scherban, B. Sun, J. Blaine, C. Block, B. Jin, E. Andideh, in: International Interconnect Technology Conference 2001 (IITC 2001), IEEE, Piscataway NJ, USA, 2001, pp. 257–259

1.36 P. Leduc, M. Savoye, S. Maitrejean, D. Scevola, V. Jousseaume, G. Passemard, in: International Interconnect Technology Conference 2005 (IITC 2005), IEEE, Piscataway NJ, USA, 2005, pp. 209–211

1.37 S. Wang, G. Grover, C. Baker, J. Chamberlain, C. Yu, Solid State Technol. 2001 (September) S9

1.38 X.T. Chen, Y.T. Tan, Y.W. Chen, C.Y. Li, S. Balakumar, K. Chew, P.D. Foo, Proc. 19th VMIC conference, 2002, Singapore, 2002, IMIC Publishers (http://www.imic.org) p. 156

1.39 T. Hara, M. Uchica, M. Fuimoto, T.K. Doy, S. Balakumar, N. Babu, Electrochem. Solid State Lett. 7 (2004) G28

1.40 A.K. Sikder, P. Zantye, S. Thagrella, A. Kumar, B.M. Vinogradov, N.V. Gitis, CMP MIC Proceedings, 2003, IMIC Publishers (http://www.imic.org) p. 120

1.41 N. Endo, S. Kondo, S. Tokitou, B.U. Yoon, N. Ohashi, S. Sone, H.J. Shin, I. Matsumoto, N. Kobayashi, CMP-MIC Conference Proceedings, 2003, IMIC Publishers (http://www.imic.org) p. 101

1.42 Busch, Analyzing damage from ultralow-k CMP, *Solid State Technology* November, 2005

1.43 Balakumar and etc., Peeling and delamination in Cu/SiLK^{TM} process during Cu-CMP, Thin Solid Films 462-463 (2004) 161-167

1.44 Leduc and etc., Dependence of CMP-induced delamination on number of low-k dielectric films stacked, Microelectronic Engineering 83 (2006) 2072-2076

2.1 Zhan Chen, and Rajiv K. Singh, Mechanism of Particle Deposition on Silicon Surface during Dilute HF Cleans, *Journal of The Electrochemical Society*, 150 (11) G667-G672 (2003).

2.2 D. Devecchio, P. Schmutz, and G. S. Frankel, *Electrochemical and Solid-State Letters,* 3 (2) 90-92 (2000).

2.3 F. Stevens, S. C. Langford, and J. T. Dickinson, Tribochemical wear of sodium trisilicate glass at the nanometer size scale, Journal of Applied Physics, **99**, 023529 (2006).

2.4 G. Huttl, D. Beyer, and E. Muller, Investigation of Electrical Double Layers on SiO_2 Surfaces by Means of Force *vs*. Distance Measurements, Surface and Interface Analysis, 1997, Volume 25, 543-547

3.1 J. Hutter and J. Bechhoefer, Calibration of atomic-force microscope tips, Review of Scientific Instruments, 1993, Volume 64, 1868-1873.

3.2 Bozkaya et al. Proceedings of the STLE/ASME International Joint Tribology Conference IJTC2008 (2008) 71122.

3.3 Karuppiah et al., Material Research Society Symposium Proceedings, 2007, Volume 977, 0977-FF04-04-DD05-04

3.4 Johnson, K. L., Kendall, K., and Roberts, A. D., Proc. R. Soc. London A **324,** 301 (1971).

3.5 B.V. Derjaguin, V.M. Muller and Y.P. Toporov, "Effect of Contact Deformations on Adhesion of Particles," *Journal of Colloid and Interface Science* , **53**, 314-326 (1975).

3.6 Robert W. Carpick,1 D. Frank Ogletree, and Miquel Salmeron, "A General Equation for Fitting Contact Area and Friction vs Load Measurements," *Journal of Colloid and Interface Science* **211**, 395-400 (1999).

3.7 Maugis, D., *J. Colloid Interface Sci.* **150,** 243 (1992).

3.8 R.W. Stark, T. Drobek, and W.M. Heckl, Thermomechanical noise of a free v-shaped cantilever for atomic-force microscopy, Ultramicroscopy 86 (2001) 207-215.

3.9 NT-MDT, *Probe-Sample Interaction: Lateral Forces*, Application Notes.

3.10 I. Sokolov, Surf. Sci. 311 (1994) 287

3.11 Maugis, *Contact, Adhesion and Rupture of Elastic Solids*. Springer-Verlag (2000), Berlin.

3.12 Oliver M.R. (ed), 2004. *Chemical mechanical planarization of semiconductor materials*. Springer, NY.

3.13 Jacob Israelachvili, *Intermolecular $ Surface Froces*, Academic Press

(1992)

3.14 http://www.erc.arizona.edu/Education/MME%20Course%20Materials/MME%20Modules/Surface%20Prep%20Module/Wet%20Etching%20and%20Cleaning%20-%20Surface.ppt#260

3.15 Murakoshi et al., *Local mechanical properties of mouse outer hair cells: Atomic force microscopic studyAuris*, Nasus Larynx, 2006. **33** 149-157.

3.16 Obeng et al. Obeng, Y., Dogariu, A., and Forsthoefel, K., Mechanical and Chemical Properties of Pads for Use in Chemo-Mechanical Processing (CMP)

3.17 M. Tomozawa, K. Yang, H. Li, and S. P. Muraka, *Mater. Res. Soc. Symp. Proc.,* **337**, 89 (2002).

3.18 M. L. Hammond and S. F. Ravitz, *J. Am. Ceram. Soc.,* **46**, 329 (1963).

3.19 L. Nevot and P. Croce, *Rev. Phys. Appl.,* **15**, 761 (1980).

3.20 Williams, Engineering Triboloy, Cambridge University Press, 2005

3.21 R.W. Carpick and M. Salmeron, "Scratching the surface: Fundamental investigations of tribology with atomic force microscopy," *Chemical Reviews* **97**, 1163-1194 (1997).

4.1 J. M. Neumeister, W.A. Ducker, Rev. Sci, Instrum. 65 (1994) 2427-2531.

4.2 J.E. Sader, Rev. Sci. Instrum. 66 (1995) 4583-4587.

4.3 G. M. Hamilton, L. E. Goodman, Journal of Applied Mechanics. (1996) 371 – 376

4.4 G. M. Hamilton, Proc. Instn. Mech. Engrs. Vol 197C (1983) 53 – 59

4.5 K. L. Johnson, *Contact Mechanics*, Cambridge University Press, 1987

4.6 N. Saka, T. Eusner, J.-H. Chun, *Nano-scale scratching in chemical-mechanical polishing*, CIRP Annals – Manufacturing Technology 57 (200) 341 - 344

4.7 D. B. Bogy, Edge-Bonded Dissimilar Orthogonal Elastic Wedges Under Normal and Shear Loading, Journal of Appl. Mech., Vol.35, (1968) 460 – 466.

4.8 D. B. Bogy, Two Edge-Bonded Elastic Wedges of Different Materials and Wedge Angles Under Surface Traction, Jour. Of Appl. Mech., Vol.38 (1971) 377 – 386.